

学 位 論 文

Application of Laser Absorption Spectroscopy to High Enthalpy
Flow Diagnostics

(レーザー吸収分光法の高エンタルピー気流診断への応用)

2005 年度

東京大学大学院新領域創成科学研究科
先端エネルギー工学専攻

松 井 信

Acknowledgments

I would like to express my gratitude to Associate Professor Kimiya Komurasaki. He has given me opportunities of experiments in his laboratory and in Germany. For five years, due to his excellent advice and encouragements, I could resolve many experimental and theoretical problems. I'm grateful to Professor Yoshihiro Arakawa (Department of Aeronautics and Astronautics) for his advice and discussion.

I'm also grateful to Professor Monika Auweter-Kurtz (Institut für Raumfahrtssysteme, University of Stuttgart) for giving me an opportunity of experiments at IRS in Germany. Gratitude is also extended to Dr.-Ing Georg Herdrich (IRS) for cooperating experiments and giving me deep understanding of ICP plasma, Dr.-Ing Michael Winter for his advice concerning the experimental set up and plasma physics and Dr.-Ing Thomas Wegmann for his advice about my life in Germany. In the experiments in JUTEM and ISTA/JAXA, I'm indebted to Dr. Masahito Mizuno, Dr. Takeshi Ito and all researchers in Wind Tunnel Technology Center.

I thanks to elders and betters at the University of Tokyo: Dr. Hiroshi Katsurayama (ISAS/JAXA), Dr. Koichi Mori (Tohoku University), Dr. Naoji Yamamoto (Kyushu University) and Mr. Masanori Sugimine (IHI Aerospace) for their fruitful discussion about thermodynamics and numerical approach.

I'm obliged to all members in high enthalpy flow and laser diagnostics group who have corroborated and helped my experiments.

Finally, I wish to thank all members in Arakawa-Komurasaki laboratory who propose a comfortable atmosphere.

Contents

| | |
|---|-----------|
| LIST OF FIGURE | 5 |
| LIST OF TABLE..... | 9 |
| CHAPTER 1 | |
| INTRODUCTION..... | 10 |
| 1.1 BACKGROUND | 10 |
| 1.2 PLASMA WIND TUNNELS..... | 12 |
| 1.2.1 Huels arc wind tunnel..... | 14 |
| 1.2.2 Constricted arc wind tunnel | 15 |
| 1.2.3 Magnetically stabilized arc wind tunnel..... | 16 |
| 1.2.4 Segmented arc wind tunnel..... | 17 |
| 1.2.5 MPD wind tunnel..... | 18 |
| 1.2.6 ICP wind tunnel..... | 19 |
| 1.2.7 Lists of Plasma wind tunnels in the world | 20 |
| 1.3 PLASMA DIAGNOSTICS..... | 22 |
| 1.3.1 Intrusive methods | 22 |
| 1.3.2 Non-intrusive methods | 30 |
| 1.3.3 Selection of diagnostics method..... | 34 |
| 1.4 LASER ABSORPTION SPECTROSCOPY..... | 35 |
| 1.4.1 History of absorption spectroscopy..... | 35 |
| 1.4.2 Applications of Laser absorption spectroscopy in other fields | 35 |
| 1.4.3 Applications of LAS to plasma wind tunnel flows and its problems..... | 36 |
| 1.5 OBJECTIVES | 38 |
| CHAPTER 2 | |
| APPLICABLE LIMIT OF LASER ABSORPTION SPECTROSCOPY | 39 |
| 2.1 PRINCIPLE OF LASER ABSORPTION SPECTROSCOPY..... | 39 |
| 2.1.1 Laser absorption..... | 40 |
| 2.1.2 Absorption coefficient..... | 40 |
| 2.1.3 Line broadening | 42 |
| 2.1.4 Line shape function..... | 46 |
| 2.1.5 Absorption Shift | 46 |

| | |
|---------------------------------|----|
| 2.1.6 Absorption Target..... | 47 |
| 2.2 MEASUREMENT SYSTEM | 48 |
| 2.2.1 Tunable diode laser | 50 |
| 2.2.2 Etalon | 51 |
| 2.2.3 Optical Equipments | 55 |
| 2.3 DATA PROCESSING..... | 56 |
| 2.3.1 Abel Inversion..... | 56 |
| 2.3.2 Gauss fitting..... | 58 |

CHAPTER 3

| | |
|--|-----------|
| APPLICABLE LIMIT OF LASER ABSORPTION SPECTROSCOPY | 60 |
| 3.1 ERROR AND APPLICABLE LIMIT OF LAS | 60 |
| 3.1.1 Signal to noise ratio | 60 |
| 3.1.2 Error analysis and applicable limit of LAS..... | 60 |
| 3.2 ABSORPTION SATURATION..... | 64 |
| 3.2.1 Background: Absorption saturation in LIF | 64 |
| 3.2.2 Theory of Absorption Saturation | 65 |
| 3.2.3 Experimental Apparatus..... | 68 |
| 3.2.4 Experimental results | 70 |
| 3.2.5 Discussion..... | 72 |
| 3.3 SUMMARY..... | 76 |

CHAPTER 4

| | |
|--|-----------|
| APPLICATION TO CONSTRICTED ARC WIND TUNNELS FLOWS..... | 77 |
| 4.1 FACILITIES | 77 |
| 4.1.1 JUTEM 20-kW Erosion Testing Machine | 77 |
| 4.1.2 THE UNIVERSITY OF TOKYO 1.2-kW ARC-HEATER..... | 78 |
| 4.2 TEST CONDITIONS..... | 85 |
| 4.2.1 Velocity Measurement..... | 85 |
| 4.2.2 Number Density and Translational Temperature Measurement | 85 |
| 4.3 MEASURED RESULTS..... | 88 |
| 4.3.1 Flow Velocity | 88 |
| 4.3.2 Number Density Distributions | 88 |
| 4.4 DISCUSSION | 91 |
| 4.4.1 Flow Velocity | 91 |
| 4.4.2 Density distributions | 91 |

| | |
|---|------------|
| 4.5 COMPARISON WITH CFD RESULTS | 92 |
| 4.5.1 Numerical models | 92 |
| 4.5.2 Results and Discussion | 94 |
| 4.6 SUMMARY..... | 98 |
| CHAPTER 5 | |
| APPLICATION TO ICP FLOWS..... | 99 |
| 5.1 FACILITIES | 99 |
| 5.2 TEST CONDITIONS AND PREVIOUS TESTS..... | 102 |
| 5.3 RESULTS..... | 104 |
| 5.4 DISCUSSION | 107 |
| 5.4.1 Temporal variation of plasma properties | 107 |
| 5.4.2 Time averaged specific total enthalpy..... | 109 |
| 5.4.3 Comparison with intrusive measurements..... | 110 |
| 5.5 SUMMARY..... | 112 |
| CHAPTER 6 | |
| CONCLUSION..... | 113 |
| REFERENCE..... | 115 |

List of Figure

CHAPTER 1

| | |
|--|----|
| Fig. 1-1 Trajectory of various reentry vehicles (Ref. [1]). | 11 |
| Fig. 1-2 Stagnation temperature as a function of test time for various wind tunnels (Ref. [1]). | 11 |
| Fig. 1-3 Flow conditions in actual flight and plasma wind tunnel (Ref. 9). | 13 |
| Fig. 1-4 Pressure specific enthalpy envelops for various plasma wind tunnels (Ref. 10). | 13 |
| Fig. 1-5 Schematic of Huels plasma wind tunnel. | 14 |
| Fig. 1-6 Schematic of typical constricted arc plasma wind tunnel (right) and NASA Ames concentric ring arcjet (left, Ref. 16). | 15 |
| Fig. 1-7 Schematic of magnetically stabilized plasma wind tunnel. | 16 |
| Fig. 1-8 Schematic of segmented arc plasma wind tunnel. | 17 |
| Fig. 1-9 Schematic of MPD plasma wind tunnel. | 18 |
| Fig. 1-10 Schematic of ICP plasma wind tunnel. | 19 |
| Fig. 1-11 Schematic of calorimeter (Ref. [37]). | 23 |
| Fig. 1-12 Conceptual figure of sonic flow method (Ref. [65]). | 24 |
| Fig. 1-13 Schematic of enthalpy probe (Ref. [63]). | 24 |
| Fig. 1-14 Schematic of heat flux probe (Ref. [37]). | 25 |
| Fig. 1-15 Schematic of Pitot probe (Ref. [63]). | 26 |
| Fig. 1-16 Schematic of heat flux probe (Ref. [63]). | 27 |
| Fig. 1-17 Conceptual figure of time of flight probe (Ref. [63]). | 27 |
| Fig. 1-18 Schematic of mass spectrometer (Ref. [71]). | 28 |
| Fig. 1-16 Schematic of single probe (Ref. [63]). | 29 |
| Fig. 1-17 Typical current-voltage curve in a single probe measurement. | 29 |

CHAPTER 2

| | |
|---|----|
| Fig. 2-1 Relationship between physical properties and absorption profiles. | 39 |
| Fig. 2-2 Grotrian diagram of atomic oxygen. | 47 |
| Fig. 2-3 Grotrian diagram of argon. | 47 |
| Fig. 2-4 Schematic of measurement system for laser absorption spectroscopy. | 48 |
| Fig. 2-5 Photograph of measurement system for laser absorption spectroscopy. | 49 |
| Fig. 2-6 Schematic of velocity measurement system. | 49 |
| Fig. 2-7 Conceptual diagram of LittmannvMetcalf cavity. | 50 |
| Fig. 2-8 a) solid type etalon (left figure), b) air-spaced plane-parallel type etalon | |

| | |
|---|----|
| (right figure). | 53 |
| Fig. 2-9 An optical path difference in etalon. | 53 |
| Fig. 2-10 Transmitted intensity as a function of phase shift for various reflectivities. | 54 |
| Fig. 2-11 Abel inversion. | 56 |
| Fig. 2-12 Radial profiles of absorption fraction and 12 th order polynomial fitting.. | 58 |
| Fig. 2-13 Absorption coefficient and Gauss fitting after Abel inversion. | 59 |

CHAPTER 3

| | |
|--|----|
| Fig. 3-1 Estimated error of absorption coefficient | 61 |
| Fig. 3-2 Conceptual figure of a relationship between absorption coefficient error and FWHM one. | 62 |
| Fig. 3-3 Estimated error of temperature for various fractional absorption and corresponding number density (λ , A , g , are used in OI 777.19nm, absorption length is 1cm.) | 63 |
| Fig. 3-4 Relationship between LIF signal and laser intensity | 65 |
| Fig. 3-5 Convolution of homogeneous and inhomogeneous profiles. | 67 |
| Fig. 3-6 Photo of glow discharge tube plasma. | 68 |
| Fig. 3-7. Schematic of TE ₁₀ mode microwave discharge tube. | 69 |
| Fig. 3-8 Photo of microwave discharge tube plasma | 69 |
| Fig. 3-9 Variation of absorption profiles in the glow discharge argon plasma. $\nu_0 =$ 842.46 nm. | 70 |
| Fig. 3-10 Relationship between absorption coefficient and laser intensity. | 71 |
| Fig. 3-11 Saturated Doppler width and deduced temperature. | 71 |
| Fig. 3-12 $I_{s_inhomo}(\nu)/I_{s_inhomo}$ and absorption profile. | 72 |
| Fig. 3-13 Computed variation of absorption profiles. | 73 |
| Fig. 3-14 Relationship between computed absorption coefficient and laser intensity. | 74 |
| Fig. 3-15 Measured and computed FWHM. | 74 |

CHAPTER 4

| | |
|--|----|
| Fig. 4-1 Schematic of arc-JUTEM heater system. | 80 |
| Fig. 4-2 Photograph of JUTEM arc-heater. | 80 |
| Fig. 4-3 Schematic of JUTEM arc-heater. | 81 |
| Fig. 4-4 Schematic of constrictor part of JUTEM arc-heater. | 81 |
| Fig. 4-5 Schematic of University of Tokyo arc-heater. | 82 |
| Fig. 4-6 Photograph of University of Tokyo arc-heater. | 82 |
| Fig. 4-7 Schematic of constrictor part of University of Tokyo arc-heater. | 83 |

| | |
|---|----|
| Fig.4-8 Schematic of injection part of University of Tokyo arc-heater..... | 83 |
| Fig.4-9 Photograph of injection part of University of Tokyo arc-heater. | 84 |
| Fig.4-10 Pressure dependency on mass flow rate. | 84 |
| Fig. 4-11 JUTEM Erosion Testing Machine plume and measurement plane..... | 86 |
| Fig. 4-12 University of Tokyo arc-heater plume and measurement plane. | 86 |
| Fig. 4-13 Typical signals. | 87 |
| Fig. 4-14 Normalized absorption signals. | 87 |
| Fig. 4-15 Absorption profiles in arc-heater plume and radiation tube. | 88 |
| Fig. 4-16 Number density distributions of atomic meta-stable oxygen in JUTEM Erosion Testing Machine..... | 89 |
| Fig. 4-17 Number density distributions of atomic meta-stable oxygen in University of Tokyo arc-heater plumes. | 89 |
| Fig. 4-18 Number density distributions of atomic meta-stable argon in the University of Tokyo arc-heater plumes..... | 90 |
| Fig. 4-19 Mixing process. | 91 |
| Fig.4-20 Computational mesh. | 93 |
| Fig.4-21 Gas inlet conditions. | 94 |
| Fig.4-22 Contours of the computed gas properties in the constrictor. | 95 |
| Fig.4-23 Radial distributions of temperature and oxygen mole fractions in the constrictor. | 96 |
| Fig.4-24 Computed contours of number density of atomic oxygen in the University of Tokyo arc-heater plume..... | 96 |
| Fig. 4-25 Number density distributions of atomic meta-stable oxygen simulated for University of Tokyo arc-heater plume. | 97 |
| Fig. 4-26 Number density distributions of atomic meta-stable oxygen simulated for University of Tokyo arc-heater plume. | 97 |

CHAPTER 5

| | |
|--|-----|
| Fig. 5-1 Schematic of PWK3. | 99 |
| Fig. 5-2 Photo of PWK3..... | 100 |
| Fig. 5-3 Schematic of Meissner type resonant circuit. | 100 |
| Fig. 5-4 Schematic of IPG3 | 101 |
| Fig. 5-5 photo of IPG3 | 101 |
| Fig. 5-6 Induction current and plasma emission signal. | 103 |
| Fig. 5-7 Photo of IPG3..... | 103 |
| Fig. 5-8 Absorption signal at $\nu=\nu_0 - 4$ GHz and emission signal, $r=0$ mm..... | 104 |
| Fig. 5-9 Typical transmitted laser and etalon signals, $r=0$ mm..... | 105 |

| | |
|--|-----|
| Fig. 5-10 Typical absorption coefficient and extracted one in each cycle, $r=0$ mm. | 105 |
| Fig. 5-11 Temporal variations of absorption profile in Mode 1, $r=0$ mm. | 106 |
| Fig. 5-12 History of translational temperature and emission signal, $r=0$ mm..... | 106 |
| Fig. 5-13 Calculated enthalpy and mole fractions by thermo-chemical equilibrium assumptions, $p_{amb}=30$ Pa..... | 108 |
| Fig. 5-14 History of estimated enthalpy and mole fractions, $r=0$ mm. | 108 |
| Fig. 5-15 Time-averaged specific total enthalpy distribution by LAS and Probes. | 109 |
| Fig. 5-16 Enthalpy balance, $r=0$ mm..... | 110 |

List of Table

CHAPTER 1

| | |
|--|----|
| Table 1-1 Plasma wind tunnels in Japan..... | 20 |
| Table 1-2 Plasma wind tunnels in the world. | 21 |
| Table 1-3 Diagnostic method. | 33 |
| Table 1-4 Comparison of LAS, ES and LIF. | 34 |

CHAPTER 2

| | |
|---|----|
| Table 2-1 Comparison of broadening effects | 45 |
| Table 2-2 Transition data..... | 47 |
| Table 2-3 Specification of diode laser with external cavity. | 51 |
| Table 2-4 Specification of optical equipments..... | 55 |

CHAPTER 3

| | |
|--|----|
| Table 3-1 Ratio of deduced temperature to true one T/T_0 | 75 |
|--|----|

CHAPTER 4

| | |
|--|----|
| Table 4-1 Comparison of two vacuum facilities and arc-heaters. | 79 |
| Table 4-2 Experimental conditions for velocity measurement..... | 85 |
| Table 4-3 Experimental conditions for laser absorption spectroscopy..... | 85 |
| Table 4-4 Chemical reaction model. | 92 |

CHAPTER 5

| | |
|--|-----|
| Table 5-1. Operational conditions..... | 102 |
| Table 5-2 Measured parameters [139]..... | 102 |
| Table 5-3 Comparison of Pplasma | 111 |
| Table 5-4 Comparison of $\bar{h}_0(0)$ | 111 |

Chapter 1

Introduction

1.1 Background

When spacecraft entry atmosphere of the earth or other planets, their entry velocity will be several km/s and then they are exposed to severe heat loads by aerodynamic heating as shown in Fig. 1-1 [1~5]. Space shuttle enters the earth at the velocity of 7 km/s (Mach >20) and gas temperature in front of its nose is heated up to 7000K. Then, Thermal Protection System (TPS) are essential to protect spacecraft from such severe conditions. Its developments have begun in 1950's for first manned space flights in Russia (Vostok, 4/12/1961) and in USA (Mercury, 5/5/1961) [6].

As indicated by Auweter-Kurtz [7], TPS requires such characteristics as 1) low mass, 2) smooth surface to avoid an early flow change from laminar to turbulent, 3) necessary strength to withstand aerodynamic, aeroelastic, chemical and heat loads, 4) low catalysity not to encourage the recombination heating, 5) high emissivity to promote the radiation cooling. For such TPS developments, ground test facilities are necessary to simulate reentry conditions, because actual flight-tests have many problems such as high cost, difficult in reproducibility and restrictions of measurement equipments.

Because, unfortunately, there is no facility to simulate such severe reentry conditions completely, various types of ground test facilities have been developed to simulate specific conditions as shown in Fig.1-2. Although, ballistic range, shock tubes, expansion tubes and shock tunnels (including reflected shock tunnels, gun tunnels, Stalker tubes) can produce high temperature and high total pressure conditions, their run time is restricted to be several ms to μ s. It is too short for TPS tests because TPS surfaces remains cold and may less interact with the hot gas than actual flight conditions. The short run time also complicates measurement techniques. Therefore, plasma wind tunnels that can produce high temperature conditions for more than several ten minutes are most suitable for TPS tests and widely used in the world.

In the following sections, plasma wind tunnels and diagnostics methods of their flows are overviewed and a motive of this thesis is presented.

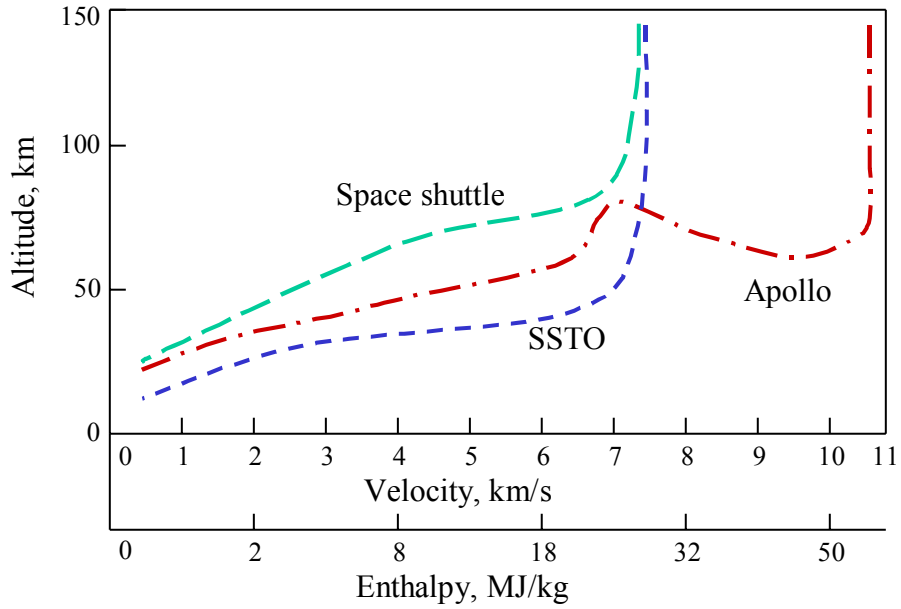


Fig. 1-1 Trajectory of various reentry vehicles (Ref. [1]).

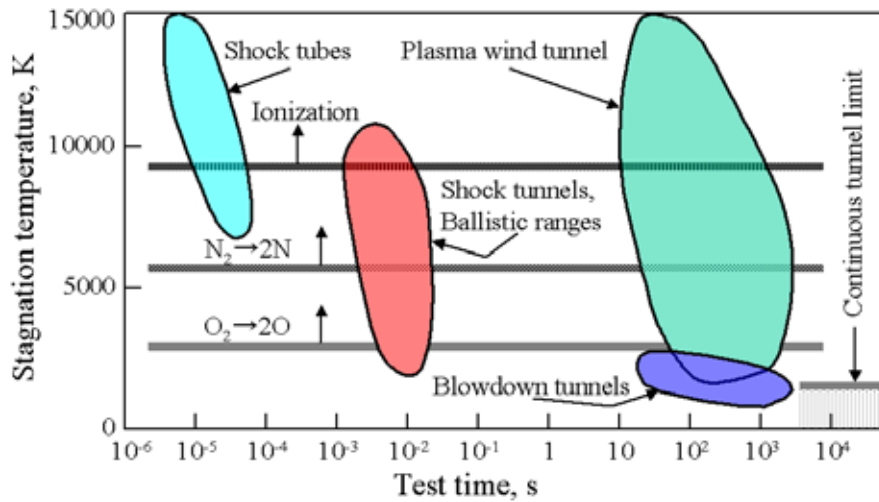


Fig. 1-2 Stagnation temperature as a function of test time for various wind tunnels (Ref. [1]).

1.2 Plasma Wind Tunnels

As indicated by Anfimov [8], plasma wind tunnels has various characteristics such as “(a) to prevent condensation during expansion of air or another test gas to hypersonic Mach number; (b) to duplicate air physical/chemical transformations for study of vehicle aerogasdynamics and heat transfer at hypersonic velocities and also for study of plasma envelopes around vehicles, their radiation and radio wave transmission through them; and (c) to duplicate the real thermal protection ablation process due to material internal physical/chemical changes as well as due to material physical/chemical interaction with a high temperature environment.”

A basic concept of flow conditions in plasma wind tunnels is compared with that of actual flight flows as shown in Fig.1-3 [9]. Test gas heated by electric power in a plenum chamber is dissociated and ionized and then it is accelerated to supersonic by a convergent-divergent nozzle. Because in the nozzle, density of the flows rapidly decreased due to expansion, recombination rates of dissociated and ionized gases also decrease. Therefore, chemical composition of the flows almost keeps frozen during the nozzle expansion whereas translational energy is transferred to the kinetic energy and then translational temperature decreases. As a result, a large part of enthalpy is possessed as chemical potential instead of kinetic energy.

In this way, plasma wind tunnels can produce same total pressure and specific enthalpy conditions with actual flights at stagnation point though flow Mach number is relatively low. Of course, differences of chemical composition and low Mach number in a free stream region should be cared in TPS tests. In fact, this non-equilibrium state in this region is one of the main problems in high specific enthalpy research fields [10].

Since 1950's, various plasma wind tunnels have been developed for various operational conditions. Here, according to Smith [11], these wind tunnels are classified in six types with respect to their heating methods: Huels arc, constricted arc, magnetically stabilized, segmented arc, magnetoplasmadynamic (MPD) and inductively coupled plasma (ICP). Especially in the former five types, arc heating is used and then they are conventionally called “arcjet”. Operational total pressure and specific enthalpy of these six wind tunnels are roughly mapped in Fig. 1-4. In the following sections, brief characteristics and history of these wind tunnels are described.

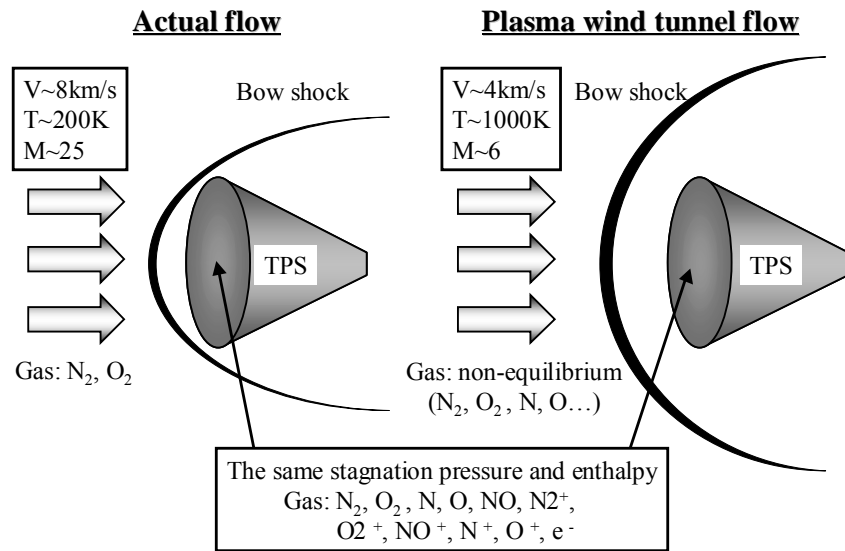


Fig. 1-3 Flow conditions in actual flight and plasma wind tunnel (Ref. 9).

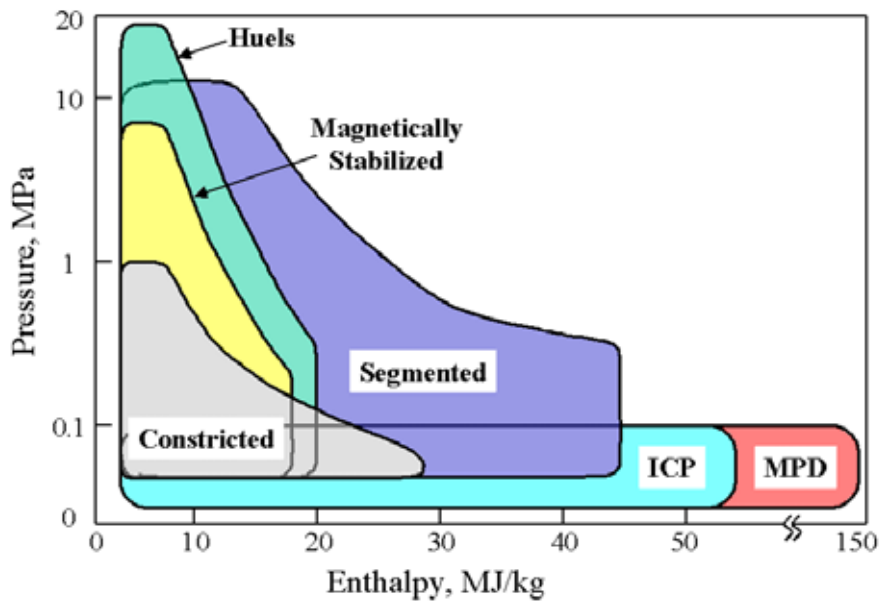


Fig. 1-4 Pressure specific enthalpy envelopes for various plasma wind tunnels (Ref. 10).

1.2.1 Huels arc wind tunnel

An origin of the Huels arc wind tunnels is old. In 1909, the first prototype was developed by German professor Shoenherr as a stable arc plasma generator. In 1928, this basic design was applied to the production of acetylene by German chemical industry Huels AG and 7 MW class Huels arc plasma generator was developed [12]. The name “Huels” derives from this corporation. Then, in 1950’s, the Linde Corporation applied the generator to simulate hypersonic flow under US Air Force contracts [13]. Because of the success of commercialization and abundance of patents, this type of wind tunnel is also called “Linde”.

A schematic of a typical Huels arc wind tunnel is shown in Fig. 1-5. Both cathode and anode are tube-shaped and usually made of water-cooled copper. Working gas is injected into the chamber with a swirl between these electrodes. Arc column is sustained between the electrodes and its length is automatically determined by the operational conditions such as chamber pressure, discharge current and applied magnetic field. For reduction of the electrode erosion, one or two spin coils are equipped and an arc spot is rotated and diffused azimuthally by axial magnetic field.

Advantages of this wind tunnel are high input power, high stagnation pressure, simple and rugged structure and relatively ease of maintenance. Especially, the highest stagnation pressure was reported at 25 MPa with the specific enthalpy of 5.6 MJ/kg [14, 15]. Then this wind tunnel is suitable for the tests of ablative materials.

On the other hand, disadvantages are limitation of the enthalpy, flow fluctuation, high contamination and inconsistent performance. Although the high specific enthalpy is achievable at low total pressure, contamination of flows becomes a severe problem.

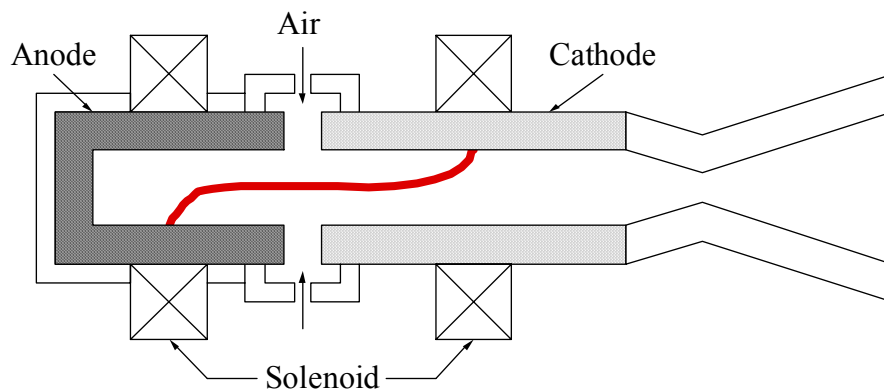


Fig. 1-5 Schematic of Huels plasma wind tunnel.

1.2.2 Constricted arc wind tunnel

In 1960's, constricted arc wind tunnels were developed for enhancement of the specific enthalpy and heat loss of a former NASA Ames concentric ring arcjet [16, 17]. A schematic of this wind tunnel is shown in Fig. 1-6 as well as that of the concentric ring arcjet. Since in the concentric ring arcjet, the arc region is quite small, most of air goes through outside the arc region resulting in the low energy coupling efficiency (Fig. 1-6 left). Then, in the constricted arc wind tunnels, the arc column is forced in a relatively small throat called "constrictor" with flow for the enhancement of the efficiency (Fig. 1-6 right). The cathode is rod shaped and made of a few percent thoriated tungsten to promote thermoionic emission. The anode is usually made of water-cooled copper and plays a role of divergent nozzle. Since the arc spot diffuses in the nozzle because of the low pressure, heat loss and erosion of the anode are reduced. Then, the higher specific enthalpy than that of Huels type is achieved [18].

Advantages of this wind tunnel are simple and rugged structure, long test time and relatively ease of maintenance. On the other hand, in this wind tunnel, air cannot be used as working gas. Instead, non-reactive gases such as nitrogen or argon is used as mainstream and oxygen should be injected at the constrictor part to prevent the hot cathode from oxidation. Other problems are non-uniformity of flows and limitation of the input power due to the short arc column. These problems were resolved by the development of the segmented arc wind tunnels. Therefore, today, there is no large-scale wind tunnel of this type more than MW class input power. However, for their robustness in structure, kW class wind tunnels are widely used at laboratory levels as basic research tools [19-21].

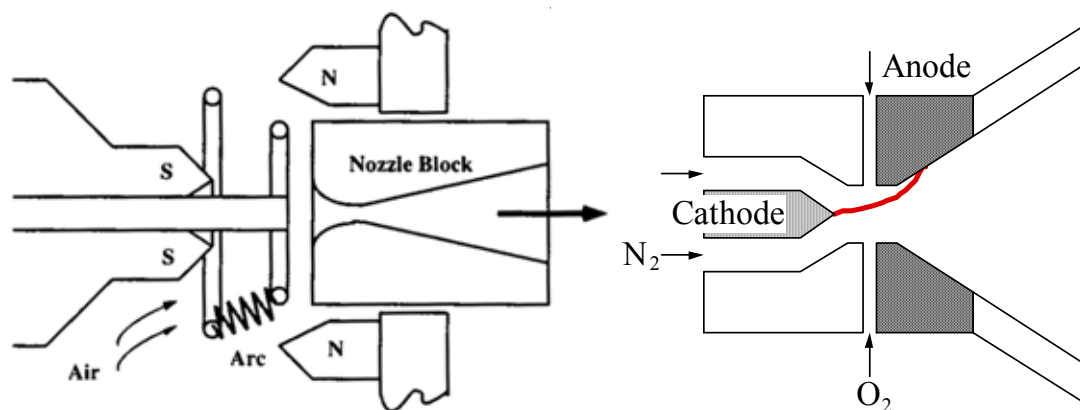


Fig. 1-6 Schematic of typical constricted arc plasma wind tunnel (right) and NASA Ames concentric ring arcjet (left, Ref. 16).

1.2.3 Magnetically stabilized arc wind tunnel

Magnetically stabilized arc wind tunnels were developed at NASA Langley Research Center and the Redstone Arsenal in 1960's [22, 23]. However, today, large-scale wind tunnels of this type are only installed at TsNIMASH in Russia. These wind tunnels have been used for the development of carbon-carbon TPS of Buran and others [8, 24].

A schematic of this wind tunnel is shown in Fig. 1-7. The electrodes are four poles and the arc column is sustained between these electrodes and sidewall. Aside from this, only one pole type wind tunnels called "coaxial" are developed.

Although operational conditions of these wind tunnels are almost same with those of the Huels type, flow contamination are severe and specific enthalpy is generally lower because of a short arc column and low energy coupling efficiency.

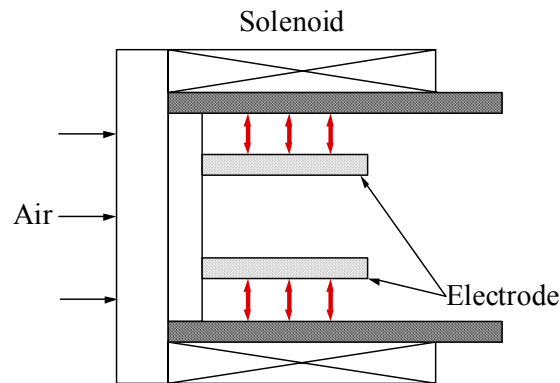


Fig. 1-7 Schematic of magnetically stabilized plasma wind tunnel.

1.2.4 Segmented arc wind tunnel

Segmented arc wind tunnels were developed at NASA Ames Research Center in 1960's [25]. These wind tunnels can operate under wide range conditions as shown in Fig. 1-4. The maximum total pressure, input power and specific enthalpy are reported at 12 MPa (AEDC, USA), 70 MW (CIRA, Italy), and 46.4 MJ/kg (NASA Ames, USA), respectively [26-28]. Therefore, in large-scale wind tunnels, this type is most widely used in the world. In USA, these wind tunnels have been used for developments and tests of TPS of all manned space vehicles and planetary entry or return missions capsules such as Gemini, Apollo, Space Shuttle Orbiter, Galileo and Viking and so on. In Japan, ISAS/JAXA (former ISAS) and ISTA/JAXA (former NASDA, NAL) have equipped these type wind tunnels and the developments and tests of carbon-carbon TPS for the asteroid sample return mission MUSES-C (currently called "HAYABUSA") was conducted [29, 30]. In EU, CIRA and ESA have recently established the largest wind tunnel in 2001 and now various basic parameters are tested [27].

A schematic of this wind tunnel is shown in Fig. 1-8. Different from the Huels type, the arc discharge is fixed between the electrodes and the long arc column is sustainable through the long constrictor. This constrictor is a series of segmented disks. These disks made of water-cooled copper are electrically insulated from each other and their potential is floated to prevent the diffusion of the arc column and to stabilize it. The potential difference between neighboring disks is kept at 30~40 V and this series of disks enables a high voltage operation. Working gas is injected through these disks. If both electrodes are made of water-cooled copper (IHF, NASA Ames [28]), air can be used. However, if the tungsten cathode is used (TP1, NASA Johnson Space Center [31]), oxygen is injected separately from nitrogen down stream of the constrictor to prevent the cathode from oxidation. Apart from the working gas, argon gas is mixed to promote ionization near the electrodes and prevent the electrode from oxidation. Typically, the argon is occupied 10% to 25% of total mass flow (IHF, NASA Ames). At the both electrodes, axial magnetic field is applied to reduce the electrode erosion.

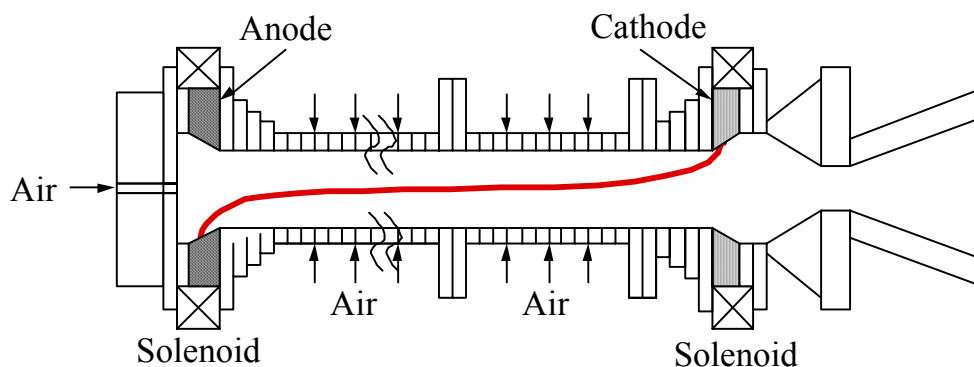


Fig. 1-8 Schematic of segmented arc plasma wind tunnel.

1.2.5 MPD wind tunnel

In 1960's, an MPD wind tunnel was investigated as one of the application of MPD arcjet thruster in USA [32, 33]. Today, these wind tunnels were installed at the Institute fur Raumfahrtssysteme of Stuttgart University (IRS) in Germany and TsTIINSH in Russia [34].

A schematic of this wind tunnel is shown in Fig. 1-9. The structure of the wind tunnels is very similar with that of the constricted arc type. However, discharge current is more than several kA and much higher than that of the constricted arc type. The high current ionizes test gas and accelerated it by a Lorentz force produced by a self-induced magnetic field. Therefore, the velocity of gas is much higher than those in other wind tunnels in which the gas is accelerated by the aerodynamic acceleration through the convergent/divergent nozzle.

The specific enthalpy is reported up to 150MJ/kg (PWK2, IRS) [34]. In addition, the contamination level of the flows is much lower than those in Huels arc, constricted arc, magnetically stabilized, and segmented arc wind tunnels. A small amount of argon is injected on the upstream of the anode to reduce the erosion of anode and the 2% thoriated tungsten cathode enables a very low cathode erosion rate. As a result, hundreds of hours operation is possible without refurbishment of the generator. Therefore these wind tunnels are very suitable for simulation of high altitude conditions or catalytic tests.

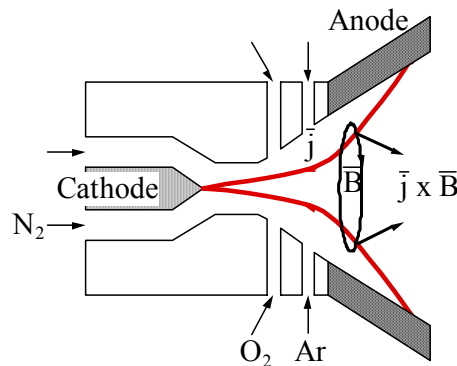


Fig. 1-9 Schematic of MPD plasma wind tunnel.

1.2.6 ICP wind tunnel

ICP was developed in USA and EU in 1960's [35]. Although some efforts were poured, until 1970's the development of this type was abandoned with appearance of the segmented wind tunnels. Instead, several wind tunnels of this type were developed in 1980's in the former Soviet Union [36]. After collapse of the Soviet Union, the research on these wind tunnels was disclosed and several wind tunnels of this type were developed in Germany, France and Belgium [37, 38]. In 2002, an 110kw ICP wind tunnel has been installed in Japan (ISTA/JAXA) [39].

A schematic of the wind tunnel is shown in Fig. 1-10. In this wind tunnel, test gas is flowed in a quartz tube and heated by induction coil. Because of the indirect heating, there is no erosion of electrodes and then contamination level of the flows is extremely lower than those of any other wind tunnels. An ideal test condition for TPS tests can be produced because there are no undesirable chemical reactions that result from the contamination. Then, these wind tunnels are very suitable for catalytic research. Another advantage is that they can use even reactive gases such as carbon dioxide and oxygen because of their electrode-less heating. Mars or Venus atmosphere entry conditions can be simulated.

A disadvantage of this wind tunnel is low total pressure. At the present time, total pressure is much less than 100kPa and most of the facilities are operated at subsonic. However, recently, a few hundred kPa operation of CO₂ has been goalod for the Venus entry simulation [40].

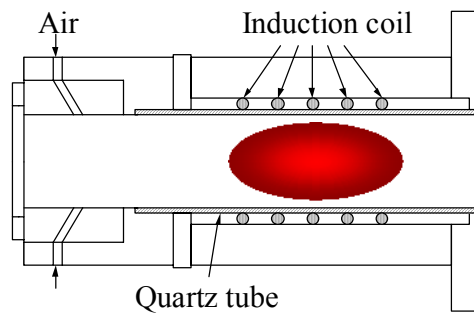


Fig. 1-10 Schematic of ICP plasma wind tunnel.

1.2.7 Lists of Plasma wind tunnels in the world

Table 1-1 shows plasma wind tunnels in Japan with input power over 10kW. The wind tunnels overseas are summarized in Table 1-2. Typical input power, total pressure and specific enthalpy are tabulated [11, 41-50].

Table 1-1 Plasma wind tunnels in Japan.

| Affiliation | Type | Input power kW | Total pressure, MPa | Specific enthalpy MJ/kg |
|--------------------|-------------|---------------------------|--------------------------------|------------------------------------|
| ISAS/JAXA | Huels | 500 | 1 | 16 |
| JUTEM | Constricted | 20 | 0.1 | 10 |
| Kyushu Univ. | Constricted | 20 | 0.1 | 10 |
| Nagoya Univ. | Constricted | 12 | | |
| ISAS/JAXA | Segmented | 1000 | 1.05 | 9.5 |
| ISTA/JAXA | Segmented | 750 | | 15 |
| ISTA/JAXA | ICP | 110 | 0.05 | 25 |
| ISAS/JAXA | ICP | 10 | 0.04 | 32 |

Table 1-2 Plasma wind tunnels in the world.

| Country | Facility | Affiliation | Input power MW | Total pressure, MPa | Specific enthalpy, MJ/kg |
|--------------------------------|-----------------------|--------------------|-------------------|------------------------|-----------------------------|
| Huels | | | | | |
| USA | 2.9 in Turbulent Flow | NASA Ames | 20 | 4 | 9.3 |
| USA | Direct Connect | NASA Ames | 50 | 2.5 | 9.3 |
| USA | AHSTF | NASA Langley | 10 | 4.5 | 3.7 |
| USA | H-R | AEDC | 40 | 10 | 9.3 |
| USA | H-2 | AEDC | 40 | 10 | 9.3 |
| USA | LCAT | Boeing | 10 | 10 | 14 |
| France | JP200 | Aerospatiale | 20 | 6 | 13.2 |
| France | 9 MW HP | Aerospatiale | 9 | 13 | 5.1 |
| France | Simoun | Aerospatiale | 5 | 1.5 | 14 |
| Germany | L2K | DLR | 1 | 1.4 | 25.5 |
| Constricted | | | | | |
| Germany | PWK4 | Univ. of Stuttgart | 0.1 | 0.1 | 30 |
| Magnetically stabilized | | | | | |
| Russia | U15-T-1 | TsNIIMASH | 40 | 1.2 | 7.0 |
| Russia | U-15-T-2 | TsNIIMASH | 50 | 5 | 8.1 |
| Russia | TT-1 | TsNIIMASH | 10 | 8 | 9.3 |
| Russia | TT-2 | TsNIIMASH | 6 | 2.5 | 46.5 |
| Segmented | | | | | |
| USA | AHF | NASA Ames | 20 | 1 | 32.5 |
| USA | IHF | NASA Ames | 60 | 1 | 46.4 |
| USA | TP-1 | NASA JSC | 10 | 1 | 37.1 |
| USA | TP-2 | NASA JSC | 10 | 1 | 37.1 |
| USA | H-1 | AEDC | 30 | 12 | 12 |
| USA | H-3 | AEDC | 68 | 12 | 11 |
| Germany | L3K | DLR | 5 | 1.7 | 21 |
| Italy | Scirocco | CIRA | 70 | 1.7 | 45 |
| MPD | | | | | |
| Germany | PWK1 | Univ. of Stuttgart | 0.25 | 0.1 | 116 |
| Germany | PWK2 | Univ. of Stuttgart | 1.0 | 0.05 | 150 |
| Russia | MPDA-T16 | TsNIIMASH | 4 | 0.003 | 46.5 |
| ICP | | | | | |
| Russia | IPG-3 | IPM RASA | 0.75 | 0.03 | 40 |
| Russia | IPG-4 | IPM RASA | 0.08 | 0.1 | 40 |
| Russia | VTS | TsAGI | 1.0 | 0.08 | 37.2 |
| Russia | VAT-104 | TsAGI | 0.24 | 0.04 | 37.2 |
| Russia | U-13-HFP | TsNIIMASH | 1.0 | 0.04 | 46.5 |
| Germany | PWK3 | Univ. of Stuttgart | 0.15 | 0.01 | 80 |
| France | Comete | Aerospatiale | 0.015 | 0.1 | 32.6 |
| Belgium | Plasmatron | VKI | 1.2 | 0.1 | |

1.3 Plasma Diagnostics

As described above section, plasma wind tunnels are suitable for TPS developments because they can produce high specific enthalpy flows for a long time. Although it is necessary to characterize such flows for evaluation of TPS performances, their exact conditions such as specific enthalpy, total pressure and number density of species have not been relatively unknown [51-56]. Especially mechanisms of catalytic effects and oxidation of TPS, which have been recognized to cause heat flux enhancement and TPS damage, have not been enough clarified resulting in that TPS has been designed with a large factor of safety [57-62]. Then, accurate characterization of flows makes it possible to reduce TPS weight. Moreover, the characterization is useful for validations of CFD calculations for non-equilibrium flows. Therefore, various diagnostics techniques have been developed with the wind tunnels developments [63, 64]. These techniques are classified into intrusive and non-intrusive methods.

1.3.1 Intrusive methods

Intrusive methods are those to put a probe into the flow directly. Although these methods disturb the flow conditions by their insert, they are established methods. In the following paragraph the obtainable parameters and corresponding intrusive methods are described. These are also tabulated and compared with non-intrusive methods in Table 1-3.

Specific enthalpy

The specific enthalpy of the flow is the most important parameter to characterize performances of the wind tunnels and various techniques have been proposed: enthalpy balance, enthalpy probe, sonic flow, and stagnation point heat flux.

Enthalpy balance method – This method is very easy and a most widespread one [64]. The specific enthalpy h_{ave} is estimated by the plasma power P_{plasma} or the input power P_{in} and heat loss P_{loss} , expressed as,

$$h_{ave} = \frac{P_{plasma}}{\dot{m}} = \frac{P_{in} - P_{loss}}{\dot{m}}, \quad (1-1)$$

where, \dot{m} is the mass flow rate. In the former case, the plasma power is directly measured by a calorimeter and in the latter case, the heat loss power is estimated by the increase of cooling water temperature as shown in Fig.1-11 [37]. Although this method may give an indicator to characterize the wind tunnels, the estimated specific enthalpy is the averaged over the volume.

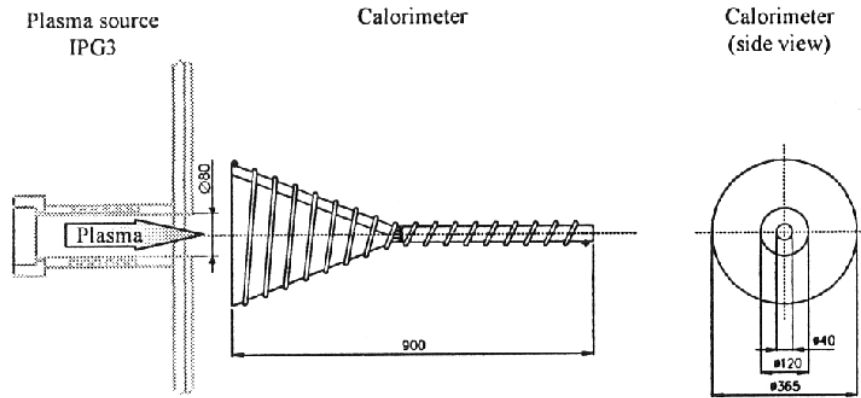


Fig. 1-11 Schematic of calorimeter (Ref. [37]).

Sonic flow method – This method developed by Winovich is based on the fact that sonic mass flow is uniquely determined under thermal equilibrium as shown in Fig. 1-12 [65]. Then, the choked mass flow is determined by a given specific enthalpy and total pressure. Conversely, the specific enthalpy can be estimated by the mass flow and pressure expressed as,

$$\frac{\dot{m}}{Ap_0} = \frac{\sqrt{2h_0}}{RT_0} \left[\frac{\rho^*}{\rho_0} \left(1 - \frac{h^*}{h_0} \right)^{1/2} \right]. \quad (1-2)$$

Here, A is the cross sectional area, h is the enthalpy, p is the pressure, R is the gas constant, T is the temperature, ρ is the density, the subscript 0 refers to stagnation conditions and subscript * refers to conditions at the throat.

In the pressure range $0.025 \text{ MPa} < p_0 < 10 \text{ MPa}$, the above expression considering real gas effects is empirically approximated as [66],

$$\frac{\dot{m}}{Ap_0} = \frac{C}{h_{\text{ave}}^{.397}}. \quad (1-3)$$

Here, C is the constant factor. The effects of boundary layer, non-equilibrium chemistry and heat loss to the nozzle wall were examined. As well as the enthalpy balance method, this method gives only the averaged enthalpy.

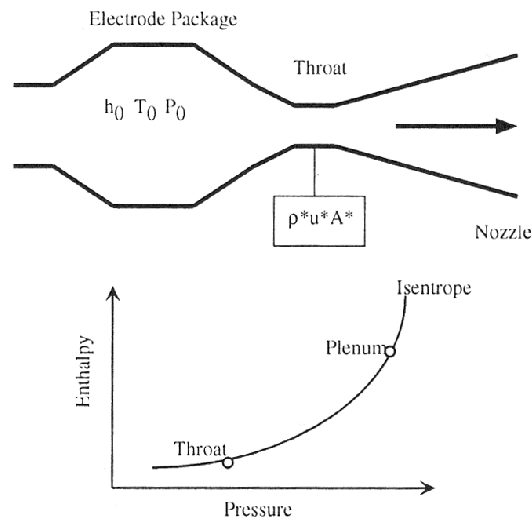


Fig. 1-12 Conceptual figure of sonic flow method (Ref. [65]).

Enthalpy probe – Typical conceptual figure of the enthalpy probe is shown in Fig.1-13 [67, 68]. The hot gas taken in the tip of probe is cooled through the probe and then mass flow and the temperature are measured at the end of probe. The influence of heat flux on the probe other than inlet gas can be removed by opening and closing the inlet. Then the specific enthalpy is estimated by the following equation.

$$h = \frac{\dot{m} C_p T + |\dot{m}_w C_w \Delta T|_{\text{open}} - |\dot{m}_w C_w \Delta T|_{\text{close}}}{\dot{m}} \quad (1-4)$$

Here, the specific heat at constant pressure of the gas, the specific heat of water, mass flow rate and temperature increase of the cooling water are C_p , C_w , \dot{m}_w , ΔT , respectively. This method is not suitable for the high enthalpy measurements because the cooling pass must be prolonged to cool the gas enough. In addition, they are neither suitable for the low-pressure flows because in difficulty of the low mass flow measurements.

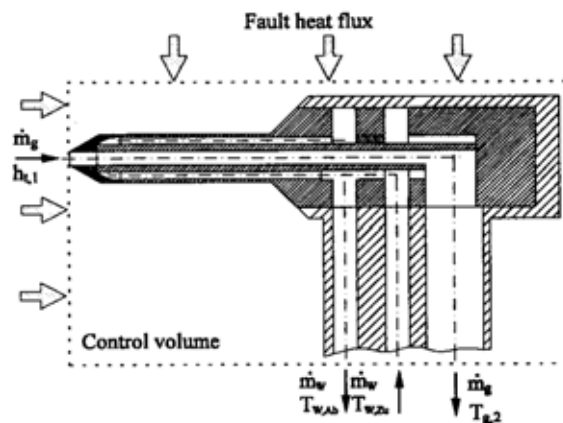


Fig. 1-13 Schematic of enthalpy probe (Ref. [63]).

Stagnation point heat transfer method – Assuming the frozen boundary layer with a fully catalytic surface of TPS, the empirical correlation was proposed by Pope to reform the Fay and Riddel’s equation, expressed as [69,70],

$$h = \frac{\dot{q}}{K} \sqrt{\frac{R_{\text{eff}}}{p_0}} \quad (1-5)$$

Here, \dot{q} is the heat flux density, R_{eff} is the effective leading edge radius of the probe, and K is the constant depending on the gas. The heat flux is usually measured by Gardon gage made of water-cooled copper as shown in Fig.1-14. In non-equilibrium flows, however, a part of enthalpy is possessed in chemical potential because the recombination does not occur completely on the surface of TPS. Then, the specific enthalpy would be underestimated. Although a correlation for a finite catalysity and non-equilibrium flows has been proposed by Goulard, it requires detail chemical parameters.

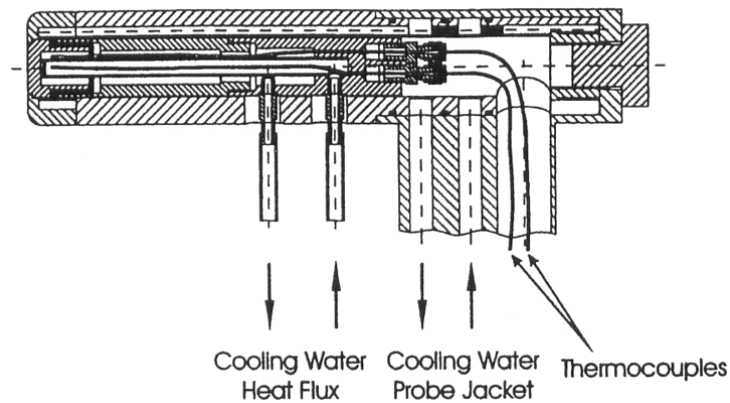


Fig. 1-14 Schematic of heat flux probe (Ref. [37]).

Total pressure

Pitot probe – For the total pressure measurement, Pitot probes shown in Fig.1-15 have been widely used. Care should be pair for the difference between subsonic and super sonic flows as described in following paragraph. As for the measurement technique, a hole of the probe should be larger than the mean free path of the gas.

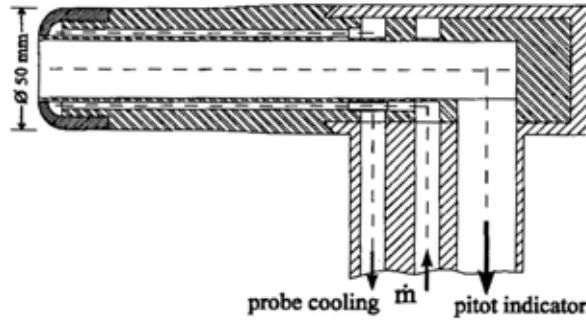


Fig. 1-15 Schematic of Pitot probe (Ref. [63]).

Flow velocity

Pitot probe – With the measurements of total pressure by Pitot probes, Mach number can also be estimated. The relationship between pressure ration and Mach number is expressed as,

$$\frac{P_{\text{pitot}}}{P_{\text{amb}}} = \left(1 + \frac{\gamma - 1}{2} M^2\right)^{\frac{\gamma}{\gamma - 1}} \text{ for a subsonic flow,} \quad (1-6)$$

$$\frac{P_{\text{pitot}}}{P_{\text{amb}}} = \left[\frac{(\gamma + 1)M^2}{2}\right]^{\frac{\gamma}{\gamma - 1}} \left[\frac{\gamma + 1}{2\gamma M^2 - (\gamma - 1)}\right]^{\frac{1}{\gamma - 1}} \text{ for a sonic flow,} \quad (1-7)$$

Here, P_{pitot} , P_{amb} and γ represents total pressure, ambient pressure and ratio of specific heat.

Mach probe – In supersonic flow, disturbance caused by a wedge probe spreads as the sound wave. This disturbance region is limited by the Mach line as shown in Fig.1-16. Then, Mach number is estimated by the angle α between the Mach line and the flow axis expressed as,

$$M = \frac{1}{\sin \alpha}. \quad (1-8)$$

Although the wedge of the probe should be sharp to clear the Mach line, the sharpness is limited by the cooling system to prevent the erosion.

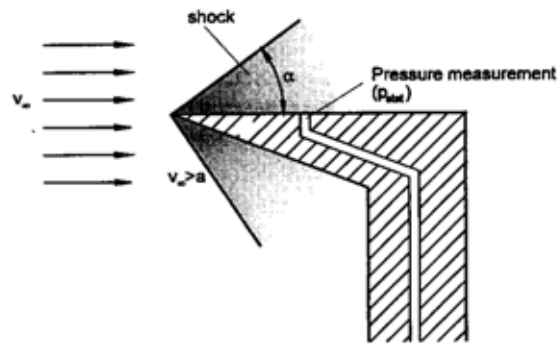


Fig. 1-16 Schematic of heat flux probe (Ref. [63]).

Time of flight probe – This method consists of two electrostatic double probes put in a flow at a distance as shown in Fig. 1-17 [63]. The velocity of the flow is estimated by delay time of a disturbance of the flow detected by the upstream and downstream probes. The disturbance is caused by the power supply system of the wind tunnels on purpose or their natural fluctuations are used.

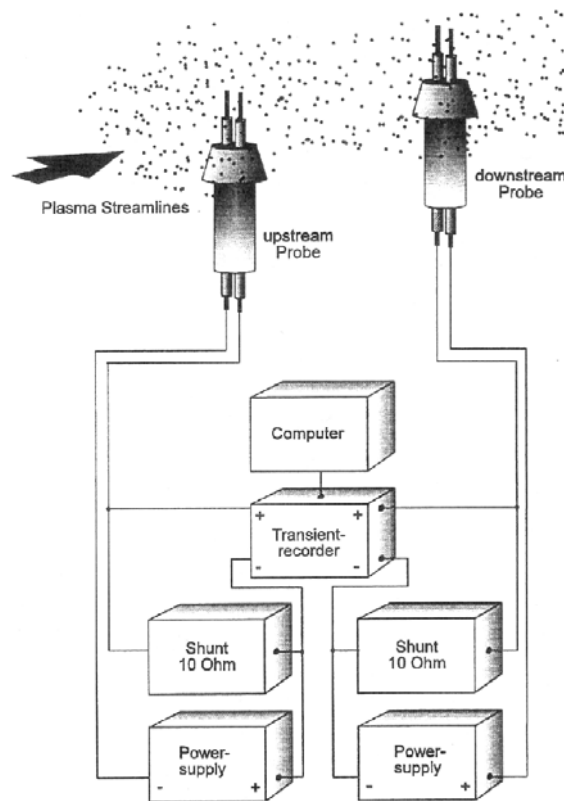


Fig. 1-17 Conceptual figure of time of flight probe (Ref. [63]).

Species number density

Mass spectrometer – The density and energy distributions of neutral and ionized particles are estimated [63, 71]. A schematic of mass spectrometer is shown in Fig. 1-18. The incoming particles are ionized in an ion source and then classified by an energy analyzer. Then, the relative density of each species can be measured. If the particles have same mass (for example, N₂ and CO are 28g/mol), the ionization potential energy is used to distinguish them. For the absolute measurements, a reference cell is used.

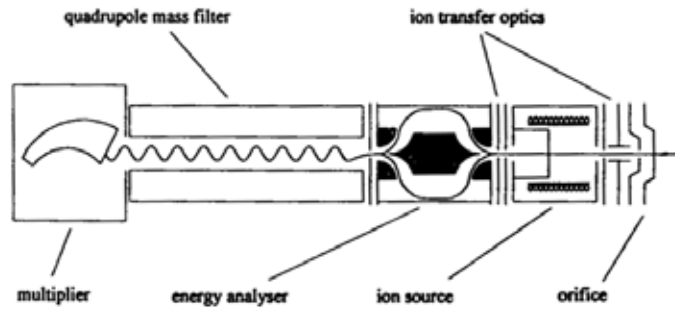


Fig. 1-18 Schematic of mass spectrometer (Ref. [71]).

Electron density and temperature

Electrostatic probe – Electrostatic probes firstly developed by Langmuir are most conventional tools for plasma diagnostics [72]. Although there are many kinds of electrostatic probes such as the single probe, double probe, triple probe and emissive probe, a brief concept of the single probe is described here.

A schematic of single probe and a current-voltage curve of the single probe is shown in Figs.1-16, 17. Here, V_s , V_f , I_{ion} and I_{es} are space potential, floating potential, ion saturation current and electron saturation current, respectively. In the transition region, the current-voltage curve is expressed as,

$$\frac{d(\ln I)}{dV} = \frac{V}{kT_e}. \quad (1-9)$$

Here, k is the Boltzmann constant. Then, electron temperature T_e is obtained by the gradient in this region. Electron density n_e is obtained by the electron current at the plasma potential I_{es} expressed as,

$$I_{es} = -en_e S \sqrt{\frac{kT_e}{2\pi m_e}}. \quad (1-10)$$

Here, S is the surface area of the probe, e is the electron charge and m_e is the electron mass. This value is estimated by linear extrapolations of the current in transition and electron saturation regions.

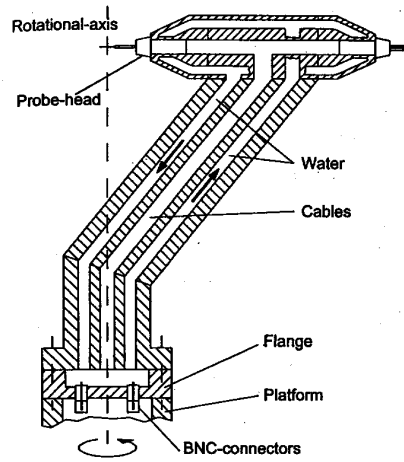


Fig. 1-16 Schematic of single probe (Ref. [63]).

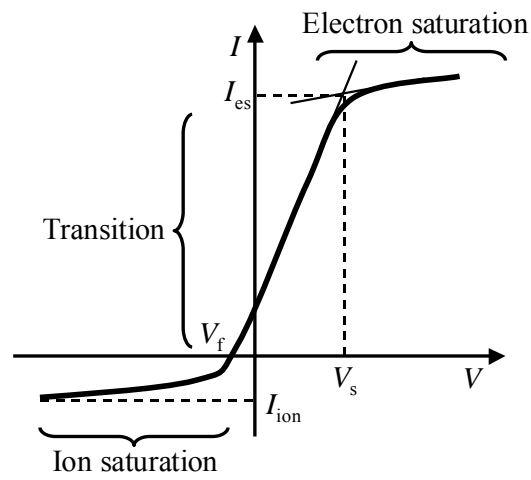


Fig.1-17 Typical current-voltage curve in a single probe measurement.

1.3.2 Non-intrusive methods

Although emission spectroscopy was formerly the only non-intrusive method, various methods have been developed with the development of laser. In general, these methods are roughly classified into spectroscopy, scattering, interference, transmission and reflection [63, 73]. As a high enthalpy diagnostics method, spectroscopy is most often used because the other methods, which are targeting electron density and temperature, are difficult to be applied to the flow due to the low degree of ionization and low temperature. In this section, therefore, only the spectroscopy is referred.

Spectroscopy is based on transitions of electrons in atoms or molecules such as spontaneous emission, absorption and fluorescence. For each process, emission spectroscopy including Fabry-Perot Interferometer (FPI), Laser Absorption Spectroscopy (LAS) and Laser Induced Florescence (LIF) has been developed. Apart from the other methods, these spectroscopes have usually information of several flow properties. Then, the limit of application should be cared. In the following paragraph, measurable parameters are briefly summarized and tabulated in Table1-3. Next the comparisons of theses spectroscopes are described.

Specific enthalpy

Total specific enthalpy of a flow is a sum of static enthalpy , kinetic energy and chemical potentials expressed as,

$$h_0 = \int C_p dT + h_{chem} + \frac{1}{2}u^2 . \quad (1-11)$$

Here, C_p is the specific heat at constant pressure, h_{chem} is chemical potential and u is the flow velocity. Then, translational temperature, flow velocity and excitation, degree of dissociation and that of ionization are necessary. These parameters can be obtained by LAS and LIF described below.

Flow velocity

Flow velocity is estimated by FPI, LAS and LIF using the Doppler shift of a spectral line [73]. Since resolutions of conventional monochromaters is usually not enough high to measure the Doppler shift ($\Delta\lambda_{shift} \sim 7\text{pm}$ for $\lambda_0 \sim 1\mu\text{m}$, $v \sim 2000\text{m/s}$), ES is difficult to be used. The theoretical detail is described in the next chapter.

Species density

Species density is estimated by LAS and LIF [73]. Although ES was also used previously, the absolute calibration is too difficult and contains much error. Then recently it has not been used. The theoretical detail is described in the next chapter.

Electron density and temperature

Electron density and temperature are estimated by ES, FPI, LAS and LIF using Stark shift or broadening [73]. This method is usually applied to hydrogen atom because the Stark effect is completely analyzed theoretically and its effect is prominent [74]. As for the other atoms, both shift and broadening are much smaller in low-pressure plasma. Moreover, their theoretical approximation includes much error and is questionable. The approximated expression for atomic oxygen is described in the next chapter.

Excitation temperature

Excitation temperature is estimated by ES using relative line intensities. This method is applicable only for the thermal equilibrium, local thermal equilibrium (LTE) or partial-LTE flows. Under these conditions, the population density of excited level obeys the Maxwell distribution and emission intensity from the level is expressed as,

$$\varepsilon_{ji} = \frac{1}{4\pi} \frac{hc}{\lambda_{ji}} \frac{g_j}{z(T)} A_{ji} n_j \exp\left(-\frac{E_j}{kT_{\text{ex}}}\right). \quad (1-12)$$

Here, ε , h , c , λ , g , z , A , n , E , k , T_{ex} , i , j are emission intensity, Planck constant, velocity of light, wavelength, statistical weight, total partition function, Einstein coefficient, population density, excitation energy, Boltzmann constant, excitation temperature, lower level and upper level, respectively. Then, at the constant excitation temperature, eq.(1-12) is rewritten as,

$$\ln\left(\frac{\varepsilon_{ji}\lambda_{ji}}{A_{ji}g_j}\right) = -\frac{E_j}{kT_{\text{ex}}} + \ln K. \quad (1-13)$$

Here, K is the constant. Then, from a few emission lines for a same atom, excitation temperature can be estimated by the gradient in excitation energy-logarithm of number density diagram [63,75]. This method has an advantage that it requires not absolute calibration but just relative intensity. However, for accurate measurements, many emission lines whose excitation energy is distributed over wide range are necessary. It is also remarked that excitation temperature does not always agree with electron temperature.

Translational temperature

Translational temperature is estimated by FPI, LAS and LIF using Doppler broadening [61]. The theoretical detail is described in the next chapter.

Rotational/vibrational temperature

Rotational and vibrational temperature is more complex than excitation one. In their theoretical expressions, rigid body and harmonic oscillation are firstly assumed and then corrected. The term values of vibrational and rotational energy are expressed as [76],

$$G(\nu) = \omega_e \left(\nu + \frac{1}{2} \right) - \omega_e x_e \left(\nu + \frac{1}{2} \right)^2 + \omega_e y_e \left(\nu + \frac{1}{2} \right)^3 + \dots, \quad (1-14)$$

$$F_\nu(J) = B_\nu J(J+1) - D_\nu J^2(J+1)^2 + \dots. \quad (1-15)$$

Here, G and F are term values of vibrational and rotational energy, ν is the vibrational quantum number, J is the rotational quantum number, ω_e , $\omega_e x_e$, $\omega_e y_e$ are vibrational constant, B_ν is the rotational constant and D_ν is the constant considering centrifugal force into rotational constant. In both equations, the first terms represent theoretical model (rigid body or harmonic oscillator) and the other terms originate from non-rigid body, anharmonic oscillator and their interaction effects. These constants are experimentally determined [77].

These temperatures are estimated by ES with the fitting to the computed line profiles or by LAS FPI and LIF using relative line intensities [78, 79].

Table 1-3 Diagnostic method.

| Parameter | Intrusive method | Non-intrusive method |
|--|--|--|
| Specific enthalpy | 1. Energy balance 2. Enthalpy probe 3. Sonic flow 4. Stagnation point heat transfer | 1. Translational temperature, flow velocity and species density (LAS, LIF, FPI) |
| Heat Flux | 1. Gardon gage 2. Slug calorimeter 3. Radiometer probe | - |
| Flow velocity | 1. Pitot probe 2. Mach probe 3. Time of flight probe | 1. Doppler shift (LAS, LIF, FPI) |
| Stagnation pressure | 1. Pitot pressure probe | - |
| Species density | 1. Mass spectrometer 2. Solid state electrolyte probe | 1. LAS 2. LIF with a reference cell 3. CARS (Raman scattering) |
| Electron density and temperature | 1. Electrostatic probe 2. Plasma absorption probe | 1. ES with computation 2. Stark effect (ES, LAS, LIF, FPI) 3. Thomson scattering 4. Interference (Mach-Zehnder, etc.) |
| Excitation temperature | - | 1. ES |
| Translational temperature | - | 1. Doppler broadening (LAS, LIF, FPI) |
| Rotational and vibrational temperature | - | 1. Molecular band (ES, LAS, LIF) with/without computation |

1.3.3 Selection of diagnostics method

As surveyed above, LAS is much superior to conventional probe methods: 1) it doesn't disturb flows 2) translational temperature and number density can be measured though they are difficult to be measured by probe methods. Furthermore, compared with other spectroscopy such as ES, FPI and LIF, LAS has following advantages as tabulated in Table 1-4.

It can be possible for optically thick plasma and number density can be obtained without calibration though others are not applicable to such plasma and need an absolute calibration source or a reference cell. Furthermore, using a diode laser, LAS system is very low cost and compact. Then, the system can be portable everywhere. On the other hand, monochromator or excimer and dye lasers are expensive. Especially the excimer laser is a large equipment and almost impossible to carry. As for the wave length resolution, in LAS around 0.001nm is possible using etalon whereas that of monochromater is around than 0.1nm. Therefore, in this study, LAS is adopted as a high enthalpy diagnostics tool.

Table 1-4 Comparison of LAS, ES and LIF.

| | LAS | ES (FPI) | LIF |
|------------------------|---------------|-----------------------|----------------|
| Optically thick plasma | Applicable | Inapplicable | Inapplicable |
| Calibration | No need | Absolute light source | Reference cell |
| Portability | Easy | Possible | Impossible |
| Equipment | Not expensive | Expensive | Very expensive |
| Wave-length resolution | <1pm | ~0.1nm | <1pm |

1.4 Laser Absorption Spectroscopy

1.4.1 History of absorption spectroscopy

An origin of spectroscopy is the discovery by Newton in 1666 [80]. He found that sunlight could be divided into spectral colors by a prism. After that, in 1802 [81], Wollaston discovered the existence of dark lines in the solar spectrum. In 1814, Fraunhofer investigated the dark lines in detail. He found over 700 dark lines, which were known as Fraunhofer lines and included a famous Na-D line [82]. After the observation of emission lines of metal salts of sodium, potassium, lithium and strontium etc. in an alcohol lamp by Talbot and Hershel in 1826 [83], Kirchhoff concluded that the Fraunhofer lines were caused by absorption of vapor sodium etc [84]. Kirchhoff and Bunsen invented many instruments such as variable slit, collimator lens and Bunsen burner [85]. From then on, qualitative analysis has been introduced to spectroscopy.

An atomic absorption spectroscopy was proposed by Walsh in 1955 [86]. In this method, atomic lines emitted from the same kinds atom with sample one in flames or hollow cathode lamps are used as light source. This light is introduced to the flame in which the sample materials are vaporized. Then, the concentration of the vaporized sample is obtained by the absorption of the light through the flame. This method has advantages of higher sensitivity and accuracy than that using continuum light sources. However, the sensitivity and accuracy are not still enough high to detect detail shapes of absorption lines because it is difficult to scan the frequency of the light source.

Laser (Light Amplification by Stimulated Emission and Radiation), which was proposed by C. H. Towns and A. L. Schawlow in 1958 [87] and realized by T. H. Maiman in 1960 [88], has caused dramatically progress in the spectroscopy because of its directivity, monochromaticity, narrow line width, tenability of frequency and stability. Especially, after invention of a diode laser by Z. I. Alfenov et al. in 1970 (double heterostructure; continuous wave oscillator and operation at room temperature is possible) [89], laser absorption spectroscopy has become widespread in many research fields.

1.4.2 Applications of Laser absorption spectroscopy in other fields

Laser absorption spectroscopy has been applied in such fields as chemical physics, plasma processing, environmental problems, and gas dynamics and combustion.

In chemical physics, atomic and molecular structure, internal state, energy transfer and cross sections have been investigated [90, 91]. Especially, near infrared region corresponds to vibrational transition energy of OH, CH, NH and SH, which are important in chemistry.

Plasma processing has played important roles for developments of semiconductors [92, 93]. Because, miniaturization, integration, high quality and large diameter of silicon wafer have been required with the developments, controls of plasma conditions have become important. Laser absorption spectroscopy makes it possible to measure concentrations of radical species such as CF_x ,

SiH_x and translational temperature in such low-pressure plasma. Recently, a new control approach has been proposed that plasma conditions are adjusted by feedbacks of time and spatially resolved monitored concentrations of radical species.

Environmental problems such as air pollutant, green house effect and depletion of ozone layer have recently remarkably got attention in the world. Target areas of these problems are atmosphere from the ground to high altitude. Then, remote sensing by laser called "laser" (Laser Identification, Detection and Ranging) is very useful because it is easy to cover wide area due to its directivity [94, 95]. Distributions of concentrations of NO_x , CO_2 and O_3 have been actively measured. Recently, utilization of satellites has been planned and tested as laser oscillators to cover wider areas.

Gas dynamics and combustion are important in industries from automobiles to aerospace. After inventions of a single longitudinal mode diode laser in 1980's, applications of a diode laser absorption spectroscopy to this fields has been widespread with developments of general technology of optical measurements such as fiber coupling and high sensitive methods because a diode laser is compact, low cost and wide oscillation range from visible to infrared ($0.4\mu\text{m}\sim 30\mu\text{m}$) [96, 97]. In these fields, various gas dynamic properties such as concentrations, temperature and flow velocity have been measured.

1.4.3 Applications of LAS to plasma wind tunnel flows and its problems

In aerospace fields, a diode laser absorption spectroscopy has been widely applied to rocket engine and shock tunnels diagnostics. Since late 1970's, Hanson et al. has applied LAS to combustion flows, shock tube flows, atmospheric ICP torches. They have measured translational temperature, number density of absorbers and electron density [98-101]. In 1997, Zhang applied LAS to arcjet thruster plumes and measured translational temperature and flow velocity [102].

However, there are few applications to plasma wind tunnel flows. In 2004, Kim and Hanson et al. applied LAS to the segmented type plasma wind tunnel (IHF in NASA Ames) flows [103]. They targeted argon, oxygen atom, nitrogen atom and copper in the arc discharge part and in the plume. Although absorption profiles for such species could be detected in the arc discharge part, the profiles were split by Zeeman effects. Then he estimated the population temperature between ground and absorbing states assuming thermal equilibrium instead of the translational temperature. In the plume, he measured the translational temperature by seeded sodium profiles, whose absorption sate is ground one and its line belongs near infrared region (769.9nm), because the absorption lines from meta-stable for other species could not be detected. Then, he concluded the number density of meta-stable state is much less than expected under thermo-chemical equilibrium assumptions and most atomic species are in ground state.

Therefore, before applying LAS to plasma wind tunnel flows, applicable limit and accuracy of it should be examined. Especially for absorption profiles, several abnormal behaviors in

low-pressure plasma have been reported. Lindsay reported incomprehensible features of two Ne lines that 1) Lorentz width was in proportional to the ambient pressure and 2) broadening constants were different in different temperatures [104]. Kasai reported that absorption profiles of meta-stable argon in low-pressure thin plasma were distorted and its Gauss width was larger than Monte Carlo expectation [105]. Then, experimental examinations of absorption profiles for various conditions are necessary as well as theoretical one. In this thesis, an effect of laser intensity on line broadening is focused and carefully investigated. Although their phenomenon called absorption saturation is theoretically analyzed [73], there are few reports concerning its quantitative investigations.

1.5 Objectives

Objectives of this thesis are 1) to establish a diagnostic system for the plasma wind tunnel using diode laser absorption spectroscopy (LAS) and 2) to characterize flow properties in low-pressure plasma wind tunnel.

1) Development of LAS system

To validate applicable limit and accuracy of LAS with particular emphasis on error analysis and an effect of absorption saturation on measurement parameters

2) Application to plasma wind tunnel flows

To characterize plasma wind tunnel flows by measurements of time and spatially resolved translational temperature and chemical composition

Chapter 2

Applicable Limit of Laser Absorption Spectroscopy

This chapter presents a theory of laser absorption spectroscopy applied to plasma wind tunnels in Chapter 3-5 and its experimental equipments.

2.1 Principle of Laser Absorption Spectroscopy

From the quantum theory [105], of the infinite number of orbits of an electron about an atomic nucleus, which are possible according to classical mechanics, only certain discrete orbits actually occur. A transition of the electron from one state to another can take place by absorbing a incident laser beam whose energy corresponds to the difference between the two states. This absorption profile of atomic lines has information such as its wavelength, intensity and shape. From such information, number density, translational temperature and flow velocity of the absorbing atom can be deduced. The relationship between these physical parameters and absorption profiles are illustrated in Fig.2-1. In this section, application condition of laser absorption spectroscopy is discussed and the detail of the relationships described above is presented. Finally the measurement limit is considered.

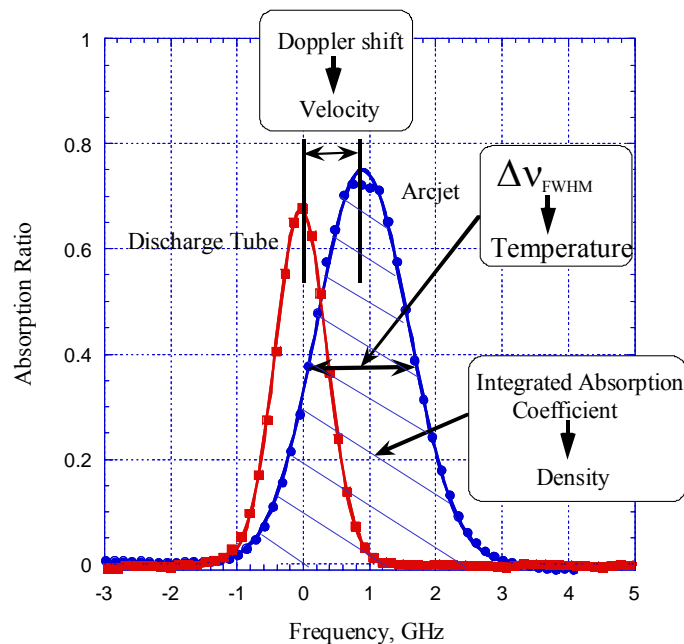


Fig. 2-1 Relationship between physical properties and absorption profiles

2.1.1 Laser absorption

The intensity decrease dI of a laser beam with intensity I propagating along x direction through an absorbing sample is expressed as, [73, 105]

$$dI = -I\sigma_{ij} \left(n_i - \frac{g_i}{g_j} n_j \right) dx . \quad (2-1)$$

Here, i, j are lower and upper energy levels, n_i, n_j are the population density, g_i, g_j are the statistical weight and σ_{ij} is the absorption cross section. As long as the population density n_i and n_j of the two levels E_i and E_j are not noticeably altered by the interaction with the radiation field (weak approximation), they can be regarded as constant. The absorbed intensity is then proportional to the incident intensity, that is linear absorption. The integration of (2-1) over the absorption path x gives Beer's law for linear absorption,

$$I(x) = I_0 e^{-kx}$$

$$k = \sigma_{ij} \left(n_i - \frac{g_i}{g_j} n_j \right) \quad (2-2)$$

Here, k is absorption coefficient.

2.1.2 Absorption coefficient

Assuming that laser absorption consists of absorption and induced emission, the total absorption is expressed as,

$$k_\nu d\nu = \frac{h\nu}{c} (B_{ij} dn_i - B_{ji} dn_j) \quad (2-3)$$

Here, N_i is lower state number density, N_j is the upper state number density, B_{ij}, B_{ji} is the Einstein B coefficients. Substituting the following relationship between A and B coefficients,

$$A_{ji} = \frac{8\pi h \nu^3}{c^3} \frac{g_i}{g_j} B_{ij}$$

$$= \frac{8\pi h \nu^3}{c^3} B_{ji} \quad (2-4)$$

to the equation (2-2), the integrated absorption coefficient is expressed as,

$$\begin{aligned}
K &\equiv \int_{-\infty}^{+\infty} k_{\nu} d\nu \\
&= \frac{c^3}{8\pi h \nu^3} \frac{g_j}{g_i} A_{ji} n_i \left(1 - \frac{g_i}{g_j} \frac{n_j}{n_i} \right)
\end{aligned} \tag{2-5}$$

Assuming the Boltzmann equilibrium between n_i and n_j states, n_i is related to n_j as,

$$n_j = \frac{g_j}{g_i} n_i \exp\left(-\frac{\Delta E_{ij}}{kT_{\text{ex}}}\right) \tag{2-6}$$

Here, ΔE_{ij} is the energy between N_i state and N_j state, k is Boltzmann constant and T_{ex} is the electron excite temperature. From the equations (2-7) and (2-8), the following relationship is obtained [116-110].

$$K = \frac{\lambda^2}{8\pi} \frac{g_j}{g_i} A_{ji} n_i \left[1 - \exp\left(-\frac{\Delta E_{ij}}{kT_{\text{ex}}}\right) \right] \tag{2-7}$$

In our research, $\Delta E_{12}/k$ corresponding to oxygen 777.19 nm and argon 840.82 nm absorptions is about 20,000K [111]. This is much smaller than T_{ex} . Therefore, the integrated absorption coefficient is expressed as follows.

$$K = \frac{\lambda^2}{8\pi} \frac{g_j}{g_i} A_{ji} n_i \tag{2-8}$$

2.1.3 Line broadening

Absorption profile of atomic line is broadened by various physical mechanisms, and is expressed by a convolution of the Lorentzian and the Gaussian distributions. Here brief derivations and results are presented [73].

Doppler broadening

The proper frequency ν_0 of a moving atom at velocity v is observed to be shifted by the Doppler effect to

$$\begin{aligned}\nu_v &= \nu_0 + \delta\nu \\ \delta\nu &= \nu_0 \frac{v}{c}\end{aligned}\tag{2-9}$$

Here, c is the velocity of light. Assuming that the velocity distribution of the atom obeys to the Maxwell distribution, the probability that the velocity component of the atom to the light direction is in $v+\Delta v$ is

$$p(v)dv = \left(\frac{M_A}{2\pi kT}\right)^{1/2} \exp\left(-\frac{M_A v^2}{2kT}\right)dv\tag{2-10}$$

Here, M_A is the atom mass, k is Boltzmann constant and T is the temperature. Therefore, a normalized profile is a Gaussian and expressed as,

$$g(\nu) = \frac{1}{\pi^{1/2} \Delta\nu_D} \exp\left[-\left(\frac{\nu - \nu_0}{\Delta\nu_D}\right)^2\right]\tag{2-11}$$

This is called the Doppler broadening. The full width at half maximum (FWHM) $\Delta\nu_D$ is related to the temperature as follows.

$$\begin{aligned}\Delta\nu_D &= \frac{2\nu_0 \sqrt{\ln 2}}{c} \sqrt{\frac{2kT}{M_A}} \\ &= 7.16 \times 10^{-7} \sqrt{\frac{T}{M_A}} \nu_0\end{aligned}\tag{2-12}$$

Natural Broadening

Natural broadening is originated by the finite time of the transition. The Heisenberg uncertainty principle is expressed as,

$$\Delta E \cdot \Delta t \approx \hbar \quad (2-13)$$

Considering that the life time of the atom is $\Delta t=1/A$, the uncertainty of the frequency $\Delta\nu_N$ is expressed as,

$$\begin{aligned} \Delta\nu_N &= \frac{\Delta E}{h} \\ &= \frac{A}{2\pi} \end{aligned} \quad (2-14)$$

This profile is the Lorentz type. Generally, typical A coefficient is from $10^7 \sim 10^8 \text{s}^{-1}$ [111]. Therefore $\Delta\nu_N$ is the order of 2~20MHz.

Collision Broadening (Pressure Broadening)

The collision broadening is originated from the fact that atoms are perturbed by collisions with other atoms (or molecules). In the phenomenological treatment, two types of collisions are discussed. One is the collision-induced transition and the other is the phase-changing collision. In the former collision, if the energy difference between atomic levels is not very large compared with the kinetic energy of the colliding atom, the collision induces a transition between the atomic levels. In the latter one, phase of the state suffers a phase shift by collisions because the phase of atomic wave function is more frequently perturbed than is the population of the atomic level by collisions with other atoms. This profile is the Lorentzian and the FWHM of these broadening $\Delta\nu_C$ is expressed as, [73]

$$\Delta\nu_C = (C_1 + C_2 + 2C_{12})p \quad (2-15)$$

Here, p is the pressure, C_1 , C_2 are the parameters related to with the collision-induced transition, and C_{12} is the parameter related to the phase-changing collision. Values of these three parameters are experimentally found in the range from 1 to 30 MHz/torr depending on the kind of atoms (or molecules) and temperature.

Stark Broadening

Stark broadening originates from the fact that the degeneracy is solved by the electric field which a surrounding electron makes. This profile is the Lorentz type and is expressed as, [73]

$$\Delta \nu_s = 1.0 \times \left[1 + 1.75 \times 10^{-4} n_e^{1/4} \alpha \left(1 - 0.068 n_e^{1/6} T_e^{-1/2} \right) \right] n_e w \cdot 10^5 \quad (2-16)$$

Here, w is electron impact parameter, α is ion-broadening parameter, n_e is electron density, and T_e is electron temperature.

Saturation Broadening

Saturation broadening is originated from the increase in the line width with the optical field intensity by the nonlinear effect as described in section 2.1.1. This profile is the Lorentz type and the broadening $\Delta \nu_p$ is expressed as,

$$\Delta \nu_p = \frac{1}{\pi} \sqrt{\gamma^2 + |x|^2} \quad (2-17)$$

Here, γ is the reciprocal of the mean collision time and $|x|$ is the Rabi frequency.

However, absorption saturation was found to cause the more broadening than that described above. A detail is described in Chapter 3.

Transit-time Broadening

Transit-time broadening is originated from the transit of the particles through light beam. This profile is Lorentz type and the broadening $\Delta \nu_T$ is expressed as, [73]

$$\Delta \nu_T = \frac{v}{2\pi a} \quad (2-18)$$

Here, v is the velocity of the atom and a is the beam diameter.

Table 2-1 Comparison of broadening effects

| Broadening | Origin | FWHM | Typical Value |
|--------------|---|---|---|
| Doppler | Thermal motion of atoms and molecules | $\frac{2\nu_0\sqrt{\ln 2}}{c} \sqrt{\frac{2kT}{M_A}}$ | ~2.2 GHz (Oxygen 1000 K) |
| Natural | Finite time of transition | $\frac{A}{2\pi}$ | ~1.6 MHz (A=10 ⁻⁷ s ⁻¹) |
| Collision | Interparticle collision | $(C_1 + C_2 + 2C_{12})p$ | ~10 MHz (0.1 torr) |
| Stark | Electric field | * | ~36MHz (Oxygen Ne=20 m ⁻³) |
| Saturation | Absorption saturation | $\frac{1}{\pi} \sqrt{\gamma^2 + x ^2}$ | ~10 MHz (10 mW) |
| Transit-time | Transit of particles through the laser beam | $\frac{\nu}{2\pi a}$ | ~1 kHz (a=1 mm) |

* $\Delta\nu_S = 1.0 \times \left[1 + 1.75 \times 10^{-4} n_e^{1/4} \alpha \left(1 - 0.068 n_e^{1/6} T_e^{-1/2} \right) \right] n_e \nu \cdot 10^5$

2.1.4 Line shape function

The actual absorption profile would be the convolution of the Gaussian and Lorentzian. The profile is called the Voigt profile and expressed as,

$$k_\nu = \frac{2k_0}{\pi\Delta\nu_L} \int_{-\infty}^{+\infty} \frac{\exp\left\{-\left(\frac{2\delta}{\Delta\nu_D}\sqrt{\ln 2}\right)^2\right\}}{1 + \left\{\frac{2(\nu - \nu_0 - \delta)}{\Delta\nu_L}\right\}^2} d\delta \quad (2-19)$$

This equation is also expressed by the following parameters as,

$$y \equiv \frac{2\delta}{\Delta\nu_D}\sqrt{\ln 2}, \quad a \equiv \frac{\Delta\nu_L}{\Delta\nu_D}\sqrt{\ln 2}, \quad \varpi \equiv \frac{2(\nu - \nu_0)}{\Delta\nu_D}\sqrt{\ln 2} \quad (2-20)$$

$$k_\nu = \frac{a}{\pi} \int_{-\infty}^{+\infty} \frac{\exp(-y^2)}{a^2 - (\varpi - y)^2} dy \quad (2-21)$$

Here, a represents the ratio of Doppler and Lorentz profile. If a is equal to 0, the profile is Doppler one. From this profile each parameters of Doppler and Lorentz profile can be obtained.

However, in this research, the broadening of Lorentz profile is much smaller than that of Doppler one as shown in Table 4-1. Therefore, broadenings except for Doppler one are neglected and obtained profiles were fitted by Gauss profile.

2.1.5 Absorption Shift

The absorption wavelength of the moving atom in a direction shifts by the Doppler effect. Therefore, from the shift quantity and the angle between the moving direction and the laser beam, the flow velocity is obtained by the following relationship.

$$V = \frac{\Delta\nu \cdot \lambda_0}{\cos\theta} \quad (2-22)$$

Here, V is the flow velocity, $\Delta\nu$ is the shift quantity, λ_0 is the absorption wavelength of the atom at rest and θ is the angle between the flow direction and laser beam.

2.1.6 Absorption Target

In this research, the target absorption lines are the transition from the metastable oxygen ($3s^5S$) and argon ($4s^2[1/2]$). This is because number density of metastable states is much larger than other excited states one, so that it is easy to detect the absorption profiles. The transition data of these lines and their Grotrian diagrams are shown in Table 2-2 and Figs 2-2 and 3 [111].

Table 2-2 Transition data.

| | 1 | 2 | λ (nm) | E_1 (eV) | E_2 (eV) | g_1 | g_2 | A_{21} ($10^8 s^{-1}$) |
|-----|-------------|-------------|-------------------|---------------|---------------|-------|-------|-------------------------------|
| OI | $3s^5S$ | $3p^3P$ | 777.19 | 9.15 | 10.74 | 5 | 7 | 0.369 |
| OI | $3s^3S$ | $3p^3P$ | 844.62 | 9.52 | 10.99 | 3 | 1 | 0.322 |
| OI | $3s^3S$ | $3s^3S$ | 844.64 | 9.52 | 10.99 | 3 | 5 | 0.322 |
| ArI | $4s^2[1/2]$ | $4p^2[3/2]$ | 840.82 | 11.62 | 13.09 | 3 | 5 | 0.223 |
| ArI | $4s^2[3/2]$ | $4s^2[5/2]$ | 842.46 | 13.28 | 14.74 | 3 | 5 | 0.215 |
| ArI | $4s^2[1/2]$ | $4s^2[3/2]$ | 852.14 | 11.62 | 13.28 | 3 | 3 | 0.139 |

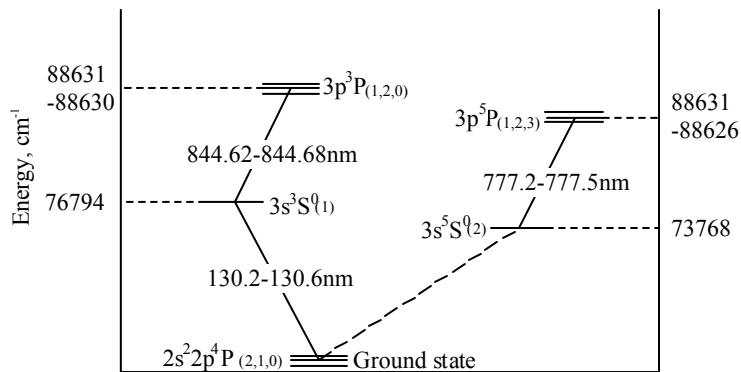


Fig. 2-2 Grotrian diagram of atomic oxygen.

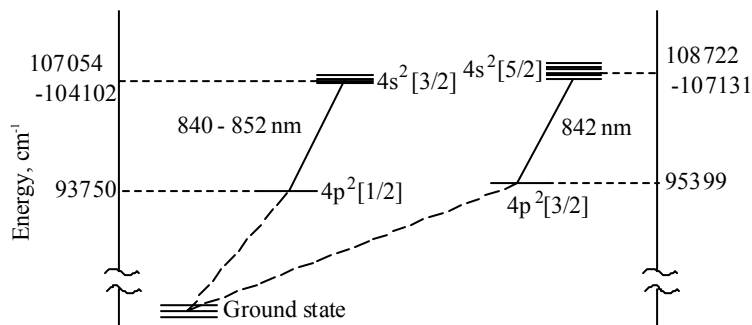


Fig. 2-3 Grotrian diagram of argon.

2.2 Measurement System

Figure 2-4 shows the schematic of an optical system used in this research. Tunable diode-lasers with an external cavity were used as the laser oscillator. The line width of both lasers is smaller than 300kHz. The modulation frequency and width were 10Hz and 20GHz, respectively. The optical isolator is used to prevent the reflected laser beam from returning into the external cavity. The laser beam is divided into three beams by beam splitters. The first beam is directly detected by a photo-detector as a reference signal. The second is detected by a Fabry-perot, etalon, whose free spectral range is 1GHz. The third is lead to the chamber window through a multimode optical fiber. The fiber output is mounted on a two-dimensional traverse stage to scan the laser beam through the plume in radial and axial directions. At the other side, a parabola mirror is set so that the laser beam can be detected without synchronizing the detector position with the laser scan. Spatial resolution is about 1mm. The photograph of this system is shown in Fig.2-5.

Figure 2-6 shows the schematic of the measurement system used in the flow velocity measurement in the university of Tokyo arc-heater. Apart form the above system, an optical fiber is lead in the vacuum chamber and the fiber output is mounted on the edge of a duralumin stage. On the opposite edge, a photo detector is set and the laser beam through the arc plume is detected. This stage is fixed on the one-dimensional traverse stage to scan the plume in the axial direction, keeping the angle between the laser beam and the axial direction to be at 45 degree.

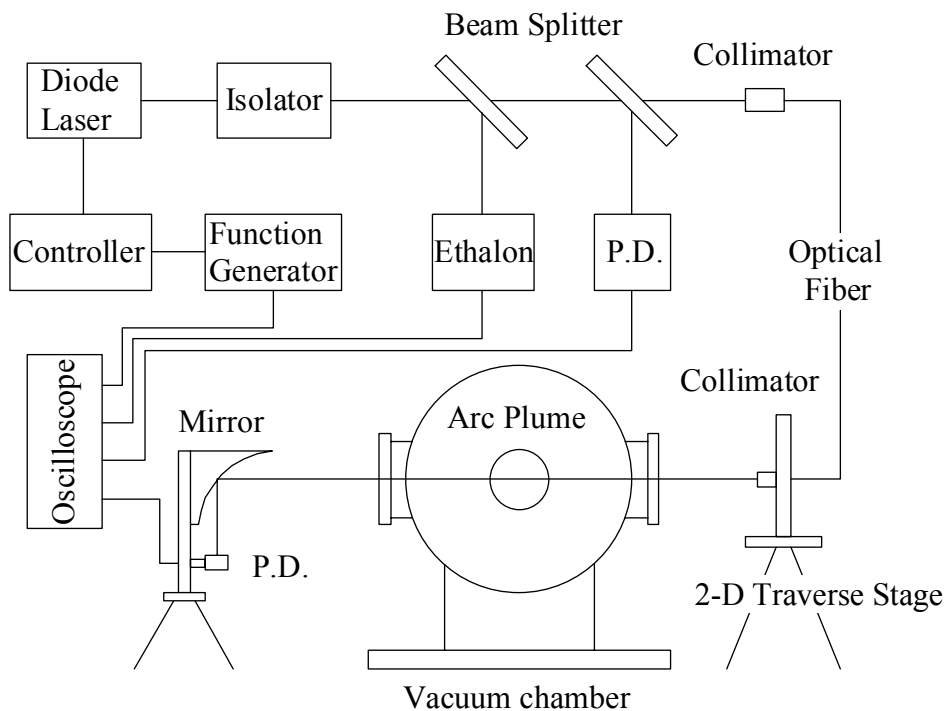


Fig. 2-4 Schematic of measurement system for laser absorption spectroscopy.



Fig. 2-5 Photograph of measurement system for laser absorption spectroscopy.

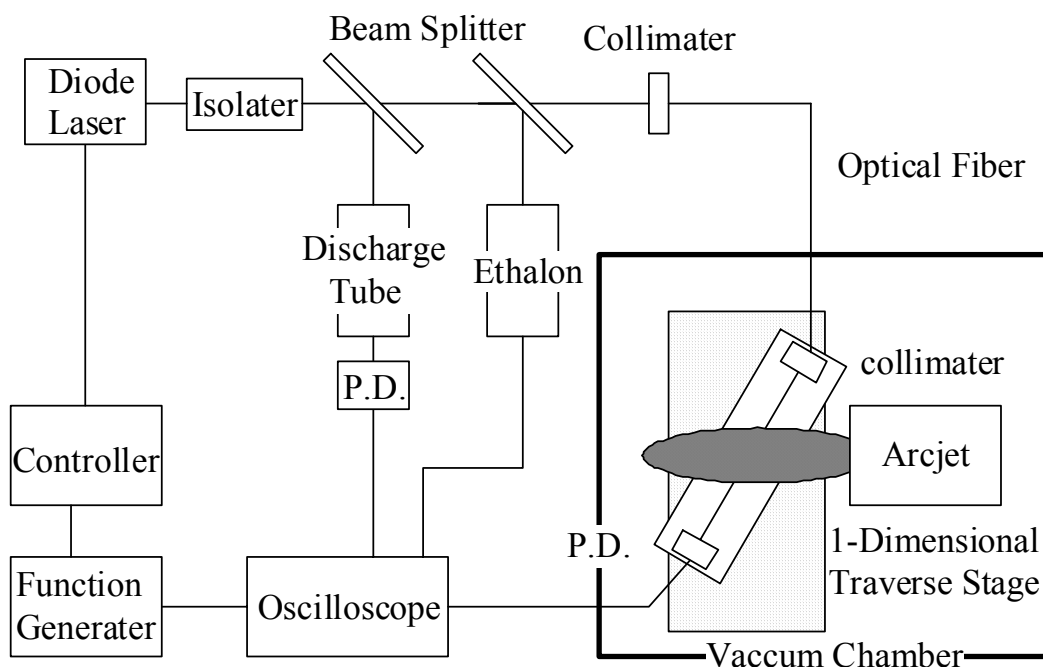


Fig. 2-6 Schematic of velocity measurement system.

2.2.1 Tunable diode laser

As a tunable diode laser, FP, DFB, DBR and VCSEL lasers are widely used [112-115]. In these lasers, the wavelength is modulated by changing the current on the diode laser or their temperature by controlling thermistors. A typical value is 0.15 pm/mA or 0.06nm/K. These lasers has a merit of low cost and high-speed modulation. However, the modulation is often accompanied with mode-hops and unstable and modulation width is relatively narrow. Therefore, in this study, an external cavity type laser (Velocity Model 6300, New Focus, and DMD845, EOSI) is used. In this system developed by Littman, the laser wavelength is modulated by a tuning mirror angle, as shown in Fig.2-7. This tuning mirror is connected to a piezo pivot and can be controlled by a function generator (AGF310, SONY-TEKTRONIX). In addition, anti-reflection coatings with residual reflectivity below 0.001 guarantee single-mode and mode-hop-free operation. The line width is less than 500 kHz and tuning range are 70 GHz in fine tuning mode and 20 nm in rough tuning mode. The specifications of these systems are shown in Table 2-3.

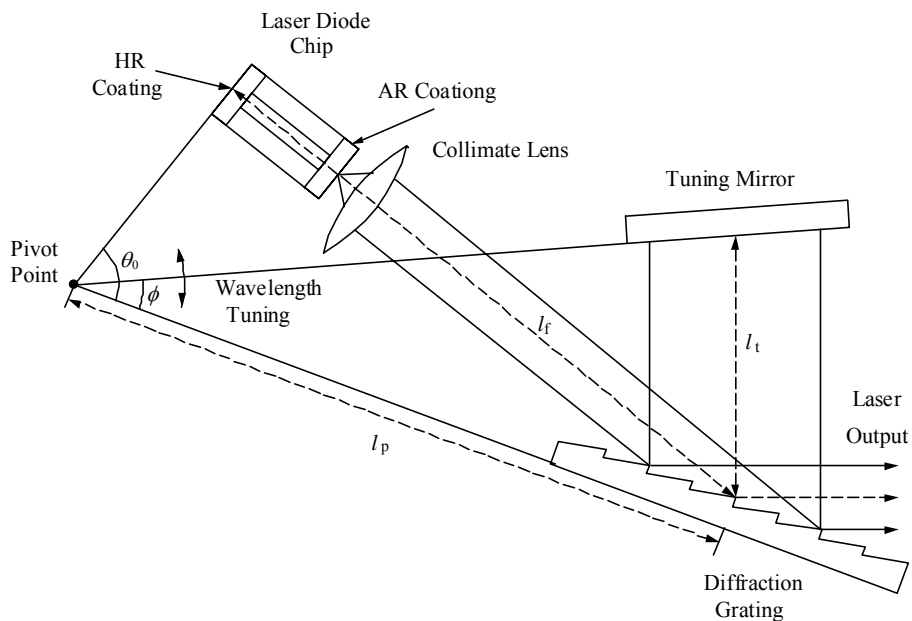


Fig. 2-7 Conceptual diagram of LittmannvMetcalf cavity.

Table 2-3 Specification of diode laser with external cavity.

| Model | Velocity6300 | DMD845 |
|-------------------|--------------|------------|
| Company | New Focus | EOSI |
| Tuning range | 771-789 nm | 833-855 nm |
| Intensity | 10 mW | 50 mW |
| Line width | <300 kHz | <500kHz |
| Fine tuning range | 70 GHz | 70 GHz |
| Modulation speed | 200 Hz | 200 Hz |

2.2.2 Etalon

An etalon is a kind of Fabry-Perot interferometer invented by C. Fabry and A. Perot in 1897. It's based on the principle of multiple beam-interference. A typical configuration is either a solid plane-parallel glass with two coated reflecting surfaces (Fig. 2-8(a)) or two separate plates aligned as parallel as possible (Fig. 2-8(b)). In the latter case, inner surfaces of each plate are coated with reflection layer and outer surfaces are with anti-reflection layer. In the following section, for simplicity, a principle of former configuration is represented. It is also applicable to the latter case.

As shown in Fig. , a plane wave incident at the angle α on a plane plate in the x -direction is assumed expressed as,

$$E = A_0 \exp[i(\omega t - kx)]. \quad (2-23)$$

Here, E , A_0 , ω , k are electric field, amplitude, angular frequency and wave number of the wave, respectively. From Fig. 2-9, the amplitude of i^{th} reflected wave A_i and transmitted wave B_i have following relations.

$$\begin{aligned} |A_{i+1}| &= R|A_i|, (i \geq 2) \\ |A_1| &= \sqrt{R}|A_0|, |A_2| = (1-R)\sqrt{R}|A_0|. \end{aligned} \quad (2-24)$$

$$\begin{aligned} |B_{i+1}| &= R|B_i|, (i \geq 1) \\ |B_1| &= (1-R)|A_0|. \end{aligned} \quad (2-25)$$

Here, R is the reflectivity. The optical path difference between i^{th} and $(i+1)^{\text{th}}$ reflected waves Δs is expressed from Fig. 2-9 as,

$$\begin{aligned} \Delta s &= 2na - b \cdot \sin \alpha \\ &= \frac{2nd}{\cos \beta} - 2d \cdot \tan \beta \cdot \sin \alpha \end{aligned} \quad (2-26)$$

Using Snell's law, Δs is rewritten as,

$$\Delta s = 2nd \cdot \cos\beta = 2nd\sqrt{1 - \sin^2\beta} . \quad (2-27)$$

A corresponding phase change caused by the optical path difference is expressed as,

$$\phi = 2\pi\Delta s / \lambda + \Delta\phi . \quad (2-28)$$

Here, $\Delta\phi$ is the phase change due to the index of refraction.

Then, the total amplitude of the reflected wave A is a summation of A_i expressed as,

$$A = -\sqrt{R}A_0 + \sqrt{R}A_0(1-R)e^{i\phi} + \sum_{m=3}^p A_m e^{i(m-1)\phi} . \quad (2-29)$$

If the incident wave is perpendicular to the plate, a number of reflection wave is infinite.

Then, A is rewritten as,

$$A = -\sqrt{R}A_0 \frac{1 - e^{i\phi}}{1 - Re^{i\phi}} . \quad (2-30)$$

Since the laser intensity I is expressed as $I=2c\varepsilon_0AA^*$, the total reflected intensity I_R is expressed as,

$$I_R = I_0 R \frac{4\sin^2(\phi/2)}{(1-R)^2 + 4R\sin^2(\phi/2)} . \quad (2-31)$$

Similarly, from a summation of B_i , the transmitted intensity I_T is expressed as,

$$I_T = I_0 \frac{(1-R)^2}{(1-R)^2 + 4R\sin^2(\phi/2)} . \quad (2-32)$$

These two equations are also called the Airy formulas.

Figure 2-10 shows the normalized laser intensity I_T/I_0 as a function of the phase shift for various reflectivities. As seen in this figure, peaks of the intensity become sharper with higher reflectivity, which means higher resolution.

The corresponding frequency range to the phase shift between two peaks is the Free Spectral Range of the interferometer $\Delta\nu_{\text{FSR}}$ expressed as,

$$\Delta\nu_{\text{FSR}} = \frac{c}{2nd} . \quad (2-33)$$

In this research, 1 GHz ($d=1\text{cm}$) and 0.75 GHz ($d=1.33\text{cm}$) etalons are used.

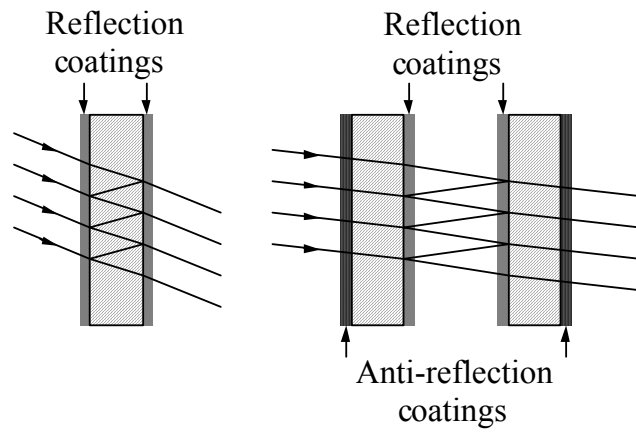


Fig.2-8 a) solid type etalon (left figure), b) air-spaced plane-parallel type etalon (right figure).

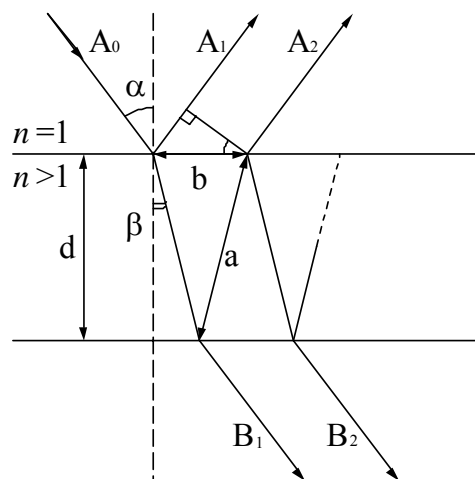


Fig. 2-9 An optical path difference in etalon.

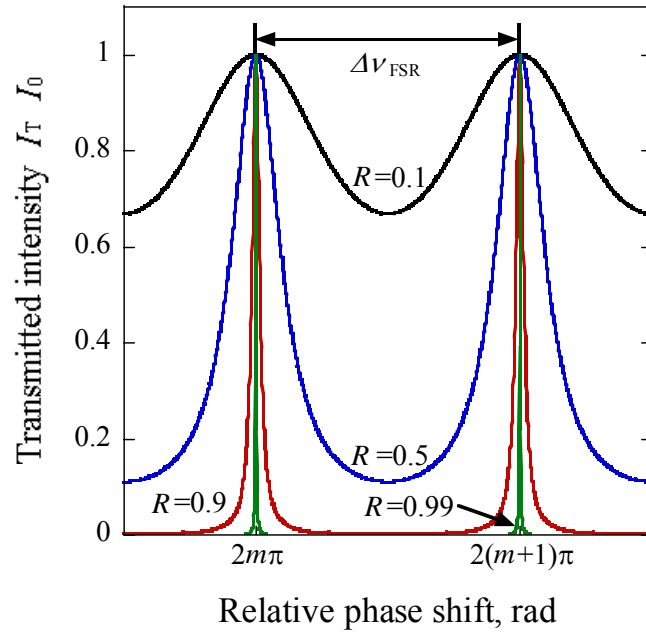


Fig. 2-10 Transmitted intensity as a function of phase shift for various reflectivities.

2.2.3 Optical Equipments

Optical equipments such as, an isolator, optical fiber, collimator, beam splitters, plane mirror, parabola mirror, IR card and digital oscilloscope were used. Their specifications are shown in Table 2-4.

Table 2-4 Specification of optical equipments.

| | Make | Serial number | Note |
|----------------------|-----------------|----------------------|--------------|
| Etalon | Neo Arc | Model | FSR=1 GHz |
| Optical fiber | THORLAB | P1-422-FC5 | Multimode |
| Isolator | ISOWAVE | I80-U4 | 780nm, 820nm |
| Collimator | THORLAB | LDH3-P2/Mz | |
| Beam splitter | NEW PORT | 10B 20BS.2 | R=50% |
| Mirror | SIGMA KOKI | 01MFG033/023 | R>99% |
| Parabola mirror | MELLES GRIOT | 02POA017 | R>90% |
| IR card | ELECTRO PHYSICS | IRC12R | 700~800 nm |
| Digital oscilloscope | YOKOGAWA | DL1540 | 16bit, 8CH |

2.3 Data Processing

2.3.1 Abel Inversion

Generally speaking, absorption profiles depend on thermo-chemical parameters such as number density and temperature. However, laser beam goes straight through the plasma and local information on the laser beam pass is integrated, assuming the plume is axisymmetry as shown in Fig.2-11. Therefore, to get the local absorption profiles, the obtained profiles have to be transformed by the Abel inversion [117].

Assuming the axisymmetry distribution, the equation (2-2) can be written as follows,

$$\ln \frac{I}{I_0}(y) = -2 \int_y^{\sqrt{r^2 - y^2}} \frac{k(r) \cdot r}{\sqrt{r^2 - y^2}} dr. \quad (2-34)$$

The Abel inversion of equation (2-3) is expressed as,

$$k(r) = \frac{1}{\pi} \int_r^R \frac{d(\ln \frac{I}{I_0}(y))}{dy} \frac{dy}{\sqrt{y^2 - r^2}}. \quad (2-35)$$

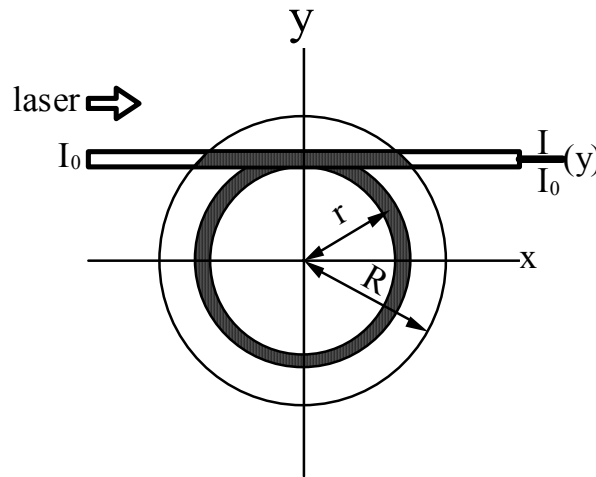


Fig. 2-11 Abel inversion.

Although many numerical methods have been developed to solve the Abel integral, in this study, eq. (2-35) is analytically solved. Because of the axisymmetry of flow properties, $\ln(I(y)/I_0)$ is fitted by an even polynomial function.

$$\ln\left(\frac{I}{I_0}(y)\right) = a_1y^2 + a_2y^4 + a_3y^6 + a_4y^8 + a_5y^{10} \dots \quad (2-35)$$

Here, a_i ($i=1, 2, 3, \dots$) are fitting parameters. In this case, eq. (2-34) is analytically solved. A typical result computed by Mathematica (Wolfram [118]) are tabulated in Table 2-5.

Table 2-5 Abel integral.

| Integrand | Result |
|---|---|
| $\int \frac{2y}{\sqrt{y^2 - r^2}} dy$ | $2\sqrt{y^2 - r^2}$ |
| $\int \frac{4y^3}{\sqrt{y^2 - r^2}} dy$ | $4\left(r^2\sqrt{y^2 - r^2} + \frac{1}{3}(y^2 - r^2)^{3/2}\right)$ |
| $\int \frac{6y^5}{\sqrt{y^2 - r^2}} dy$ | $6\sqrt{y^2 - r^2}\left(\frac{8}{15}r^4 + \frac{4}{15}r^2y^2 + \frac{1}{5}y^4\right)$ |
| $\int \frac{8y^7}{\sqrt{y^2 - r^2}} dy$ | $8\sqrt{y^2 - r^2}\left(\frac{16}{35}r^6 + \frac{8}{35}r^4y^2 + \frac{6}{35}r^2y^4 + \frac{1}{7}y^6\right)$ |
| $\int \frac{10y^9}{\sqrt{y^2 - r^2}} dy$ | $10\sqrt{y^2 - r^2}\left(\frac{128}{315}r^8 + \frac{64}{315}r^6y^2 + \frac{16}{105}r^4y^4 + \frac{8}{63}r^2y^6 + \frac{1}{9}y^8\right)$ |
| $\int \frac{12y^{11}}{\sqrt{y^2 - r^2}} dy$ | $12\sqrt{y^2 - r^2}\left(\frac{256}{693}r^{10} + \frac{128}{693}r^8y^2 + \frac{32}{231}r^6y^4 + \frac{80}{693}r^4y^6 + \frac{10}{99}r^2y^8 + \frac{1}{11}y^{10}\right)$ |

The measured absorption profiles as shown in Fig.4-5 at each radial position have to be transformed by the Abel inversion using the equation (2-4). Here, considering that the absorption coefficient changing with the laser frequency, the Abel inversion has to be conducted at each frequency. In this research, the measured absorption profiles were divided into 10 points at intervals of 0.5 GHz and the function of $-\ln(I/I_0)$ was fitted by 12th order polynomials as shown in Fig.2-12. Finally, the local absorption profiles were obtained after the Abel inversion as shown in Fig.2-13.

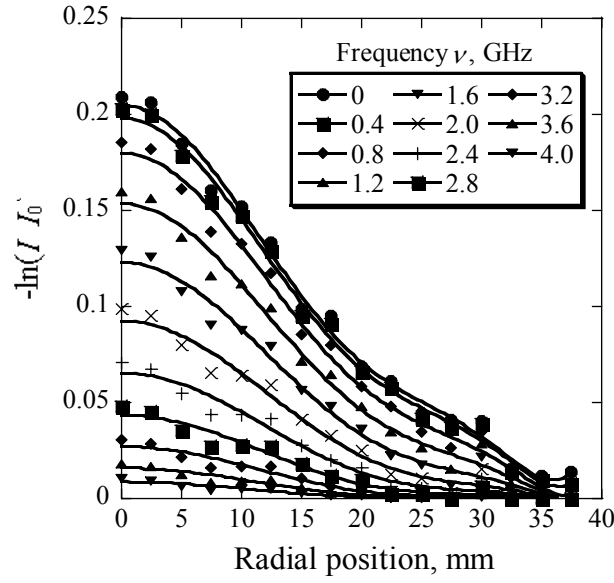


Fig. 2-12 Radial profiles of absorption fraction and 12th order polynomial fitting.

2.3.2 Gauss fitting

The obtained local absorption profiles after the Abel inversion were fitted by the Gaussian expressed as,

$$k_r(\nu) = k_r(\nu_0) \cdot \exp\left[-\left(\frac{\nu_0 - \nu}{\Delta\nu}\right)^2\right]. \quad (2-36)$$

The full width at half maximum $\Delta\nu_{\text{FWHM}}$ is related to $\Delta\nu$ by

$$\Delta\nu_{\text{FMWHM}} = 2\sqrt{\ln 2} \Delta\nu. \quad (2-37)$$

The integrated absorption coefficient is expressed as,

$$K(r) = \int_{-\infty}^{+\infty} k_r(\nu) d\nu$$

$$= k_r(\nu_0) \sqrt{\pi} \Delta \nu$$
(2-38)

Then, the local translational temperature and number density are obtained by the equations (2-14).

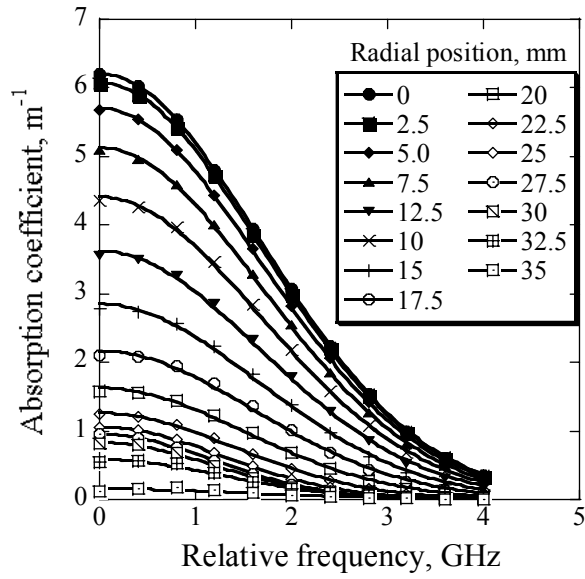


Fig. 2-13 Absorption coefficient and Gauss fitting after Abel inversion.

Chapter 3

Applicable Limit of Laser Absorption Spectroscopy

In this section, applicable limit of LAS and an effect of laser intensity on translational temperature measurements are investigated. Firstly, errors of absorption coefficients and temperature measurements are analytically discussed and applicable limit of LAS is represented. Secondary, an influence of laser intensity on Doppler broadening is investigated using glow and microwave discharge tube plasma and new broadening model is presented.

3.1 Error and Applicable Limit of LAS

3.1.1 Signal to noise ratio

Assuming the measurement noise is quantum and thermal one, the signal to noise ratio is expressed as,

$$\frac{P_s}{P_q + P_{th}} = \frac{\delta(e\eta/h\nu)^2 R}{(2e^2\eta P\Delta f/h\nu + 4eTNF\Delta f)} \quad (3-1)$$

Here, P_s , P_q , P_{th} , P are absorption power, shot noise, thermal noise and laser power, respectively. δ , is fractional absorption, η is the quantum efficiency of detector, R is resistance of terminator, Δf is band width of detection and NF is the noise figure. In the ideal case, noise is assumed to be only shot noise. The fractional absorption with signal to noise ratio of 1 is expressed as,

$$\begin{aligned} \delta_{\min} &= \frac{I - I_0}{I_0} = 2 \frac{h\nu\Delta f P}{\eta} \\ &\approx 10^{-8} (P = 10\text{mW}) \end{aligned} \quad (3-2)$$

In the practical experiments, it is reported that the fractional absorption of $10^{-1} \sim 10^{-2}$ % is achieved.

3.1.2 Error analysis and applicable limit of LAS

Error of absorption coefficient

From Beer-Lambert law Eqs. (2-1,2), error of absorption coefficient is related to that of fractional absorption expressed as,

$$\frac{\Delta k}{k} = \frac{\Delta(I/I_0)}{(I/I_0)\ln(I/I_0)}. \quad (3-3)$$

Here, Δk , $\Delta(I/I_0)$ are errors of absorption coefficient and measurement, respectively. Figure 3-1 shows the estimated error of absorption coefficient for various measurement errors. The error rapidly increases with lower $(I_0-I)/I_0 < 0.1$. At high $(I_0-I)/I_0 > 0.99$, the error also increases with $(I_0-I)/I_0$. However, for high number density states, corresponding errors may be reduced by targeting other degenerate states or higher excited states. Therefore, errors at higher $(I_0-I)/I_0$ are not discussed below. The fractional absorption more than 1% is measured within 1% error at $\Delta(I/I_0)$ of 10^{-2} %.

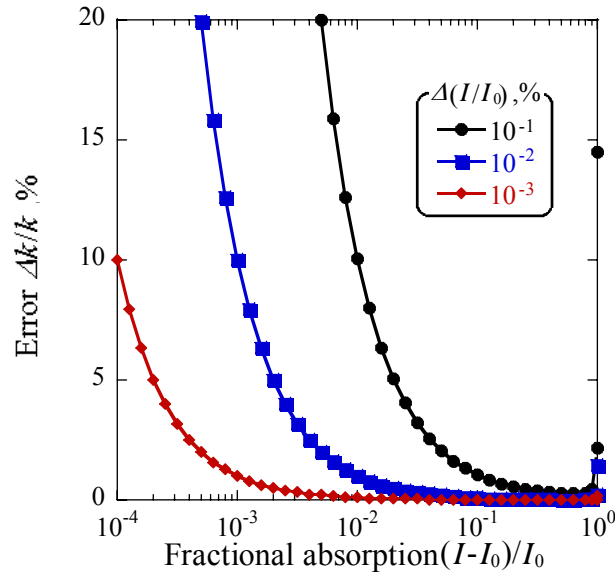


Fig. 3-1 Estimated error of absorption coefficient

Error of temperature

As shown in the Fig. 3-2, a relationship between errors of absorption coefficient and FWHM is expressed as,

$$\frac{\Delta(\Delta\nu_D)}{\Delta\nu_D} \approx \frac{\Delta k}{k}. \quad (3-3)$$

Since FWHM of absorption profiles is calibrated by etalon, its error should be added. Then, the error of width is rewritten as,

$$\frac{\Delta(\Delta\nu_D)}{\Delta\nu_D} \approx \frac{\Delta k}{k} + \frac{\Delta\text{FSR}}{\Delta\nu_D}. \quad (3-4)$$

Here, ΔFSR is the etalon error. Assuming the calibration error is 1 %, ΔFSR for FSR of 1GHz is 0.01 GHz.

As shown in Eq. (2-12), temperature is proportional to the square of FWHM. Then from Eqs. (3-3, 4) temperature error is expressed as,

$$\frac{\Delta T}{T} = 2 \frac{\Delta(\Delta\nu_D)}{\Delta\nu_D} \approx 2 \left(\frac{\Delta(I/I_0)}{(I/I_0)\ln(I/I_0)} + \Delta\text{FSR} \right). \quad (3-5)$$

Figure 3-3 shows temperature errors for $(I_0-I)/I_0 > 10^{-3}$ % and T of 500 K and 5000 K. Here, number density corresponding $(I_0-I)/I_0$ is roughly calculated in which absorption length is set to be 1 cm and λ , A and g in OI 777.19 nm line are used, respectively. With $\Delta(I/I_0)$ of 0.01%, translational temperature is measured with in 5 % error for $(I_0-I)/I_0 > 10^{-2}$. Then, in this case, measurable minimum number density is about 10^{15} m^{-3} .

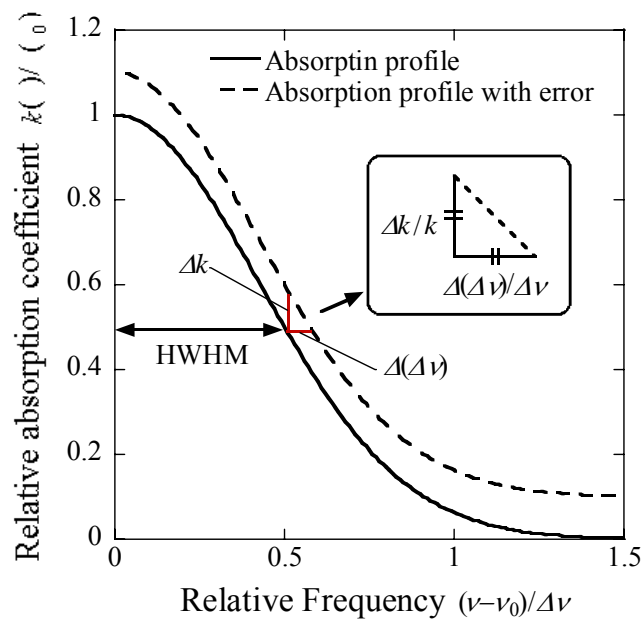


Fig. 3-2 Conceptual figure of a relationship between absorption coefficient error and FWHM one.

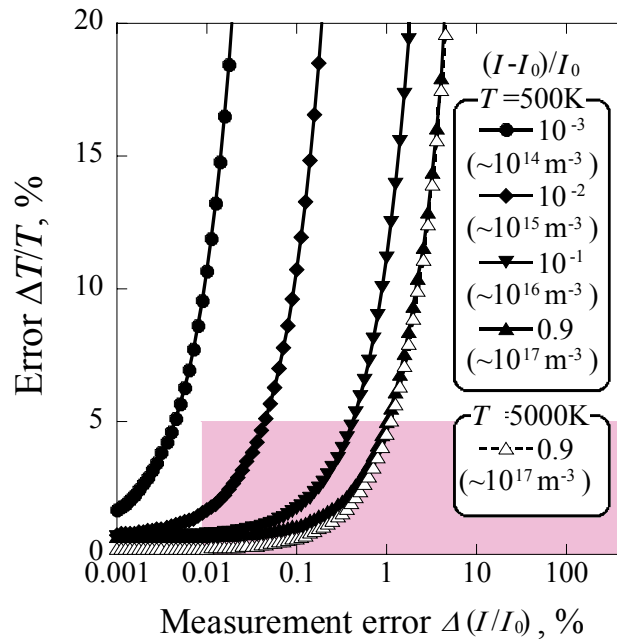


Fig. 3-3 Estimated error of temperature for various fractional absorption and corresponding number density (λ , A , g , are used in OI 777.19nm, absorption length is 1cm.)

3.2 Absorption Saturation

3.2.1 Background: Absorption saturation in LIF

In LIF, fluorescence signal is proportional to the number density excited by probe laser, expressed as [73],

$$N_2 = N_1 \frac{B_{12}}{B_{12} + B_{21}} \frac{1}{1 + I_{\text{sat}} / I} . \quad (3-6)$$

Here, B is the Einstein coefficient and I_{sat} is the saturation intensity defined as,

$$I_{\text{sat}} = \frac{A_{21} + Q_{21}}{B_{12} + B_{21}} c . \quad (3-7)$$

Here, Q is the quenching rate. Then, the fluorescence signal is classified into two regimes as shown in Fig. 3-4.

In case of $I \ll I_{\text{sat}}$, this is called linear regime, the fluorescence signal is proportional to the probe laser intensity expressed as,

$$N_2 = N_1 \frac{B_{12}}{B_{12} + B_{21}} \frac{I}{I_{\text{sat}}} . \quad (3-8)$$

Then, in this regime, the fluorescence signal is normalized by laser intensity and the quenching rate is necessary for the density measurements. Planar-LIF is usually conducted in this regime for the nonnecessity of high laser intensity.

In case of $I \gg I_{\text{sat}}$, this is called saturation regime, the signal is independent of the laser intensity expressed as,

$$N_2 = N_1 \frac{B_{12}}{B_{12} + B_{21}} . \quad (3-9)$$

In this case, rates of laser absorption and stimulated emission are enough large to neglect other transition processes. The fluorescence signal is maximized. Although the quenching rate is not necessary for density measurements, high laser intensity enough to saturate the absorbers is necessary.

As described above, in LIF laser intensity is carefully determined. On the analogy of LIF, it is thought that absorption saturation also influences on LAS. Therefore, in the following sections, influences of laser absorption on number density and translational temperature measurements by LAS are investigated.

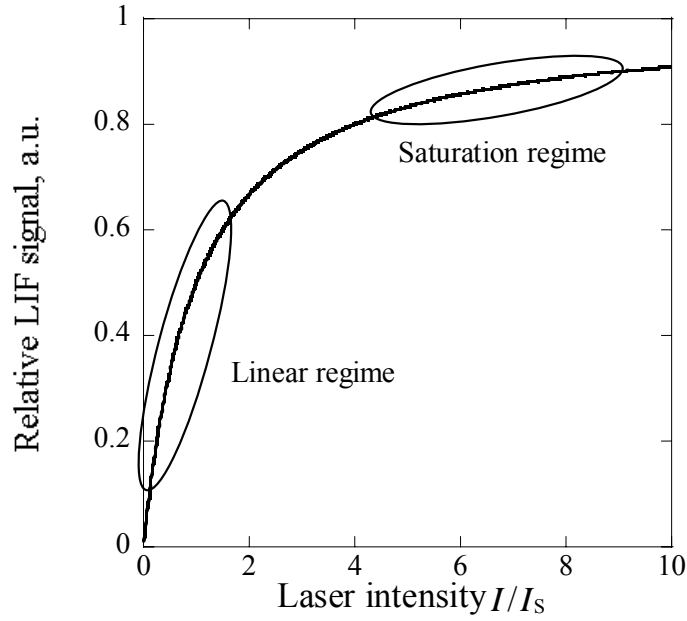


Fig. 3-4 Relationship between LIF signal and laser intensity

3.2.2 Theory of Absorption Saturation

Homogeneous broadening

According to the conventional theory, the saturated absorption coefficient $k_S(\nu)$ at laser intensity I is expressed as [120, 121],

$$k_S(\nu) = \frac{c^2 A_{ji}}{8\pi\nu^2} \left(\frac{g_j}{g_i} N_i^0 - N_j^0 \right) \frac{\Delta\nu_L/2\pi}{(\nu - \nu_0)^2 + (\Delta\nu_L/2)^2 \cdot \left(1 + \frac{\phi c^2}{2\pi^2 h \nu^3 \Delta\nu_L} I \right)} \quad (3-10)$$

$$= K_0 \cdot g_L(\nu) \left[1 + \frac{I}{I_{S_homo}(\nu)} \right]^{-1} \quad (3-11)$$

, where $g_L(\nu)$ is the Lorentzian line shape function defined as

$$g_L(\nu) = \frac{\Delta\nu_L/2\pi}{(\nu - \nu_0)^2 + (\Delta\nu_L/2)^2} \quad (3-12)$$

Here, ν , ν_0 , h , c and g represent laser frequency, absorption line frequency, Planck's constant, velocity of light and statistical weight, respectively. $\Delta\nu_L$, K_0 , and N_0 are the FWHM of homogeneous broadening, integrated absorption coefficient and population density in the absence of light,

respectively and $\phi = A_{ji} / (A_{ji} + Q_{ji})$ where A , Q , i , and j are the Einstein coefficient, quenching rate, absorption level and excited level, respectively. The saturation laser intensity for homogeneous broadening $I_{S_homo}(\nu)$ is defined as

$$I_{S_homo}(\nu) = \frac{4\pi h \nu^3}{\phi c^2} \frac{1}{g_L(\nu)}. \quad (3-13)$$

Equation (3-10) indicates that the saturated line profile remains Lorentzian, whereas its linewidth $\Delta \nu_{SL}$ increases with I as

$$\Delta \nu_{SL} = \Delta \nu_L \sqrt{1 + \frac{\phi c^2}{2\pi^2 h \nu^2 \Delta \nu_L} I}. \quad (3-14)$$

Inhomogeneous broadening

In the case of inhomogeneous broadening, absorption saturation is somewhat complex because individual absorption particles are distinguishable. The lineshape is inhomogeneous in which each distinguishable part is homogeneous as shown in Fig. 3-5. The resulting profile is a convolution integral of the Gaussian and the saturated Lorentzian profiles expressed as

$$k_S(\nu) = \frac{A_{ji} c^2 \Delta \nu_L}{16\pi^2 \nu^2} \left(\frac{g_j}{g_i} N_i^0 - N_j^0 \right) \int_{-\infty}^{\infty} \frac{\exp[-\{2(\nu_\xi - \nu_0) / \Delta \nu_D\}^2 \ln 2] d\nu_\xi}{(\nu - \nu_\xi)^2 + (\Delta \nu_{SL} / 2)^2}. \quad (3-15)$$

Here, x represents respective distinguishable part.

In low-pressure plasma where Doppler broadening is dominant (Voigt parameter $\alpha = (\ln 2)^{1/2} \Delta \nu_L / \Delta \nu_D \ll 1$), the exponential part in Eq. (3-15) is approximately pulled outside the integrand. The integral is calculated as

$$k_S(\nu) = K_0 \cdot g_G(\nu) \left[1 + \frac{I}{I_{S_inhomo}} \right]^{-1/2}. \quad (3-16)$$

Here, $g_G(\nu)$ is the Gaussian lineshape function

$$g_G(\nu) = \frac{2}{\Delta \nu_D} \sqrt{\frac{\ln 2}{\pi}} \exp \left[-\ln 2 \left\{ \frac{2(\nu - \nu_0)}{\Delta \nu_D} \right\}^2 \right]. \quad (3-17)$$

and the saturation intensity for inhomogeneous broadening I_{S_inhomo} is defined as

$$I_{S_inhomo} = \frac{2\pi^2 h \nu^3 \Delta \nu_L}{\phi c^2}. \quad (3-18)$$

When pressure broadening is the most dominant in homogeneous broadening, Eq.(3-18) is rewritten as,

$$I_{S_inhomo} = \frac{2\pi^2 h \nu^3 N \bar{v} \sigma}{\phi c^2}. \quad (3-19)$$

Here, N and σ represent the number density of colliding particle and collision cross-section, respectively. \bar{v} is the averaged velocity of absorbers defined as

$$\bar{v} = \sqrt{3k_B T / m}. \quad (3-20)$$

If variation of I_{S_inhomo} is very small in the range of $|\nu - \nu_0| < \Delta \nu_D$, Doppler width of the saturated profile $\Delta \nu_{SD}$ is invariant for the variation of laser intensity:

$$\Delta \nu_{SD} = \Delta \nu_D. \quad (3-21)$$

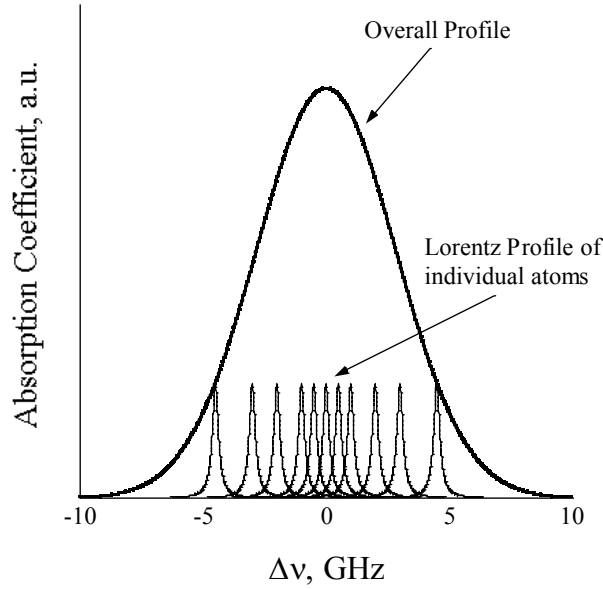


Fig. 3-5 Convolution of homogeneous and inhomogeneous profiles

3.2.3 Experimental Apparatus

In this study, the influence of laser intensity on broadenings was measured in two types of argon plasma. One is glow discharge tube plasma (CI TECHNO CO., Ltd) as shown in Fig.3-6. Its input power, discharge voltage and ambient pressure were 1.5 W, 4.00 V, and 79 Pa, respectively. This is direct current plasma and the gas is static.

The other is TE₁₀ mode microwave discharge tube plasma (NIHON KOSHUHA CO., Ltd) as shown in Figs. 3-7, 8. Its input power, oscillation frequency, mass flow rate and ambient pressure are 500 W, 2.4 GHz, 20 sccm and 20 Pa, respectively.

In addition to the basic set up described in Chapter 2, neutral density filters and lenses are used to vary laser intensity. At the measurement points, the laser intensity is ranged from 0.60 mW/mm² to 2.4.4 mW/mm². Target absorption lines are 840.82 nm, 842.46 nm, and 852.14 nm of ArI.

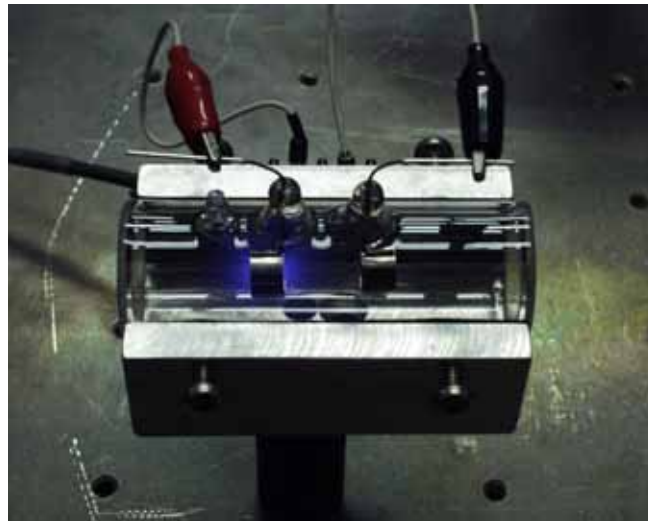


Fig. 3-6 Photo of glow discharge tube plasma

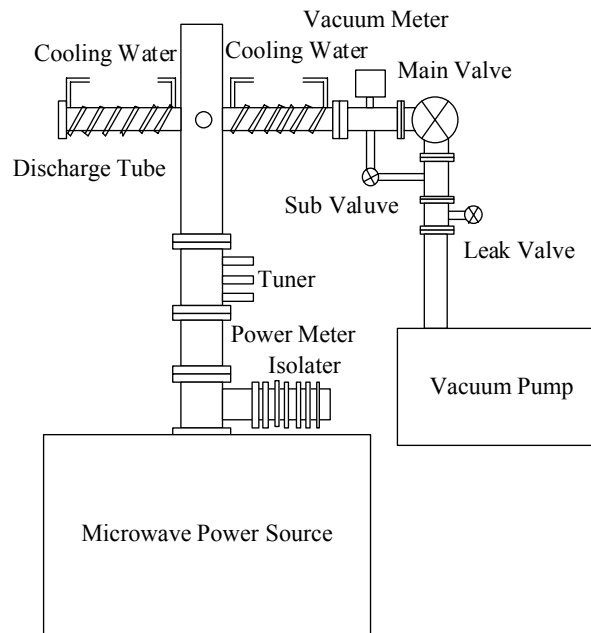


Fig. 3-7. Schematic of TE₁₀ mode microwave discharge tube



Fig. 3-8 Photo of microwave discharge tube plasma

3.2.4 Experimental results

Figure 3-9 shows the measured absorption profiles at 842.46 nm line in the glow discharge plasma. Strong absorption saturation was observed at high laser intensity. Absorption saturation was also observed for other lines and in the microwave discharge plasma. The Voigt parameter α of the measured profiles was kept less than 0.07 and then Doppler dominant approximation was valid for all conditions.

Figure 3-10 shows a plot of absorption coefficient and a theoretical curve-fitting of Eq.(3-16) as a function of I/I_{S_inhomo} , where I_{S_inhomo} was a fitting parameter. Figure 3-11 shows plots of $\Delta\nu_{SD}$ and T . $\Delta\nu_{SD}$ increased with I in contradiction to the theoretical prediction Eq. (3-21), resulting in the increase in T with I .

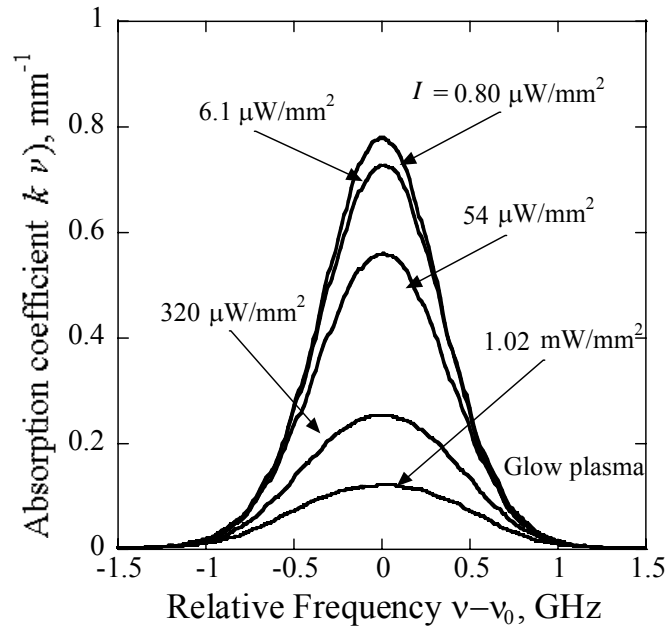


Fig. 3-9 Variation of absorption profiles in the glow discharge argon plasma. $\nu_0 = 842.46$ nm.

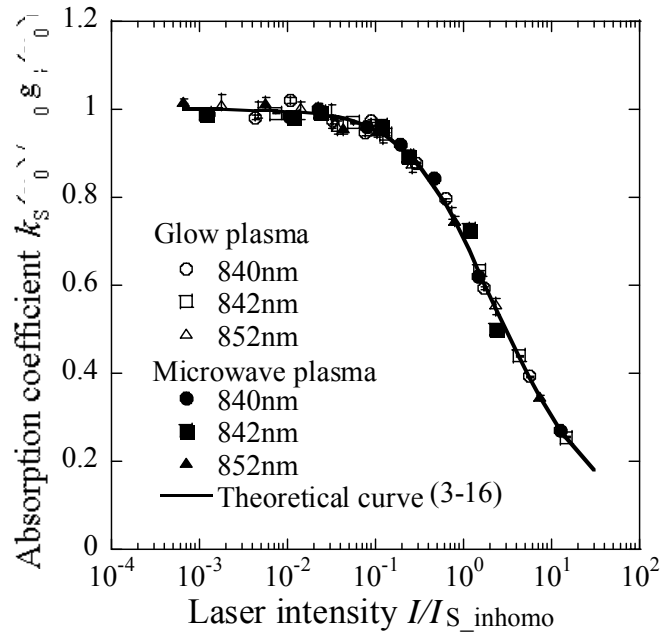


Fig. 3-10 Relationship between absorption coefficient and laser intensity.

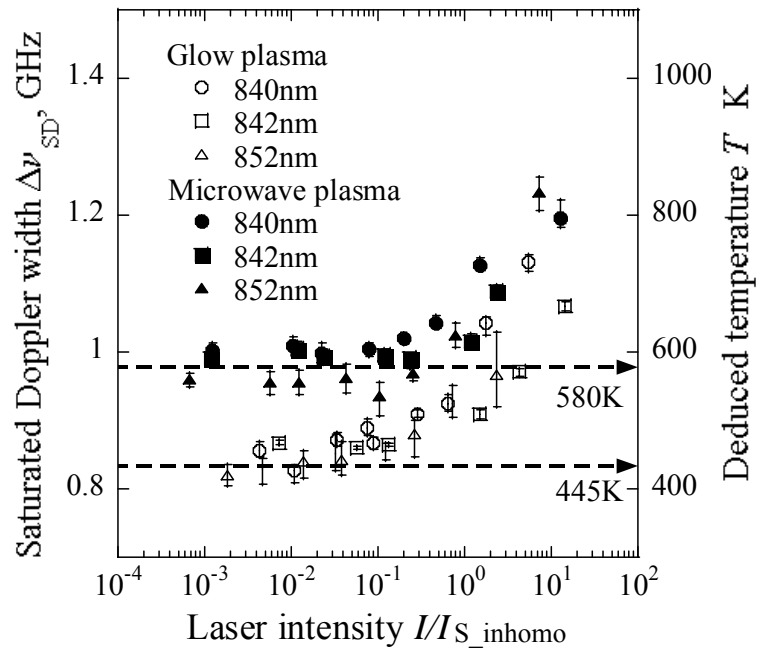


Fig. 3-11 Saturated Doppler width and deduced temperature.

3.2.5 Discussion

Dependency of I_{S_inhomo} on the frequency

The experimental result suggests that I_{S_inhomo} should vary with the relative frequency $|\nu - \nu_0|$. The averaged velocity v seen in Eq. (3-20) may be a function of $|\nu - \nu_0|$. In fact, absorbers showing larger Doppler shift have higher averaged velocity: In the gas isotropic in a three-dimensional velocity field, velocity $v(\nu)$ averaged over the absorbers showing the Doppler shift $|\nu - \nu_0|$ is expressed as

$$v(\nu) = \sqrt{(\nu - \nu_0)^2 \frac{c^2}{\nu_0^2} + \frac{2k_B T_0}{m}} = \bar{v} \sqrt{\frac{8 \ln 2}{3} \frac{(\nu - \nu_0)^2}{\Delta \nu_D^2} + \frac{2}{3}}. \quad (3-22)$$

Here, T_0 is the true temperature and \bar{v} is constant. Assuming s is constant, I_{S_inhomo} is expressed as a function of ν by substituting Eq.(3-22.) into Eq. (3-19),

$$I_{S_inhomo}(\nu) = I_{S_inhomo} \sqrt{\frac{8 \ln 2}{3} \frac{(\nu - \nu_0)^2}{\Delta \nu_D^2} + \frac{2}{3}}. \quad (3-23)$$

Figure 3-12 shows the theoretical plot of $I_{S_inhomo}(\nu)/I_{S_inhomo}(\nu_0)$. $I_{S_inhomo}(\nu_0/\Delta \nu_D)$ is almost double of $I_{S_inhomo}(\nu_0)$.

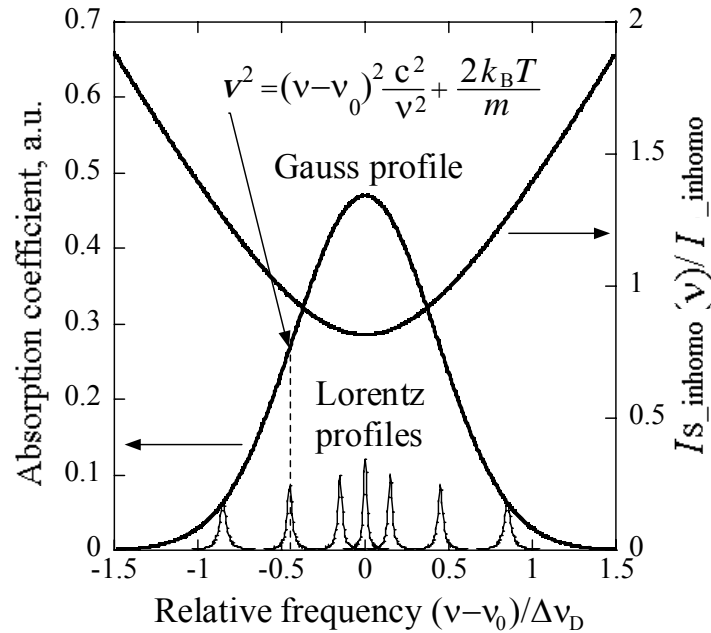


Fig.3-12 $I_{S_inhomo}(\nu)/I_{S_inhomo}$ and absorption profile.

Computed profile and true temperature

Figures 3-13, 14 show computed absorption profiles and a plot of relationship between computed absorption coefficient and laser intensity normalized by saturation one with theoretical curve fitting of Eq. (3-16). Strong saturation effects are also observed in the computed absorption profiles and their coefficients are well fitted on the curve.

Figure 3-15 shows the FWHM of absorption profiles measured and computed from Eqs. (3-16) and (3-23). The results show a good agreement.

The ratio of deduced temperature to the true temperature is computed for various laser intensities and Voigt parameters as tabulated in Table 1. When probe laser intensity is high ($I/I_{S_inhomo} > 10^{-1}$), temperature will be overestimated and should be corrected by the factor shown in Table 3-1.

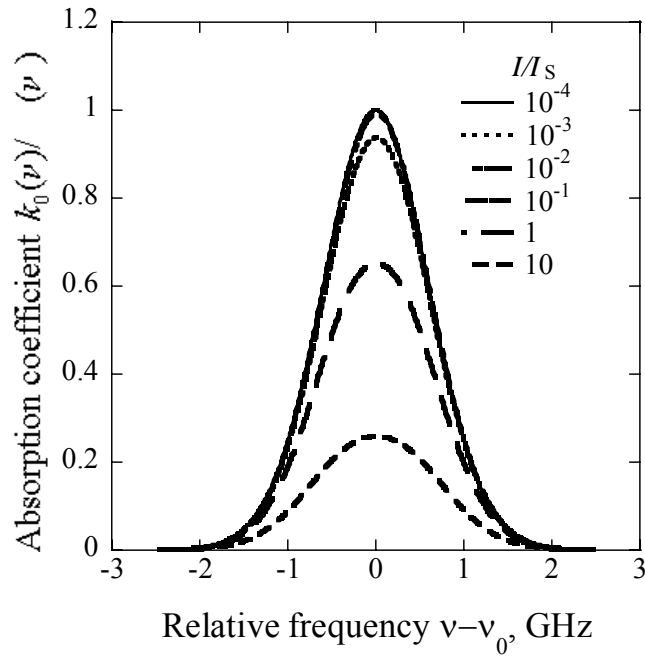


Fig. 3-13 Computed variation of absorption profiles.

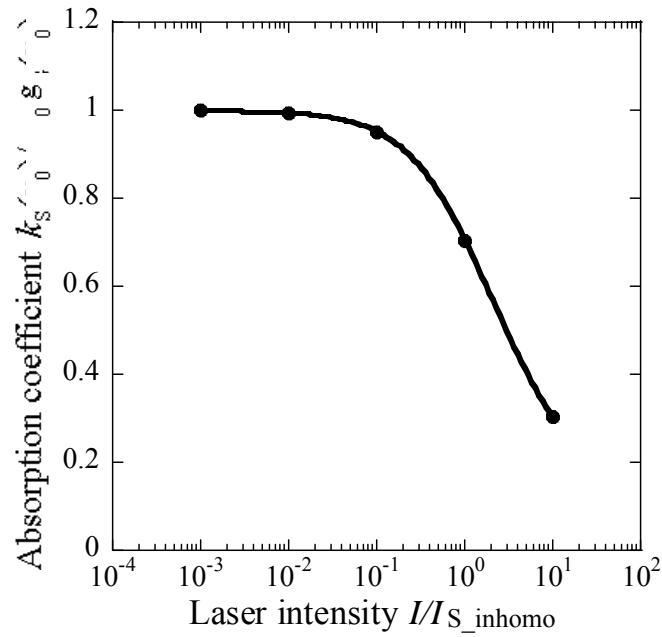


Fig. 3-14 Relationship between computed absorption coefficient and laser intensity.

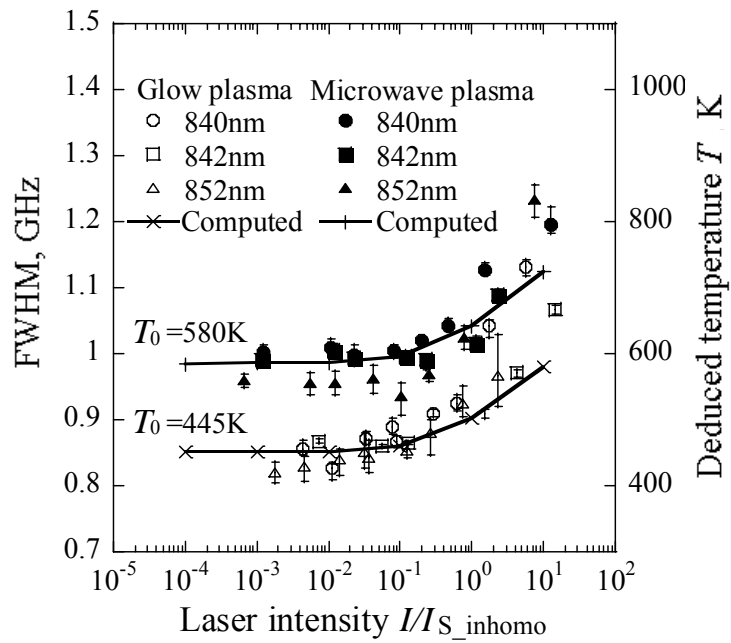


Fig. 3-15 Measured and computed FWHM.

Table 3-1 Ratio of deduced temperature to true one T/T_0

| $\alpha(w)$ | $I/I_{s \text{ inhom}}$ | | | | | |
|-------------|-------------------------|-----------|-----------|-----------|----------|-----------|
| | 10^{-4} | 10^{-4} | 10^{-2} | 10^{-1} | 1 | 10 |
| 0.01 | 0.999 | 0.999 | 1.004 | 1.018 | 1.107 | 1.216 |
| 0.05 | 1.014 | 1.014 | 1.014 | 1.044 | 1.148 | 1.441 |
| 0.1 | 1.047 | 1.047 | 1.047 | 1.057 | 1.189 | 1.585 |

3.3 Summary

Error and applicable limit of LAS are investigated. The fractional absorption more than 1% is measured within 1% error with measurement error of 10^{-2} %. An influence of this error on translational temperature measurements is also estimated. As a result, translational temperature is measured with in 5 % error for fractional absorption more than 10^{-2} with measurement error of 10^{-2} %. Then, in OI 777.19 nm measurements, the number density at least more than 10^{15} m^{-3} is necessary for temperature measurements within 5% error.

When probe laser intensity I is higher, Doppler broadening of absorption line becomes wider, and the temperature deduced from the broadening was found to tend to be overestimated in contradiction to the conventional laser theory.

This result is caused by the dependency of saturation intensity I_{S_inhomo} on the frequency: Absorbers showing larger Doppler shift $|\nu - \nu_0|$ have higher averaged velocity, and then increases with relative frequency $|\nu - \nu_0|$.

Even though probe laser intensity is high and saturation effect is large, true temperature can be obtained using a correction factor presented in this study.

Chapter 4

Application to Constricted Arc Wind Tunnels Flows

4.1 Facilities

4.1.1 JUTEM 20-kW Erosion Testing Machine

The Japan Ultra-high Temperature Materials Research Center (JUTEM) is located in Tajimi, Gifu prefecture [123]. The vacuum facility is consisted of a cylindrical steel vacuum chamber of approximately 1m diameter and 1m in length. Backpressure was maintained about 37 Pa (0.28 torr) during thruster operation with 20 slm argon and 4. slm oxygen by a rotary pump (KS-14.0, Sato-shinnkuu) and a mechanical pump (PMB-060B, ULVAC) whose pumping speed are 1,500 l/m and 100,000 l/m, respectively. The arc-heater is fixed at the center of the chamber flange. TPS materials can be mounted on a one-dimensional traverse stage at 100mm ~ 300mm from the nozzle exit to regulate the heat flux. On the both sides of the chamber, two 300mm diameter quartz windows are used for optical access to the arc-heater plume. The schematic of the vacuum system and its photograph are shown in Figs 4-1 and 2.

The arc-heater is a 20-kW class water-cooled type and built by the Ishikawajima-harima Heavy Industry (IHI). A schematic of the arc-heater is shown in Fig.4-3, and the zoom up of the constrictor part is shown in Fig.4-4 Oxygen is injected at the constrictor as described in Chapter 2. The cathode is made of 2% thoriated-tungsten alloy and nozzle is of copper, both of which are cooled by water. The converging and diverging sections are both conical, with half-angle of 45 and 15 degrees, respectively. The constrictor is 8mm in diameter and 16mm in length. The diverging section is 156.8mm in length and has an area ratio of 156:1, yielding an exit diameter of 100mm. The flow Mach number is designed at 3. Nitrogen-oxygen gas or argon-oxygen gas were used as a working gas. The input power is 20 kW for the nitrogen-oxygen gas and 7.2 kW for the argon-oxygen gas. Total pressure is about 1 kPa for the nitrogen 20slm and oxygen 5 slm flow.

4.1.2 The University of Tokyo 1.2-kW Arc-Heater

Most of the experiments described in this thesis were performed in the university of Tokyo with a 1.2-kW arc-heater. The vacuum facility is consisted of a cylindrical steel vacuum chamber of 0.5 m in diameter and 2 m in length with a rotary pump (VS14.01, ULVAC) and a mechanical pump (PMB-012CM, ULVAC) whose pumping speed are 2500 l/m and 17,000 l/m, respectively. The chamber pressure can be maintained to be at 0.2torr with 6slm of argon and 1.4slm oxygen flow. The arc-heater is set on the center of the chamber and its plume direction is parallel to the chamber axis. On the both sides of the chamber, two 100 mm diameter quartz windows are used for optical access to the arc-heater plume. An optical fiber and BNC cables are lead in the chamber window through the flange connector to set a part of the optical system in the chamber.

The arc-heater is a 1.2-kW class water-cooled type and built in the university of Tokyo. The schematic of the arc-heater is shown in Fig.4-5 and its photograph is shown in Fig.4-6. The zoom up of the constrictor part and the schematic of the injecting part and its photograph are shown in Figs.4-7, 8 and 9. The cathode is made of 2% thoriated-tungsten alloy and nozzle is of copper, both of which are cooled by water. The converging part is made of boron, where oxygen is injected. This section and the diverging section are both conical, with half-angle 30 and 15. degrees, respectively. The constrictor is 2mm in diameter and 3mm in length. The diverging section 4.2.3mm in length and has an area ratio of 225:1, yielding an exit diameter of 30mm. The flow Mach number is designed at 2. The distribution of the flow velocity deduced from the Doppler shift of the center absorption wavelength is shown in Fig.4-14. Argon-oxygen gas was used as a working gas and supplied by a mass flow controller (3620, KFLOC). The maximum input power is 1.2 kW and supplied by a power source (NH-120100, Stabilizer). The plenum pressure dependence on the mass flow rate is shown in Fig.4-10 and on the input power is shown in Fig. 4.-11. The thermal efficiency was estimated about 60% from the increase in temperature of cooling water.

Table 4-1 Comparison of two vacuum facilities and arc-heaters.

| | JUTEM Arc-heater | The university of Tokyo Arc-heater |
|-----------------------|-------------------------------------|---|
| Vacuum Facility: | | |
| Chamber diameter | 1 m | 0.5 m |
| Chamber length | 1 m | 2 m |
| Pumping speed | 1500 l/m (100,000l/m) | 2500 l/m (17,000 l/m) |
| Back pressure | 38 Pa | 26 Pa |
| | (Ar: 20slm, O ₂ : 5 slm) | (Ar: 4.slm, O ₂ : 1.5 slm) |
| Arc-heater: | | |
| Constrictor diameter | 8 mm | 2 mm |
| Constrictor length | 16 mm | 3 mm |
| Area ratio | 14.6 | 225 |
| Converging half angle | 45° | 30° |
| Diverging half angle | 15° | 15° |
| Exit diameter | 100 mm | 30 mm |

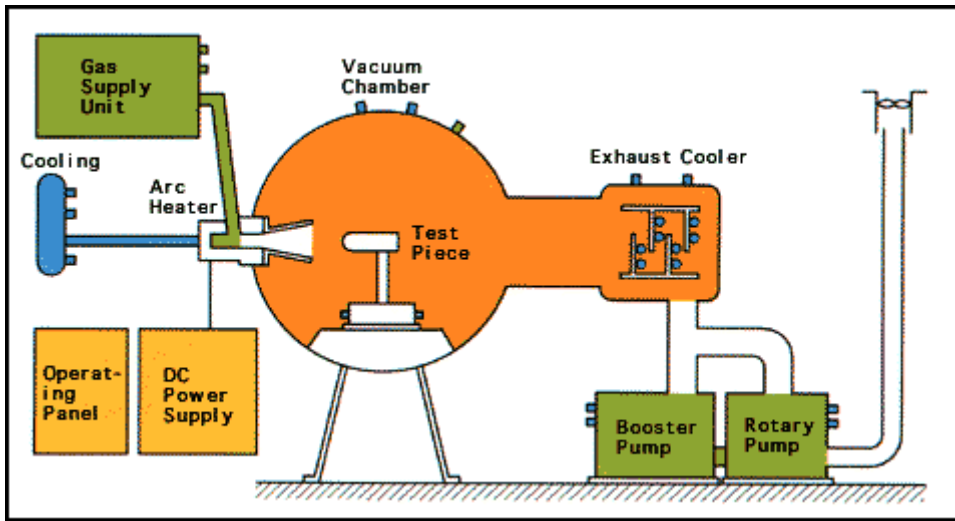


Fig.4-1 Schematic of arc-JUTEM heater system.



Fig.4-2 Photograph of JUTEM arc-heater.

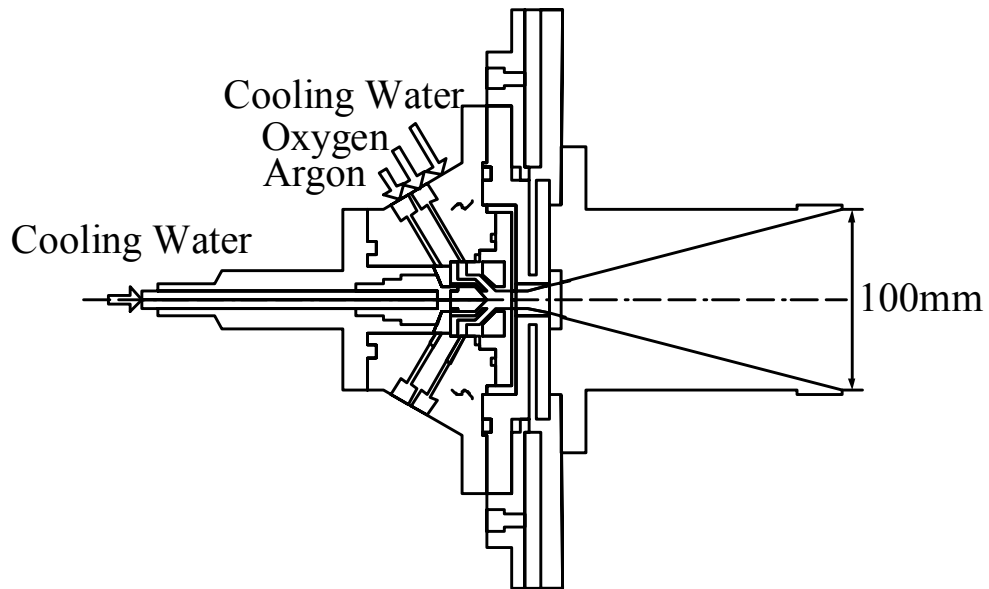


Fig.4-3 Schematic of JUTEM arc-heater.

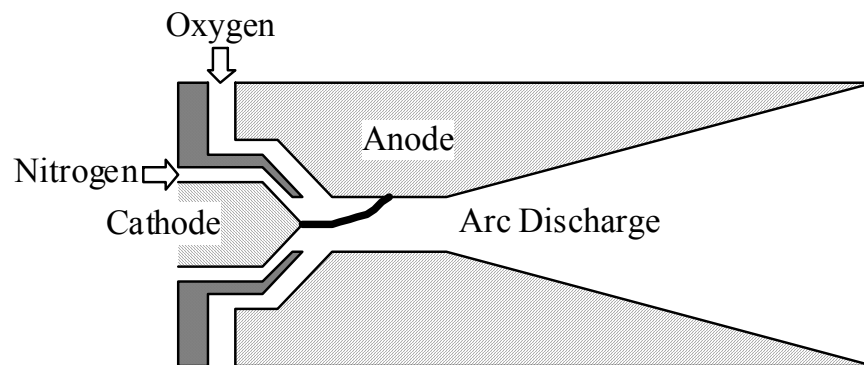


Fig.4-4 Schematic of constrictor part of JUTEM arc-heater.

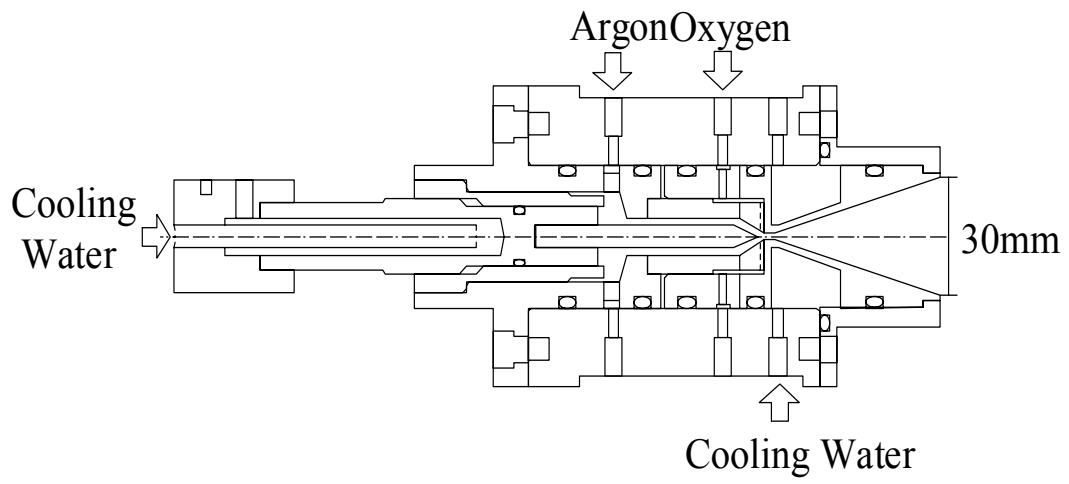


Fig.4-5 Schematic of University of Tokyo arc-heater.

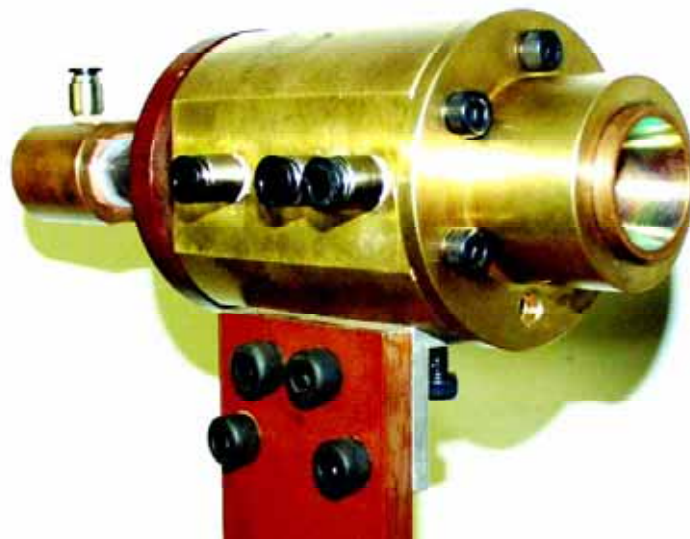


Fig.4-6 Photograph of University of Tokyo arc-heater.

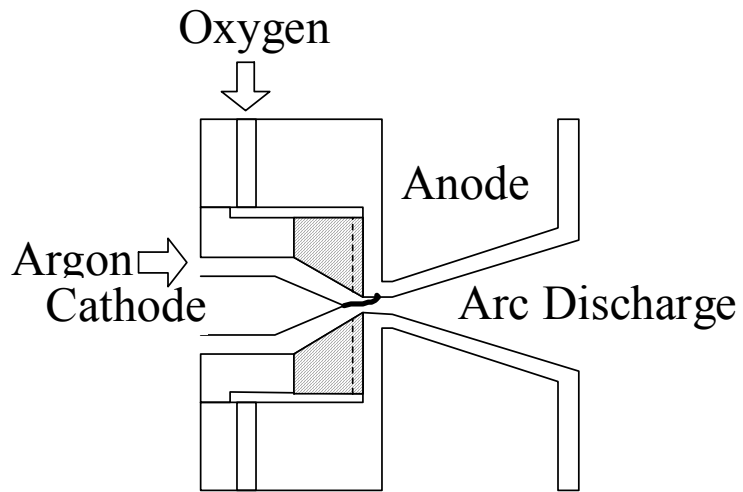


Fig.4-7 Schematic of constrictor part of University of Tokyo arc-heater.

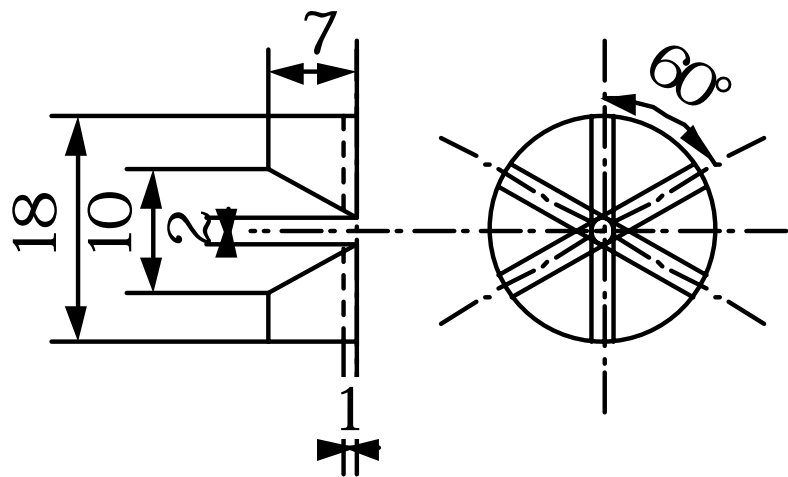


Fig.4-8 Schematic of injection part of University of Tokyo arc-heater.

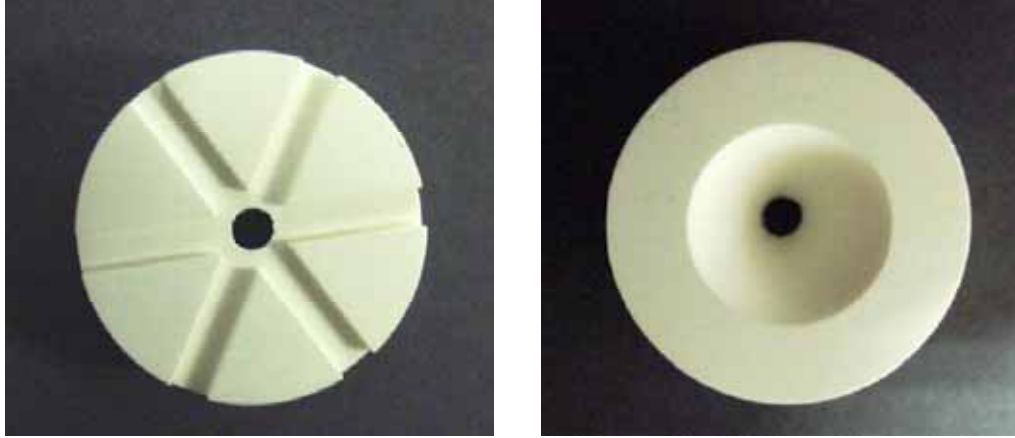


Fig.4-9 Photograph of injection part of University of Tokyo arc-heater.

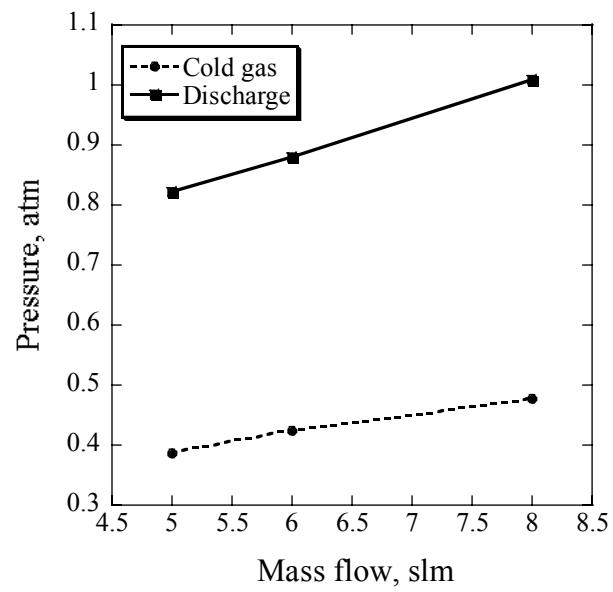


Fig.4-10 Pressure dependency on mass flow rate.

4.2 Test Conditions

4.2.1 Velocity Measurement

Flow velocity of the university of Tokyo arc-heater plume was measured from the Doppler shift. The target line was the absorption from the metastable argon. As a reference signal at rest, the radiation tube whose power was 0.5 mW was used. Table 4-3 shows the experimental conditions.

Table 4-2 Experimental conditions for velocity measurement.

| Radiation tube | Gas Flow | Specific Enthalpy | Target | Arc Generator |
|----------------|--------------------------|-------------------|---------------------|-----------------------------------|
| 0.5 mW | Ar: 6 slm | 3.3 MJ/kg | Ar I (840.82 nm) | University of Tokyo arc-heater |
| | O ₂ : 1.5 slm | | | |

4.2.2 Number Density and Translational Temperature Measurement

Three cases were tested, and the experimental conditions are listed in Table 4-4. Case #1 is the measurement of the number density of metastable atomic oxygen and the translational temperature using the OI 777.19nm absorption line in the argon-oxygen plume generated in the JUTEM arc-heater. The flow consists of 20 slm argon and 4. slm oxygen. The input power is 7.2 kW and specific enthalpy is about 6.1 MJ/kg assuming that thermal efficiency is 60%. The backpressure was kept at 38 Pa.

Case #2 is the measurement using the University of Tokyo arc-heater. The target line is also OI 777.19nm. The flow consists of 6 slm argon and 1.4. slm oxygen. The input power is 1.2 kW and specific enthalpy is 3.3 MJ/kg. The backpressure was kept at 26 Pa.

Case #3 is the measurement of the number density of metastable argon and the translational temperature using the ArI 840.82nm absorption line. The operating conditions are the same as those in Case #2.

Table 4-3 Experimental conditions for laser absorption spectroscopy.

| No | Gas Flow | Specific Enthalpy | Target | Arc Generator |
|----|--------------------------|-------------------|----------------------|---------------------------------------|
| 1 | Ar: 20slm | 6.1 MJ/kg | O I (777.19nm) | JUTEM Erosion Testing Mashine |
| | O ₂ : 4.slm | | | |
| 2 | Ar: 6slm | 3.3 MJ/kg | O I (777.19nm) | The University of Tokyo arc-heater |
| | O ₂ : 1.4.slm | | | |
| 3 | Ar: 6slm | 3.3 MJ/kg | Ar I (84..0.82nm) | The University of Tokyo arc-heater |
| | O ₂ : 1.4.slm | | | |

Photographs of the JUTEM arc-heater plume and the university of Tokyo arc-heater plume are shown in Figs.4-11 and 12, in which the measured planes are drawn in broken lines. Typical signals, absorption, reference and ethalon, and a normalized absorption profile of metastable oxygen are shown in Figs. 4-13 and 14.

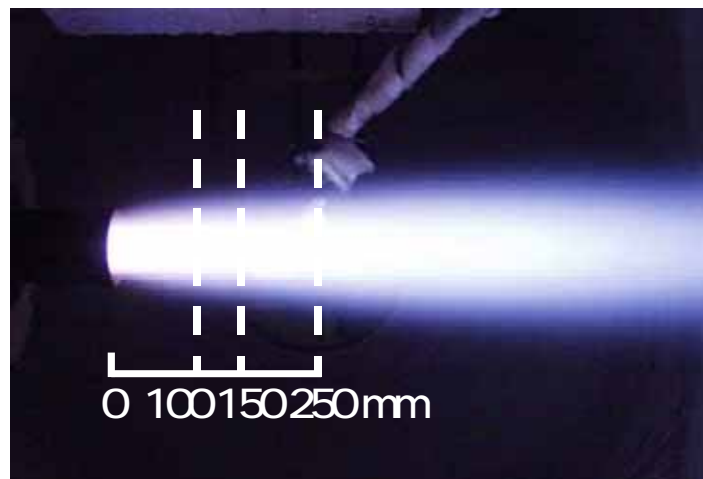


Fig. 4-11 JUTEM Erosion Testing Machine plume and measurement plane.

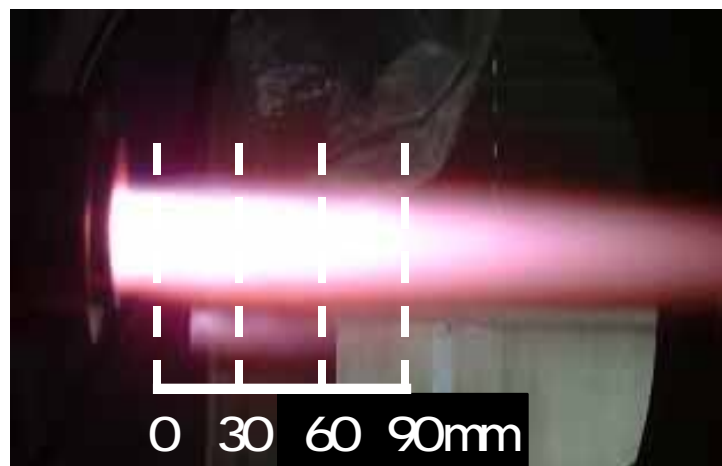


Fig. 4-12 University of Tokyo arc-heater plume and measurement plane.

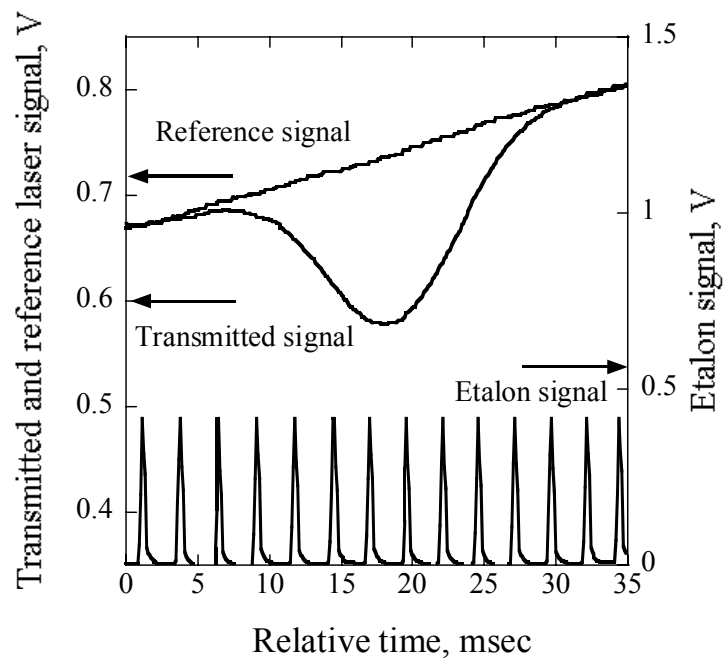


Fig. 4-13 Typical signals.

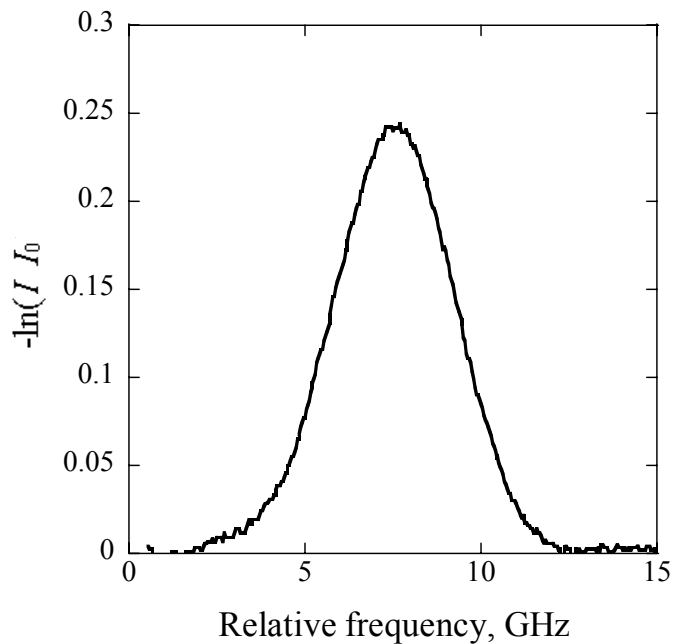


Fig. 4-14 Normalized absorption signals.

4.3 Measured Results

4.3.1 Flow Velocity

Figure 4-15 shows the absorption profiles in the arc-heater plume and the radiation tube. From the Doppler shift describe in the previous Chapter, the flow velocity is estimated to be 1630[m/s].

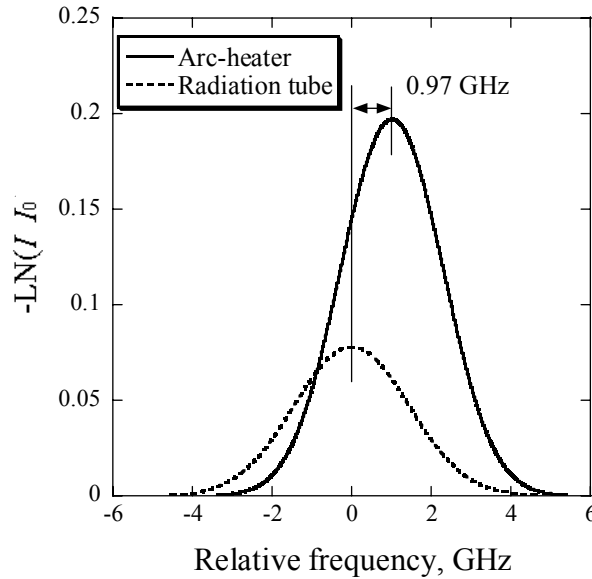


Fig. 4-15 Absorption profiles in arc-heater plume and radiation tube.

4.3.2 Number Density Distributions

Case #1

Figure 4-16 shows the distributions of meta-stable oxygen number. At $z=100\text{mm}$, the number density profile has two peaks at $r=20\text{mm}$ (here, z and r are defined by cylindrical coordinate and origin is taken at the center of nozzle exit). Then, these two peaks approach to the centerline in the downstream of the plume and combine at $z=24.0\text{mm}$. The maximum number density is $3.1 \times 10^{16}\text{m}^{-3}$.

Case #2

Figure 4-17 shows the distributions of meta-stable oxygen number. The profile of number density distribution is similar to that of Case #1. That is, at $z=0\text{mm}$, the number density profile has a peak at $r=11\text{mm}$. Then, the peak approach to the centerline in the downstream of the plume and combine at $z=60\text{mm}$. The maximum number density is $3.5 \times 10^{16}\text{m}^{-3}$.

Case #3

Figure 4-18 shows the distributions of meta-stable argon number. Number density decreases monotonously along the centerline. The maximum number density is $3.0 \times 10^{17}\text{m}^{-3}$.

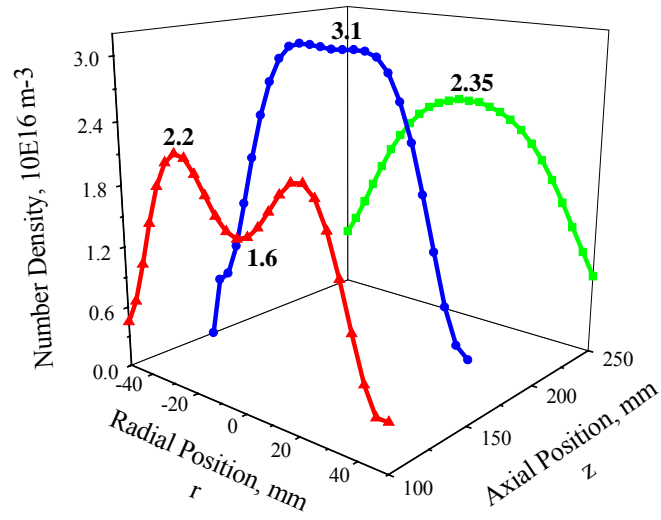


Fig. 4-16 Number density distributions of atomic meta-stable oxygen in JUTEM Erosion Testing Machine.

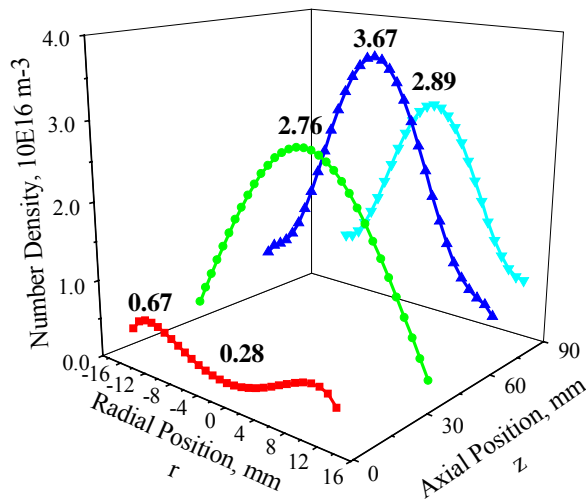


Fig. 4-17 Number density distributions of atomic meta-stable oxygen in University of Tokyo arc-heater plumes.

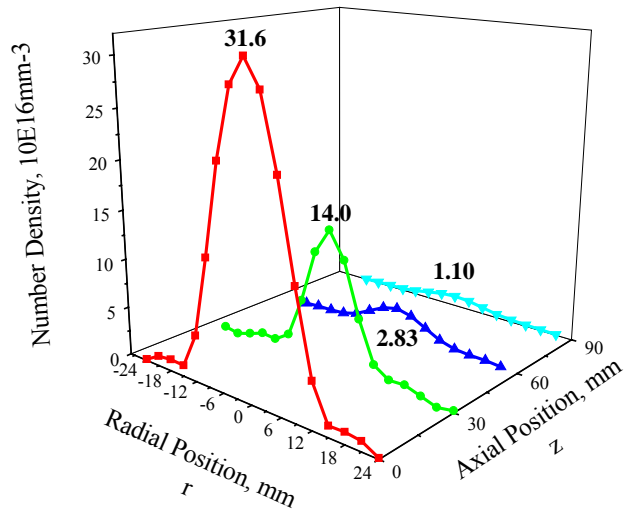


Fig. 4-18 Number density distributions of atomic meta-stable argon in the University of Tokyo arc-heater plumes.

4.4 Discussion

4.4.1 Flow Velocity

Assuming the fluid is ideal, the velocity of sonic a is expressed as,

$$a = \sqrt{\gamma RT} \quad (4-1)$$

Here, γ is the ratio of specific heats and R is the gas constant. For the argon gas, $a=986$ m/s. So, the flow Mach number is estimated to be 1.65. Considering that the measurement point is 30 mm from nozzle exit and the plume is not ideal gas, this value is thought to be valid.

4.4.2 Density distributions

The density peaks of meta-stable atomic oxygen were located off-axis at the nozzle exit and approached to the centerline in Cases #1 and #2 as shown in Figs 4-16 and 17. Although the profile of ground state would be somehow different from that of meta-stable state, this result implies the following mixing process. Oxygen injected at the constrictor is not enough mixed with nitrogen in the nozzle. Then, oxygen diffuses from outside toward the centerline, being dissociated in the plume out of the nozzle. Since, oxygen does not pass through the high temperature cathode-jet region, degree of dissociation is unexpectedly small. The visualized schematic of mixing process is shown in Fig. 4-19.

In Case #2, two density peaks located off-axis combine earlier than in Case #1. This is partly because the size of the University of Tokyo's arc-heater is smaller than JUTEM's and the shear in the free jet is stronger resulting in larger turbulent transport, and partly because the flow Mach number of former plume is smaller than the latter one.

In the downstream, number density of meta-stable atomic oxygen is increasing, while that of meta-stable argon is decreasing as shown in Figs. 4-17 and 18. This is because oxygen is being dissociated in the plume, while meta-stable argon is being deexcited by collision and radiation.

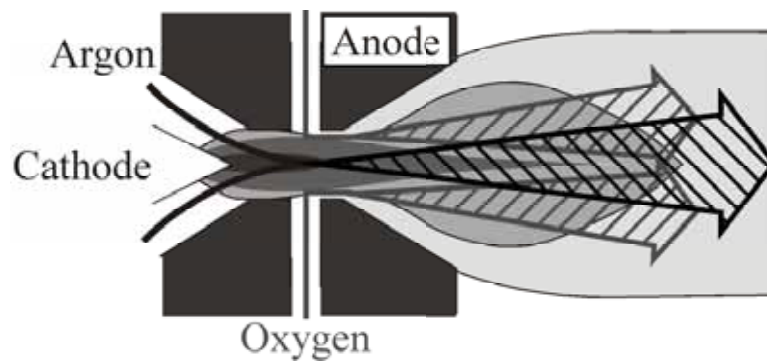


Fig. 4-19 Mixing process.

4.5 Comparison with CFD results

It is difficult for the OI number density at the ground state to be estimated from that at the absorbing state because the energy level of the absorbing state is far above that of the ground state. Therefore, total OI number density and its distribution were simulated by CFD analysis in the constrictor, nozzle and the plume. This work is conducted by Koreto [124].

4.5.1 Numerical models

Arc discharge process has not been solved for simplicity because this simulation focuses on the diffusion and mixing processes of the oxygen injected into the inert gas flow at the constrictor part. The temperature distribution of argon inlet flow was given as a boundary condition assuming thermo-chemical equilibrium because the flow speed is subsonic and pressure is high around the cathode tip.

Seven species and seven chemical reactions are taken into account as listed in Table 4-4. Arrhenius type forward reaction rates were used and the principle of the detailed balance was used to have backward reaction rates [125]. One temperature model is employed. Transport coefficients such as viscosity, thermal conductivity and diffusion coefficient were calculated by the formulas in reference [126]. The algebraic turbulence model by the Plandtl's mixing length theory was used [127]. The Reynolds number in the free-jet region was 1800.

Table 4-4 Chemical reaction model.

| Reaction Process | |
|---------------------------|------------------------------------|
| $\text{Ar} + e$ | $\text{Ar}^+ + e + e$ |
| $\text{O}_2 + \text{O}_2$ | $\text{O} + \text{O} + \text{O}_2$ |
| $\text{O}_2 + \text{O}$ | $\text{O} + \text{O} + \text{O}$ |
| $\text{O}_2 + \text{Ar}$ | $\text{O} + \text{O} + \text{Ar}$ |
| $\text{O} + e$ | $\text{O}^+ + e + e$ |
| $\text{O} + \text{O}$ | $\text{O}_2^+ + e$ |
| $\text{O} + \text{O}_2^+$ | $\text{O}_2 + \text{O}^+$ |

Governing equations and computational method

The governing equations are two-dimensional axisymmetric Navier-Stokes equations extended to chemical non-equilibrium gases. The convection terms were calculated using the SHUS (Simple High-resolution Upwind Scheme [128]) in which the spatial accuracy is extended to third order using the MUSCL approach. Implicit time integration has been done using the LU-SGS (Lower-Upper Symmetric Gauss Seidel Scheme [129]).

Computational grids and conditions

The schematic of computational grid is shown in Fig.4-20. The calculation region is composed of the constrictor-nozzle section and the free jet section. At the interface of these sections, several computational grids were superposed to preserve the spatial accuracy. It was not necessary to concentrate the grid points near the wall surface, because entire region in the constrictor and nozzle is covered by boundary layers.

The grid spacing in the radial direction Δr should be so small that the numerical dissipation effect is smaller than actual diffusion. To have a grid convergence, Δr was set at 1.3mm and total number of grid points was about 10,000.

The same operational conditions as those in the experiment were computed. Subsonic inflow conditions are employed for the inlets of constrictor and of oxygen injection slit. To simulate the cathode jet phenomenon, Gaussian temperature distribution was assumed at the inlet as shown in Fig.4-21. The degree of ionization of argon at the inlet was computed assuming the Saha equilibrium. As for the wall of the constrictor and nozzle, adiabatic non-slip wall conditions were adopted.

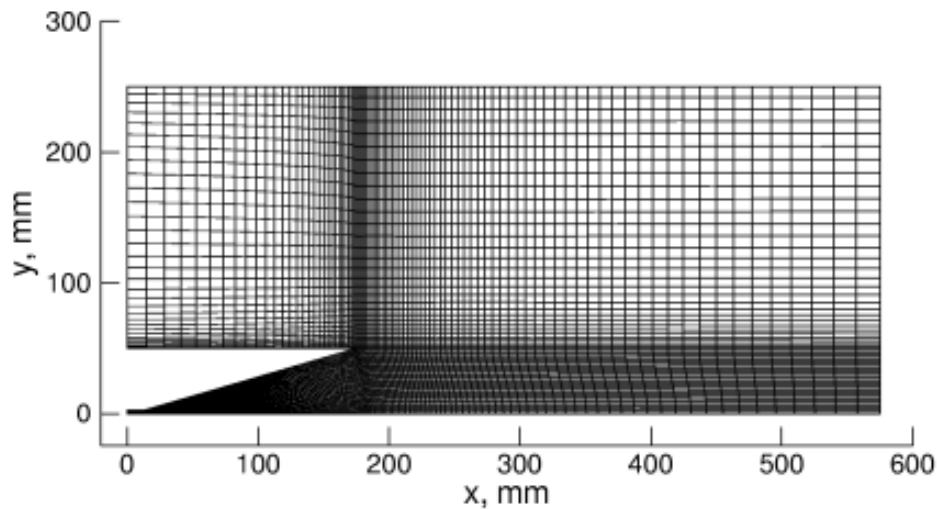


Fig.4-20 Computational mesh.

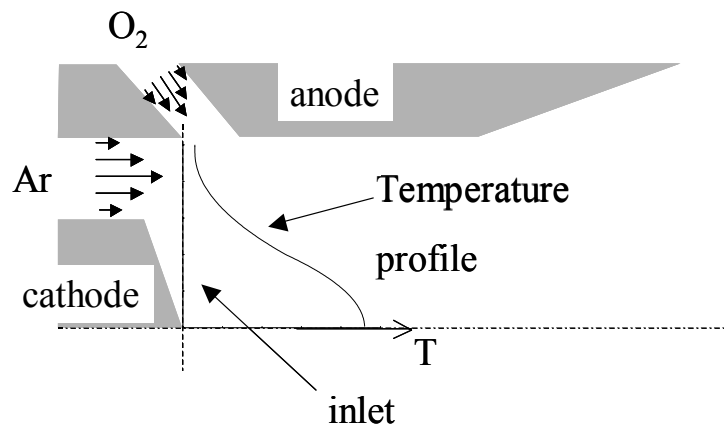


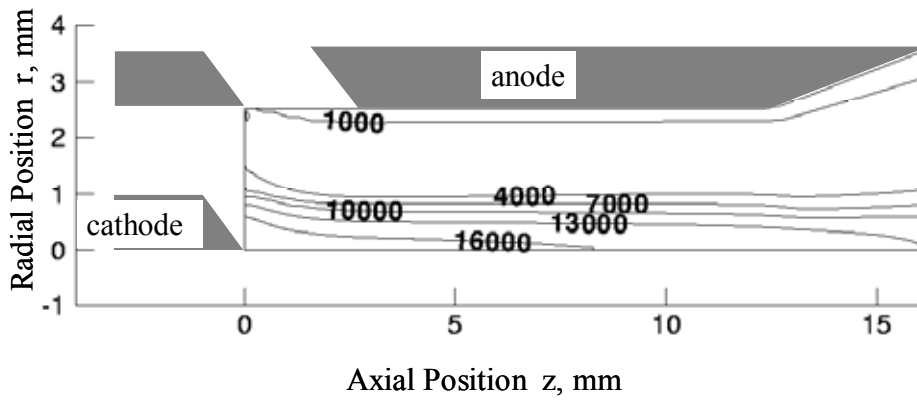
Fig.4-21 Gas inlet conditions.

4.5.2 Results and Discussion

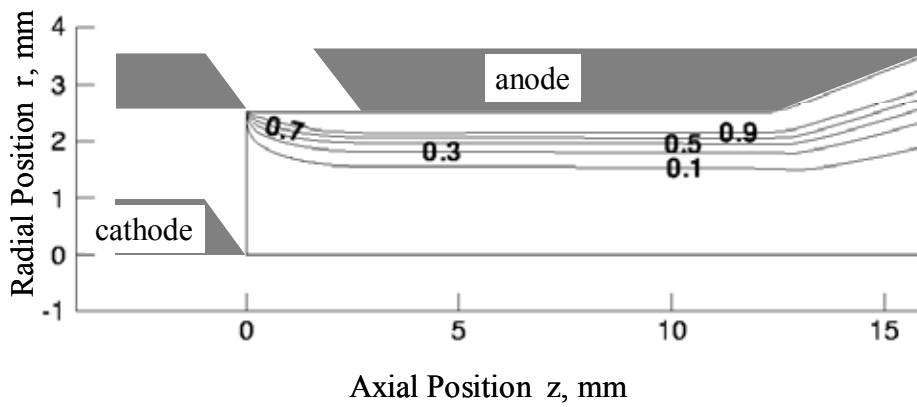
The contours of O₂ mole fraction, temperature and O mole fraction in the constrictor part of the JUTEM arc-heater are shown in Fig. 4-22 and the radial distributions of these properties at 10 mm downstream from the cathode tip are plotted in Fig. 4-23. Oxygen mixing is very slow and it is localized at outer side of the plume in the constrictor. Although the degree of dissociation is very high near the axis due to the high temperature cathode jet, OI mole-fraction is very small.

OI number density distributions are shown in Fig.4-23-25. As seen in these figures, the peak is located off axis at $z=0\sim 30\text{mm}$ and on axis in the downstream of the plume, similarly to that in Fig.4-16, 17.

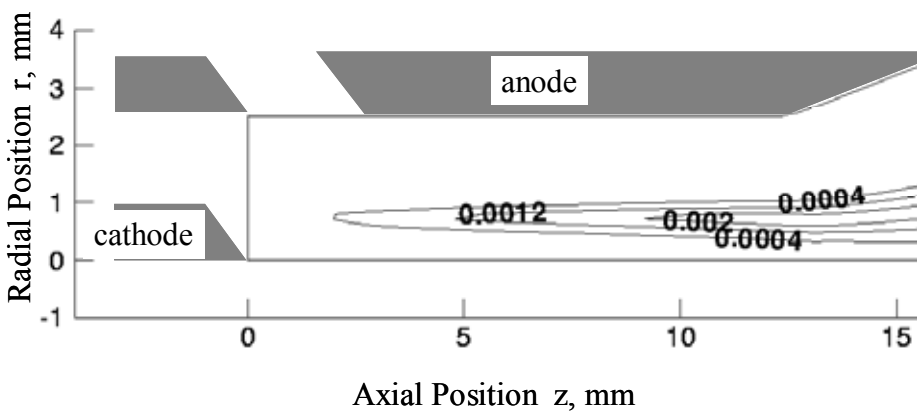
Consequently, this slow mixing process would be the reason why the measured distribution OI at the absorbing state has a peak off axis at the nozzle exit. Although the oxygen is mixed gradually in the plume, the reaction rate is quite small there because of the decrease in temperature. In the plume, the volume-averaged degree of dissociation is estimated at 0.01%.



(a) Temperature



(b) Mole fraction of molecular oxygen



(c) Mole fraction of atomic oxygen

Fig.4-22 Contours of the computed gas properties in the constrictor.

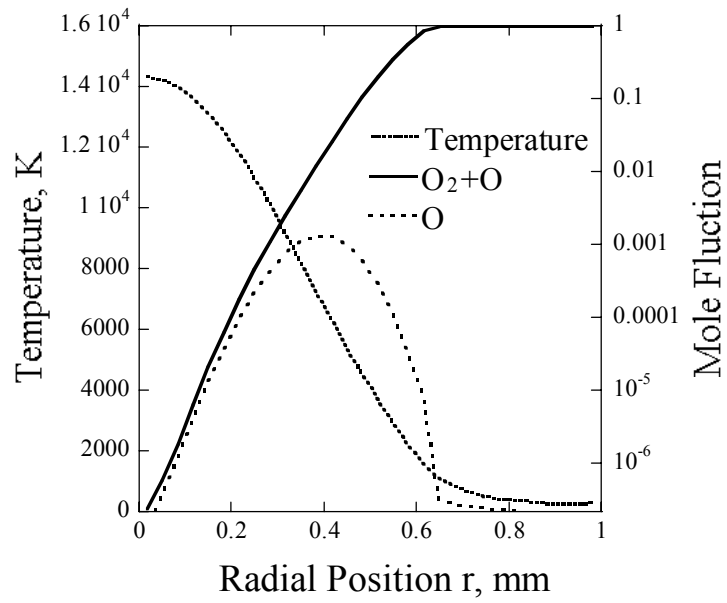


Fig.4-23 Radial distributions of temperature and oxygen mole fractions in the constricter.

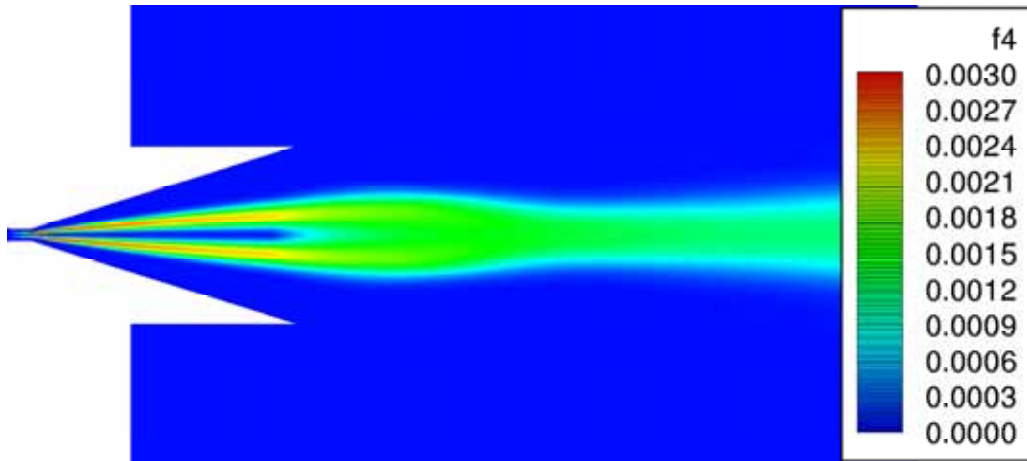


Fig.4-24 Computed contours of number density of atomic oxygen in the University of Tokyo arc-heater plume.

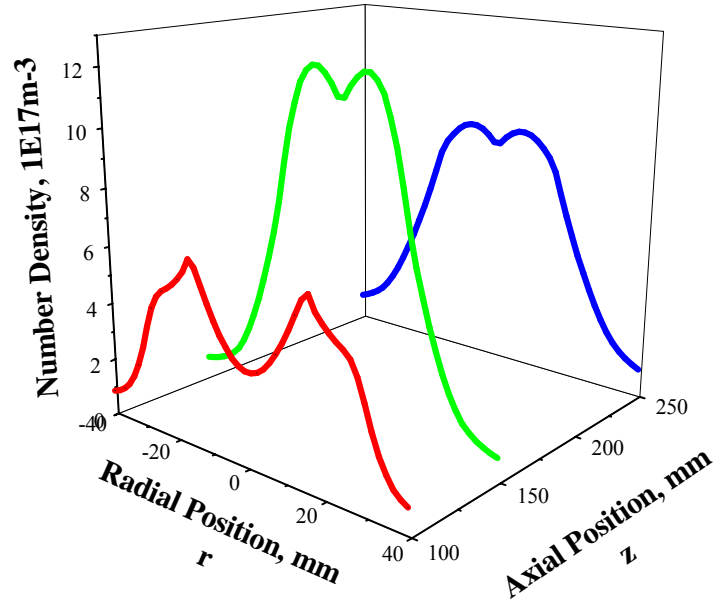


Fig. 4-25 Number density distributions of atomic meta-stable oxygen simulated for University of Tokyo arc-heater plume.

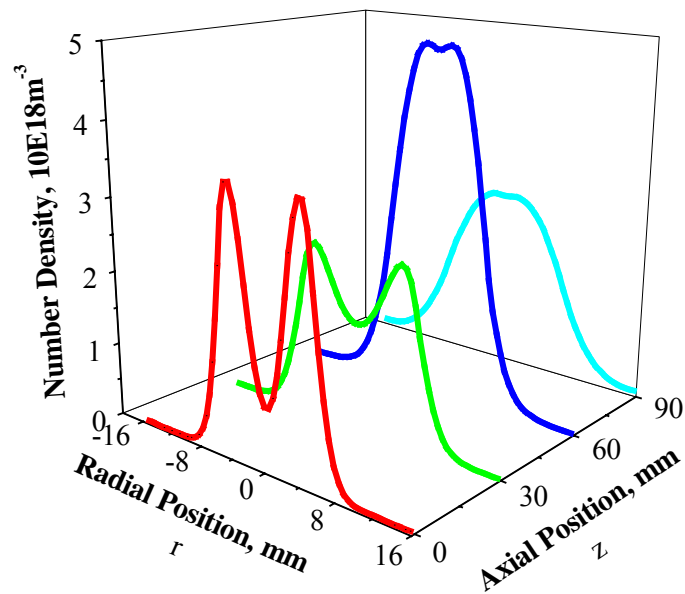


Fig. 4-26 Number density distributions of atomic meta-stable oxygen simulated for University of Tokyo arc-heater plume.

4.6 Summary

LAS was applied to the measurement of the two kinds of constricted arc plasma wind tunnel flows.

Number density distributions of atomic meta-stable oxygen were obtained from the measured absorption line profile at 777.19 nm in argon-oxygen plumes generated by arcjet type arc-heaters. As a result, it was found that the oxygen is localized off axis at the nozzle exit, and diffuses from outside toward the centerline in the plume.

Moreover, numerical simulation was conducted to investigate the diffusion process of the oxygen in the arc-heater. The result indicates that the maximum degree of oxygen dissociation would be at the level of 0.01%.

Chapter 5

Application to ICP Flows

5.1 Facilities

5.1.1 PWK3 system

A plasma wind tunnel (PWK3) including an inductively heated plasma generator (IPG3) has been developed at IRS, Stuttgart University [7, 19, 37, 129]. A schematic of PWK3, its photo and are shown in Figs. 5-1, 2. The size of the vacuum chamber is 2m in length and 1.6m in diameter. The maximum pumping power of the vacuum system is up to $250000\text{m}^3/\text{h}$ at 10Pa, which corresponds to the pressure at the altitude of 90km.

In IPG3, a Meissner type resonant circuit is used as a RF oscillator. Its operational frequency can be optimized to achieve high energy coupling efficiency for various gas species by changing the capacitance (6 nF~42 nF) as well as changing a coil, as shown in Fig.5-3. The range of the frequency in this circuit is from 0.5 MHz to 1.6 MHz.

A schematic of IPG3 and its photo are shown in Figs.5-4, 5. IPG3 consists of an induction coil, a quartz tube containing plasma and a gas injection head. The induction coil made of copper has 5 turn with its inductivity of $2\ \mu\text{H}$. Both the induction coil and quartz tube are surrounded by an external tube and cooled to protect the tube from overheating. Various gases can be injected with swirl to stabilize the plasma.

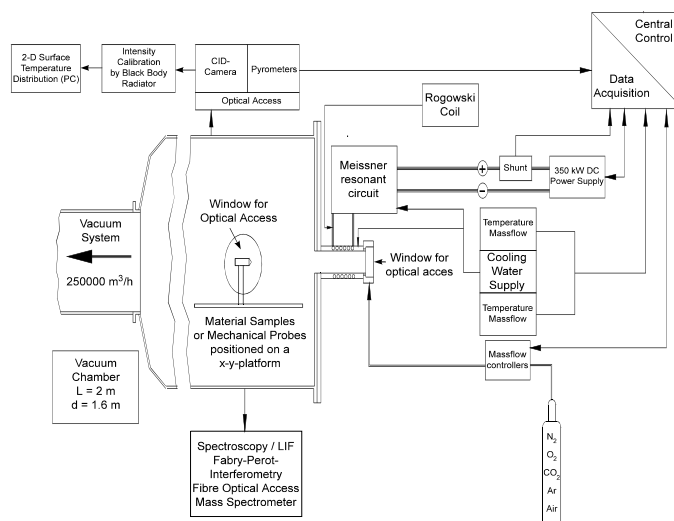


Fig. 5-1 Schematic of PWK3.



Fig. 5-2 Photo of PWK3.

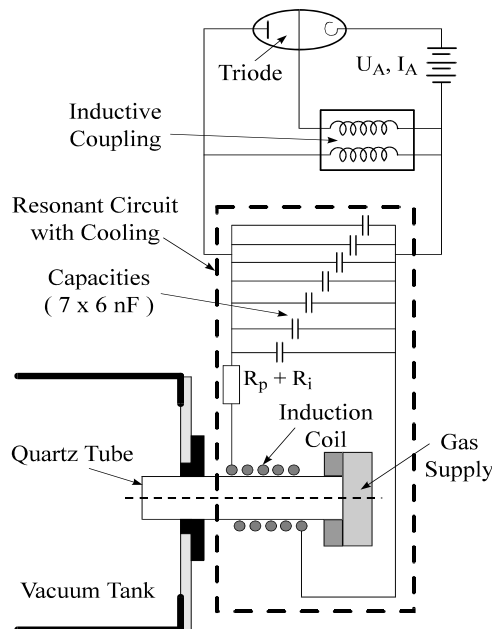


Fig. 5-3 Schematic of Meissner type resonant circuit.

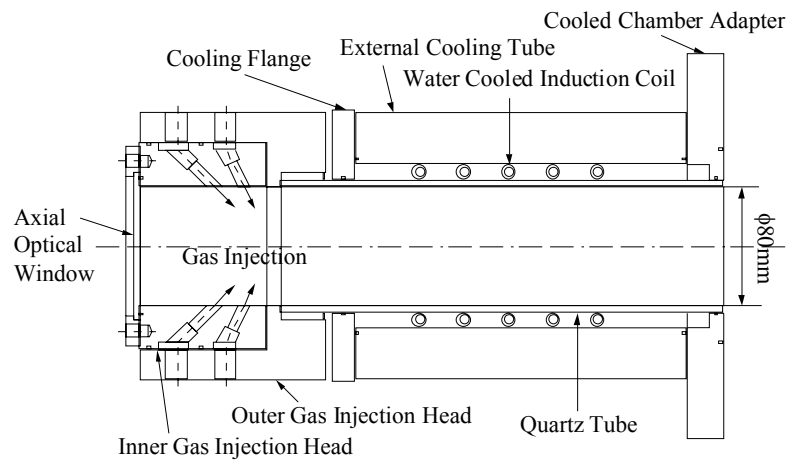


Fig. 5-4 Schematic of IPG3



Fig. 5-5 photo of IPG3

5.2 Test conditions and Previous tests

Various intrusive measurements using a calorimeter, Pitot probe, Mach probe, and heat flux probe have been applied to the flows [130-139]. The operational condition and measured parameters by these methods are tabulated in Tables 5-1 and 2, respectively.

Figure 5-6 shows that the induction current has a specific characteristic. A plasma emission signal measured by a photo detector is also plotted in the figure. Both signals fluctuate at 300 Hz. This fact implies that the flow generated by IPG3 is not stationary.

Figure 5-7 shows that the measured region was $0 < r < r_{\max}$ at 130 mm downstream from the generator exit. Axisymmetric distributions of flow properties were assumed here; r represents the radial coordinate. In this experiment, r_{\max} was set at 50 mm, which is equal to the generator exit radius. The test condition of IPG3 in LAS measurements is also the same with previous tests as shown in Table 5-1.

Table 5-1. Operational conditions.

| Operational condition | Value |
|------------------------------------|--------|
| Working gas | O2 |
| Mass flow | 3 g/s |
| Anode Power Panode | 110 kW |
| Coil turn | 5.5 |
| Number of capacitors | 4 |
| Chamber ambient pressure p_{amb} | 30 Pa |

Table 5-2 Measured parameters [139].

| Parameter | Value |
|----------------------------------|-----------------------|
| Plasma power P_{plasma} | 28.2 kW |
| Total pressure p_0 | 410 Pa |
| Mach number M | 3 |
| Heat flux density q | 2.1 MW/m ² |

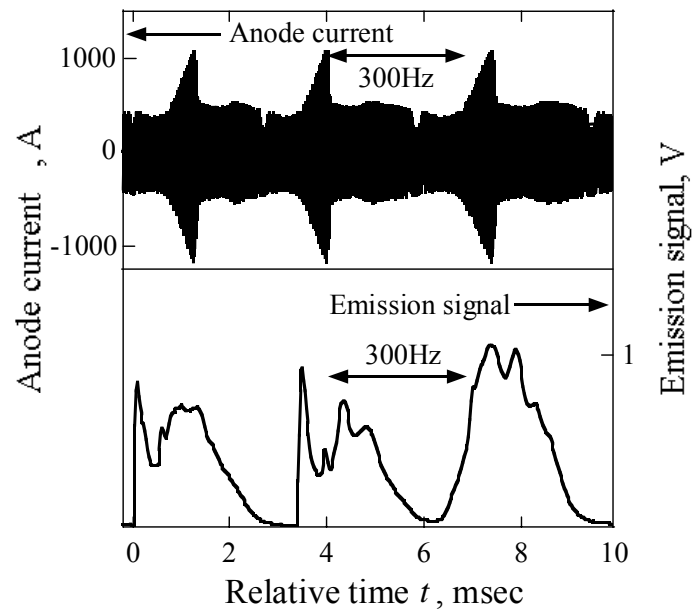


Fig. 5-6 Induction current and plasma emission signal.

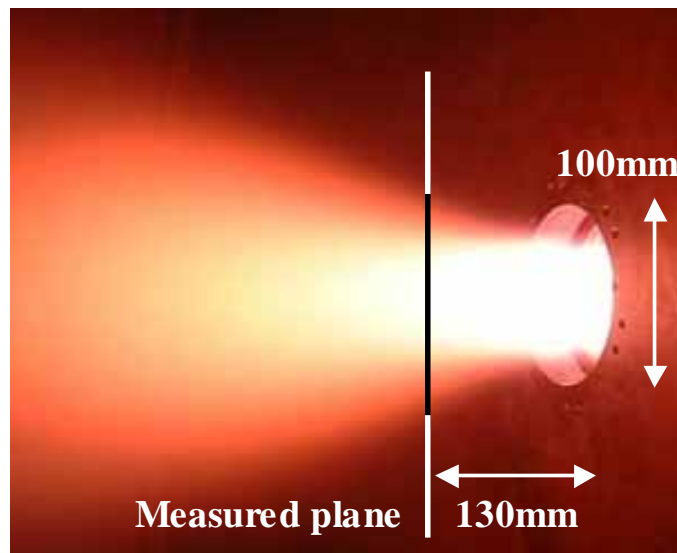


Fig. 5-7 Photo of IPG3.

5.3 Results

Figure 5-8 shows the history of an absorption signal at the fixed laser frequency along with an emission signal. The absorption signal fluctuated in synchronization with the emission signal with a period t of 3.3 ms. Although the absorption signal decreases every 3.3 ms, it sometimes goes to zero and sometimes not. The signal traces can be categorized into two modes: in Mode 1, the trace starts from zero absorption condition, in which plasma has been distinguished for some time; in Mode 2, the trace starts increasing from non-zero absorption condition, in which plasma is sustained even at the minimum energy input.

Typical signals that were recorded with frequency modulation are shown in Fig. 6 along with an ethalon signal. We recorded 40 cycles of frequency modulation for each measurement position. Absorption coefficients are extracted every 0.4 ms and rearranged according to elapsed time t and the modes. Thereby, we obtained an instantaneous absorption profile. Figure 5-9 shows typical absorption coefficients that were extracted from the absorption signal. Here, the origin of time, $t=0$, is set at the minimum signal in each cycle.

Figure 5-10 shows instantaneous absorption profiles that were reconstructed through Abel inversion. Figure 5-11 shows that the history of T , as deduced from line broadening, was very similar to that of the emission signal. Here, T at $\tau=0$ in Mode 2 was set at 75 K, assuming isentropic expansion of cold gas from the generator. The maximum temperature was 9500 K.

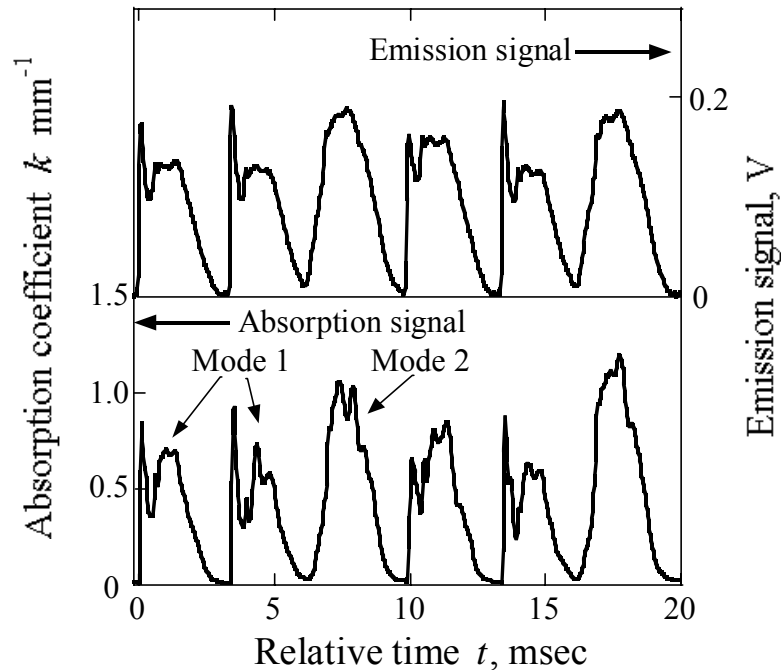


Fig. 5-8 Absorption signal at $\nu=\nu_0 - 4$ GHz and emission signal, $r=0$ mm.

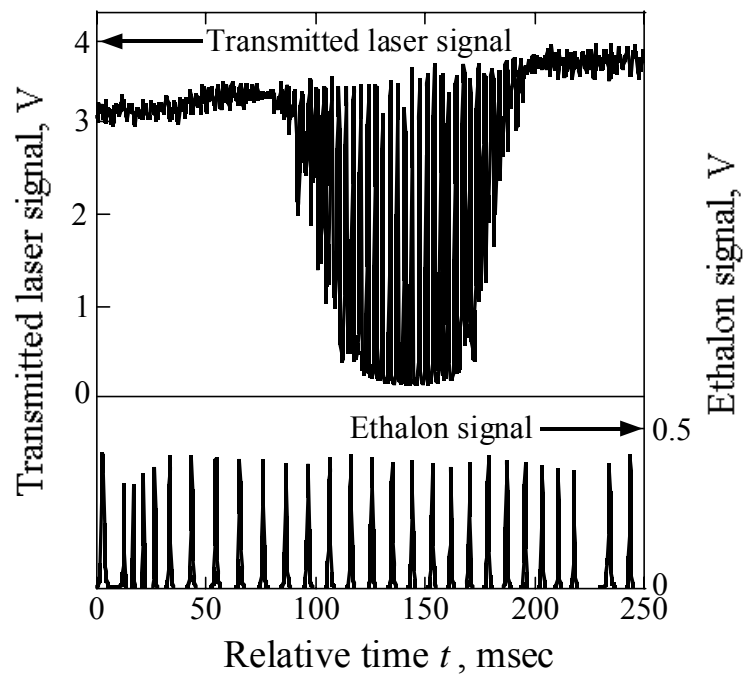


Fig. 5-9 Typical transmitted laser and ethalon signals, $r=0$ mm.

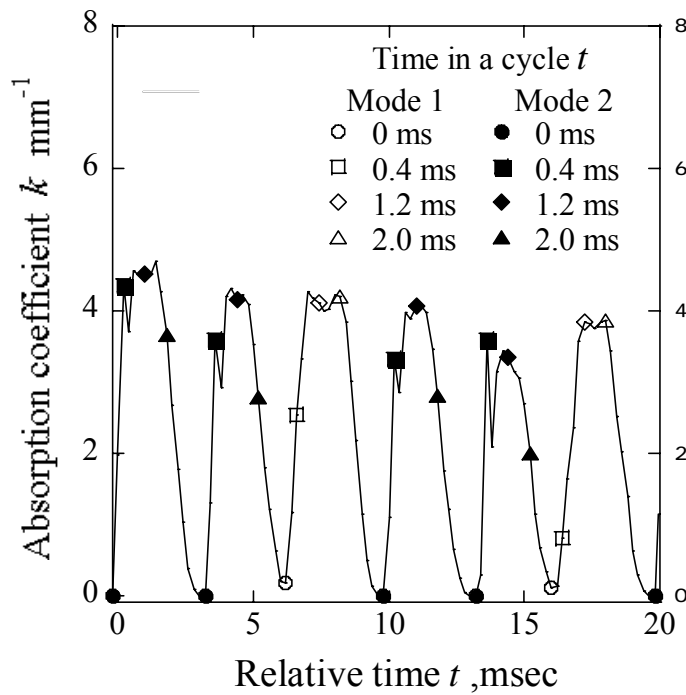


Fig. 5-10 Typical absorption coefficient and extracted one in each cycle, $r=0$ mm.

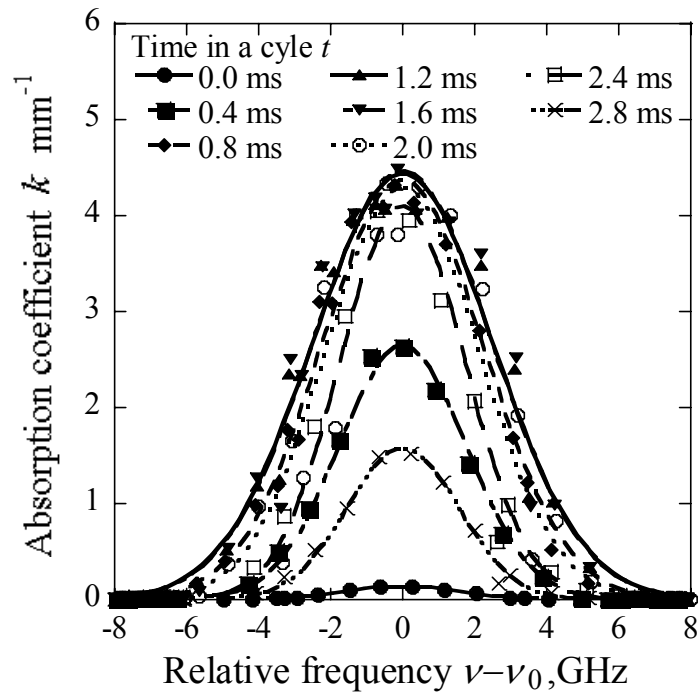


Fig. 5-11 Temporal variations of absorption profile in Mode 1, $r=0$ mm.

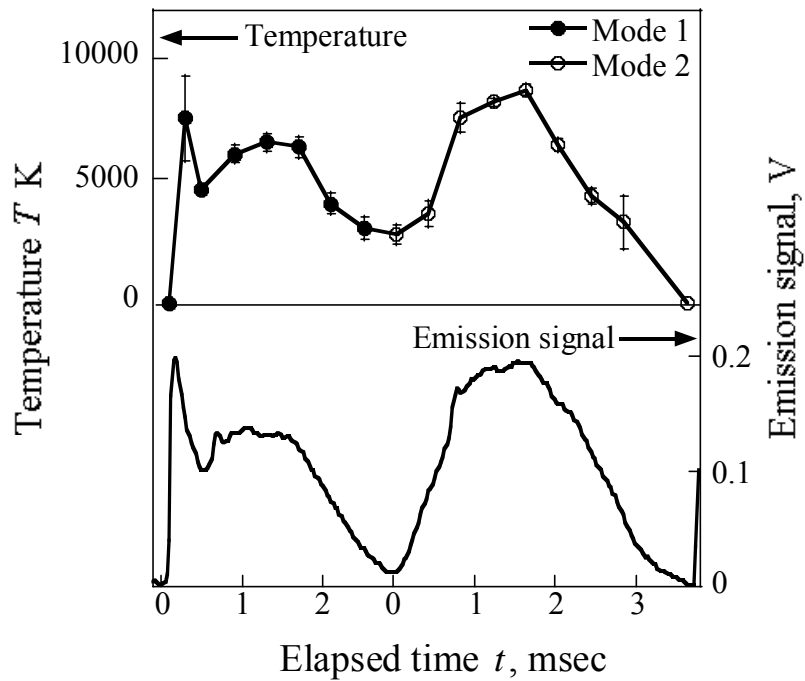


Fig. 5-12 History of translational temperature and emission signal, $r=0$ mm.

5.4 Discussion

5.4.1 Temporal variation of plasma properties

The specific total enthalpy, h_0 , is the sum of static enthalpy $\int C_p dT$, chemical potential h_{chem} and kinetic energy $u^2/2$, expressed as

$$h_0 = \int C_p dT + h_{\text{chem}} + \frac{1}{2}u^2. \quad (5-1)$$

Here, C_p is the specific heat at constant pressure and u is the flow velocity expressed as

$$u = M \sqrt{\gamma RT}. \quad (5-2)$$

Here, γ and R are the specific heat ratio and the gas constant, respectively.

Thermo-chemical equilibrium is assumed for simplicity and we estimate h_0 and mole fractions from the measured T . Three chemical species, O_2 , O , and O^+ , and two chemical reactions $O_2 \rightleftharpoons 2O$ and $O \rightleftharpoons O^+ + e^-$ are considered. Their equilibrium constants were obtained from Ref. [125]. C_p is computed as the sum of the contributions of each species. Figure 5-13 shows calculated equilibrium properties at $p_{\text{amb}}=30$ Pa.

Figure 5-14 shows the history of estimated properties on the plume axis. Maximum h_0 was 86 MJ/kg and the averaged degree of dissociation of oxygen is about 0.92. At the highest enthalpy, the mole fraction was 0.7 because of ionization. Its degree of dissociation was very high. For that reason, it would be useful for precise evaluation of catalytic effects for various TPS materials.

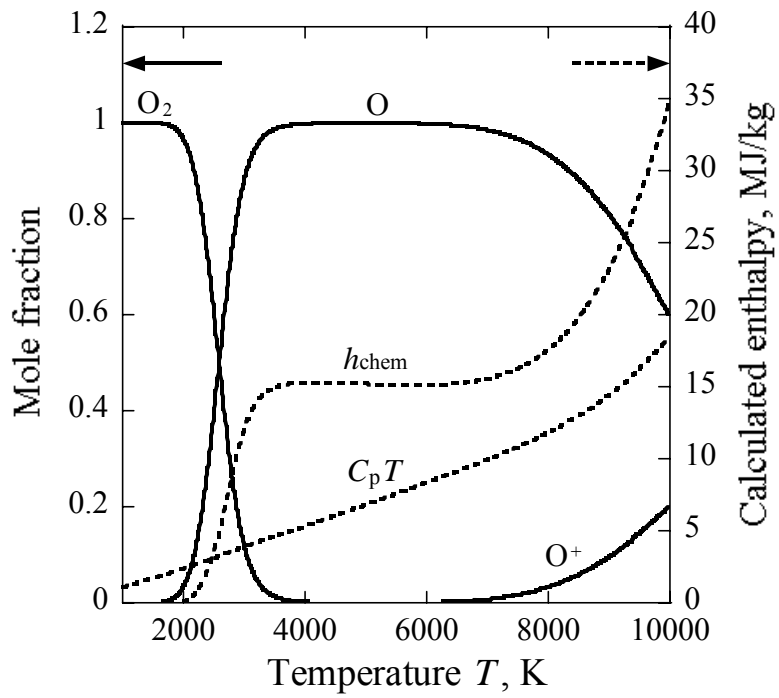


Fig. 5-13 Calculated enthalpy and mole fractions by thermo-chemical equilibrium assumptions, $p_{amb}=30$ Pa.

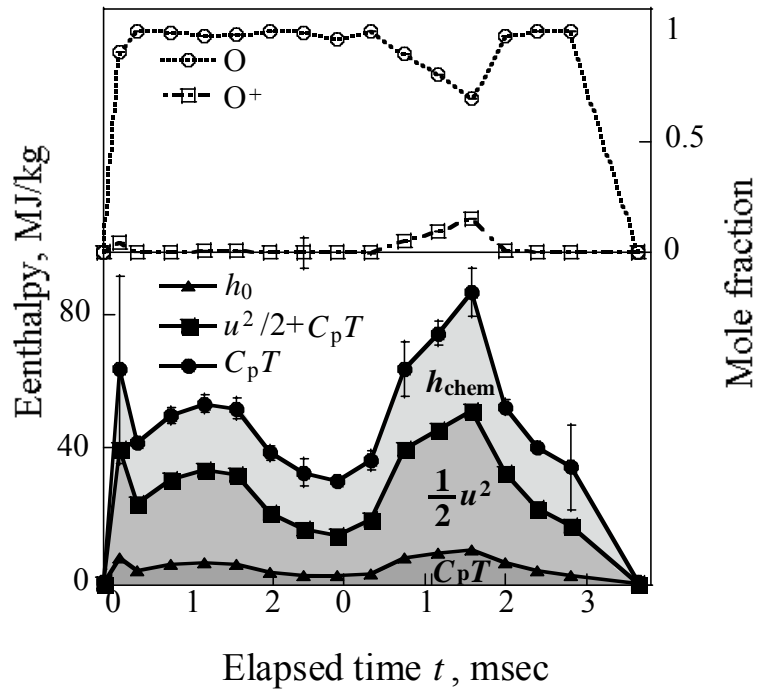


Fig. 5-14 History of estimated enthalpy and mole fractions, $r=0$ mm.

5.4.2 Time averaged specific total enthalpy

The time-averaged specific total enthalpy $\bar{h}_0(r)$ is defined as

$$\bar{h}_0(r) = \frac{\int_0^r h_0(r,t) \rho(r,t) u(r,t) dt}{\int_0^r \rho(r,t) u(r,t) dt} \quad (5-3)$$

where $\rho(r,t) = p_{\text{amb}}/k_B T(r,t)$.

Figure 5-15 shows the distribution of $\bar{h}_0(r)$ with that estimated from the probe measurements described next section. Although it took a maximum of 33.7 ± 2.9 MJ/kg on the axis, the profile was almost flat for the TPS probe area ($r < 10.5$ mm). Figure 5-16 shows the enthalpy balance at $r=0$, where \bar{h}_{chem} accounted for 42.5% of $\bar{h}_0(r)$.

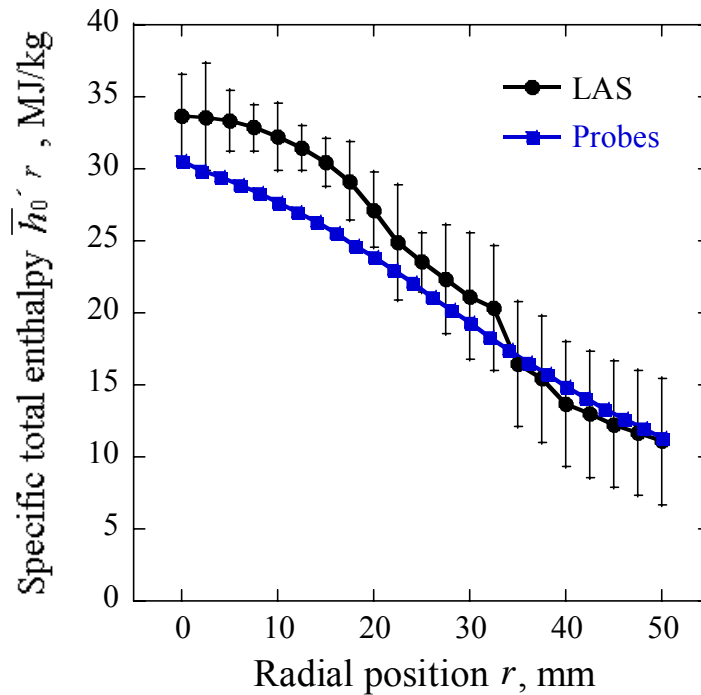


Fig. 5-15 Time-averaged specific total enthalpy distribution by LAS and Probes.

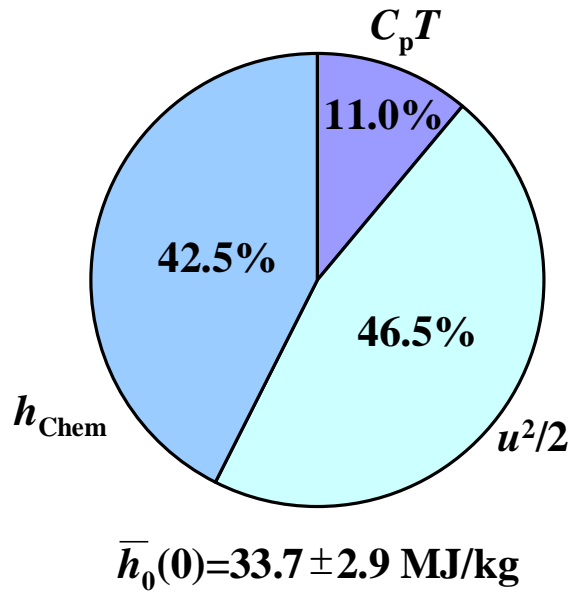


Fig. 5-16 Enthalpy balance, $r=0$ mm.

5.4.3 Comparison with intrusive measurements

Plasma power $P_{\text{plasma}, r < r_{\text{max}}}$ and the mass flow rate $\dot{m}_{r < r_{\text{max}}}$ contained in the measured cylinder of the flow are obtained as

$$P_{\text{plasma}, r < r_{\text{max}}} = \int_0^{r_{\text{max}}} 2\pi r \rho(r) u(r) \bar{h}_0(r) dr . \quad (5-4)$$

$$\dot{m}_{r < r_{\text{max}}} = \int_0^{r_{\text{max}}} 2\pi r \rho(r) u(r) dr . \quad (5-5)$$

Table 5-3 shows those results in comparison with the calorimeter measurements [139]. Figure 5-7 shows that $P_{\text{plasma}, r < r_{\text{max}}}$ in LAS is smaller than those of calorimeter measurements because the flow has expanded to the region of $r > r_{\text{max}}$.

Table 5-3 Comparison of Pplasma

| Method | rmax | Pplasma |
|---------------|-------|---------|
| LAS (Present) | 50 mm | 17.5 kW |
| Calorimeter22 | 60 mm | 28.2 kW |

In Ref. [139], $\bar{h}_0(r)$ was estimated from the measured $\dot{q}(r)$, $p_0(r)$, and P_{plasma} using Pope's relation as 23

$$\bar{h}_0(r) = \frac{r_{\text{max}}^2}{2} \frac{\dot{q}(r)/\sqrt{p_0(r)}}{\int_0^{r_{\text{max}}} (\dot{q}(r)/\sqrt{p_0(r)}) r dr} \frac{P_{\text{plasma}, r < r_{\text{max}}}}{\dot{m}_{r < r_{\text{max}}}}. \quad (5-6)$$

Here, $\dot{m}_{r < r_{\text{max}}} = \dot{m} = 3\text{g/s}$ was assumed regardless $r_{\text{max}} = 60$ mm. Table 6-4 shows a comparison between intrusive measurements and present study. Results show good agreement. The values would more closely resemble one another than those in Table 5-4 if $\dot{m}_{r < r_{\text{max}}}$ is estimated precisely in intrusive measurements.

Table 5-4 Comparison of $\bar{h}_0(0)$

| Method | $\bar{h}_0(0)$ |
|--------------------------|----------------|
| LAS (Present) | 33.7±2.9 MJ/kg |
| Intrusive measurements22 | 30.5 MJ/kg |

5.5 Summary

LAS was applied for the diagnostics of IPG3 pure oxygen flow. The flows were non-stationary and its emission and absorption signals were found to fluctuate at 300 Hz because of the fluctuation of anode power.

Then, temporal and spatial translational temperature distributions were measured. The maximum temperature was found to be 9000 K instantaneously.

The corresponding averaged degree of dissociation of oxygen estimated by the measured temperature and thermo-chemical equilibrium calculation is more than 0.90. The total enthalpy was estimated as 33.7 ± 2.9 MJ/kg; 43% of it was possessed as the chemical potential. These results show good agreement with intrusive measurements.

Chapter 6

Conclusion

A diode laser absorption spectroscopy system applicable to low-pressure plasma has been successfully developed with following remarks.

1) Development of LAS system

Error analysis

Relationship of errors between translational temperature and measured fractional absorption were analytically investigated. As a result, translational temperature is estimated with in 5 % error for fractional absorption more than 10^{-2} with its measurement error of 10-2 %. This fractional absorption requires number density more than 10^{15} m^{-3} in OI 777.19 nm line with 1cm optical path.

Absorption saturation

When probe laser intensity I is higher, strong absorption saturation was observed. As a result, absorption coefficients were found to decrease with laser intensity according to the conventional laser theory. Then, number density should be estimated using the theory.

On the other hand, Doppler broadening of absorption line becomes wider with laser intensity, and the temperature deduced from the broadening tends to be overestimated in contradiction to the theory. This result is caused by the dependency of saturation intensity I_{S_inhomo} on the frequency: Absorbers showing larger Doppler shift $|n-n_0|$ have higher averaged velocity, and then increases with relative frequency $|n-n_0|$.

Therefore, in case of $I/I_{S_inhomo} > 10^{-1}$, where strong laser intensity is necessary due to strong plasma emission, measured temperature should be calibrated by the correction factor presented in this paper, though in case of $I/I_{S_inhomo} > 10^{-1}$, temperature is precisely measured.

2) Application to Plasma Wind Tunnel Flows

Next, this system was applied to two kinds of plasma wind tunnel flows and various properties of the flows were successfully clarified. Also portability of this system is proved by measurements in other facilities in Japan and Germany.

Constricted arc heater flows: mixing process of oxygen

Oxygen injected at the constrictor was found not enough mixed with argon base flow at the nozzle exit. The oxygen slowly diffused toward the axis in the downstream region of the plume, resulting in the quite small degree of dissociation of oxygen at the level of 0.01%. For the enhancement of the oxygen dissociation, the oxygen injection method should be improved to promote the mixing between oxygen and argon.

ICP flows: Temperature measurements and enthalpy estimation

Laser absorption spectroscopy was successfully applied for the diagnostics of non-stationary IPG3 flow. Consequently, the averaged degree of dissociation of oxygen is more than 0.92. The total enthalpy was estimated as 33.7 ± 2.9 MJ/kg; 43% of it was possessed as the chemical potential. These results show good agreement with intrusive measurements.

Reference

- [1] Bertin, J. J., "Hypersonic Aerothermodynamics," AIAA Education Series, AIAA, Inc., Washington, DC, 1994
- [2] Throckmorton, D. A., "Shuttle Entry Aerothermodynamic Flight Research: The Orbiter Experiments Program," *Journal of Spacecraft and Rockets*, Vol. 30, No. 4, 1993, pp. 449-465.
- [3] Gnoffo, P. A., Braun, R. D., Weilmuenster, K. J., Mitcheltree, R. A., Engelund, W. C., and Powell, R. W., "Prediction and Validatin of Mars Pathfinder Hypersonic Aerodynamic Data Base," AIAA Paper 98-2445, June 1998.
- [4] Seiff, A., Kirk, D. B., Young, R. E., Blanchard, R. C., Findlay, J. T., Kelly, G. M., and Sommer, S. C., "Measurement of Thermal Structure and Thermal Contrasts in the Atmosphere of Venus and Related Dynamical Observations: Results from the Four Pioneer Venus Probes," *Journal of Geophysical Research*, Vol. 85, NO. A13, 1980, pp. 7903-7933.
- [5] Tauber, M., Wercinski, P., Henline, W., Paterson, J., and Yang, L., "Uranus and Neptune Atmospheric-Entry Probe Study," *Journal of Spacecraft and Rockets*, Vol. 31, No. 5, 1994, pp. 799-805.
- [6] http://spaceinfo.jaxa.jp/db/kensaku_html/type1_j.html
- [7] Auweter-Kurtz, M., "Overview of IRS Plasma Wind Tunnel Facilities," *Measurement Techniques for High Enthalpy and Plasma Flows*, NATO Research and Technology Organization proceedings RTO-EN-8, Neuilly-Sur-Seine Cedex, France, 2000, pp. 2A-1-1A-20.
- [8] Anfimov, N., "TSNIIMASH Capabilities for Aerogasdynamic and Thermal Testing of Hypersonic Vehicles," AIAA Paper 92-3962, June 1992.
- [9] Kubota, H., Suzuki, K., and Watanuki, T., "Aerothermodynamics of Space Vehicles," University of Tokyo Press, 2002
- [10] Park, C., "Laboratory Simulation of Aerothermodynamic Phenomena: A Review," AIAA Paper 92-4025, 1992.
- [11] Smith, R. K., Wagner, D. A., and Cunningham, J. W., "A Survey of Current and Future Plasma Arc-heated Test Facilities for Aerospace and Commercial Applications," AIAA Paper 98-0146, Jan. 1998.
- [12] Gladisch, H., "How Huels Makes Acetylene by D.C. Arc," *Hydrocarbon Proceeding and Petroleum Refining*, Vol. 41, No. 6, 1962.
- [13] Eschenbach, R. C., and Skinner, G. M., "Study of Arc Heaters for Hypersonic Wind Tunnel," WADD Technical Report 60-354, May 1960.
- [14] Smith, R. T., and Kachel, W. A., "Design and Performance of a High Pressure, Continuous

- Flow Arc Heater,” AFFDL TR-66-48, May 1966.
- [15] Painter, J. H., and Ehmsen, R. J., “Development of a High Performance Arc Heater for Ground Testing Advanced Strategic Reentry Vehicle Components,” AIAA Paper 71-259, March 1971.
- [16] Stine, H. A., “The Hyperthermal Supersonic Aerodynamic Tunnel,” International Symposium on High Temperature Technology, Asilomar, CA, 1963.
- [17] Shepard, C. E., Watson, V. R., and Stine, H. A., “Evaluation of a Constricted-Arc Supersonic Jet,” NASA TN D-2066, 1964.
- [18] Shepard, C. E., “Advanced High-Power Arc Heaters for Simulating Entries into the Atmospheres of the Outer Planets,” AIAA Paper 71-263, 1971.
- [19] Auweter-Kurtz, M., Hammer, F., Herdrich, G., Kurtz, H., Laux, T., Schreiber, E., and Wegmann, T., “The Ground Test Facilities for TPS at the Institut für Raumfahrtssysteme,” 3rd European Symposium on Aerothermodynamics for Space Vehicles, ESTEC, Noordwijk, NL, Nov. 1998.
- [20] Nishida, M., Watanabe, Y., “Preliminary Experiments of Atomic Oxygen Generation for Space Environmental Testing,” *Trans. Japan Soc. Aero. Space Sci.* Vol.31, No.93, p123-133
- [21] Lago, V., Lebehot, A., and Dudeck, M., “Facilities of the Laboratoire d’Aerothermique for the Simulation of Planetary Entry and Earth Re-entry,” First Joint French-German Symposium on Simulation of Atmospheric Entries by Means of Ground Test Facilities, Nov. 1999.
- [22] Mayo, R. et al., “A Magnetically Rotated Electric Arc Air Heater Employing a Strong Magnetic Field and Copper Electrodes,” NASA TN D 2032, Nov. 1963
- [23] Barr, T. and Cason, C., “Multiple Arc Performance in an 8000 kW Plasma Facility,” Eighth Symposium on Engineering Aspects of MHD, Stanford, CA, Mar. 1967.
- [24] Lagutin, V., and Lapygin, V., “Typical Balance Test Tasks for Aerogasdynamic Facilities of TsNIMASH,” NASA/CP-1999-20101, NASA Langley Research Center, 1999, pp. 385-392.
- [25] Shepard, C. E., et al., “A High Enthalpy Plasma Generator for Entry Heating Simulation,” NASA TN D-4588, 1968.
- [26] Felderman, E. J., Chapman, R., Jacocks, J. L., Horn, D. D., and Bruce, W. E., “High-Pressure Arc Heater Development and Modeling: Status and Requirements,” *Journal of Propulsion and Power*, Vol. 12, No. 6, 1996, pp. 1044-1051.
- [27] Vecchio, A. D., Purpura, C., and Filippis, F. D., “Cold Air Injection and Mixing in Scirocco Hypersonic Large Scale Arcjet Facility,” AIAA Paper 2003-6959, Dec. 2003
- [28] Balter-Peterson, A., Nichols, F., Mifsud, B., and Love, W., “Arcjet Testing in NASA Ames Research Center Thermophysics Facilities,” AIAA Paper 92-1071, 1992
- [29] Smith, R. K., Wagner, D. A., Cunningham, D. J., Painter, J. H., Itagaki, H., Watanabe, Y., and Hasegawa, S., “High Enthalpy Material Test Facility Design Improvements in Japan,” AIAA Paper 94-2592, June 1994.
- [30] Yamada, T., and Inatani, Y., “Arc Heating Facility and Test Technique for Planetary Entry

- Missions,” ISAS SP, No.17, 2003
- [31] Grimaud, J., “Orbiter TPS Development and Certification Testing at the NASA/JSC 10 MW Atmospheric Reentry Materials and Structures Evaluation Facility,” AIAA Paper 83-0147, Jan. 1983
- [32] Pugh, E. R., Patrick, R. M., and Schneiderman, A. M., “High-Pressure, High-Enthalpy Test Facility,” *AIAA Journal*, Vol. 9, No. 2, 1971
- [33] Huegel, H., “Arc-Heater for High-Enthalpy Plasma Flows,” Third International Conference on Gas Discharges, London, 1974.
- [34] Schonemann, A., and Auweter-Kurtz, M., “The Plasma Wind Tunnels PWK1 and PWK2,” IRS-92 P6, July 1992.
- [35] Reboux, J., and Morvan, D., “Inductive Thermal Plasma,” Industrial Applications of Induction of SEE.
- [36] Gordeev, A. N., “Overview of Characteristics and Experiments in IPM Plasmatrons,” Measurement Techniques for High Enthalpy and Plasma Flows, NATO Research and Technology Organization Proceedings RTO-EN-8, Neuilly-Sur-Seine Cedex, France, 2000, pp. 1A-1-1A-18.
- [37] Herdrich, G., Auweter-Kurtz, M., Kurtz, H., Laux, T. and Winter, M., “Operational Behavior of Inductively Heated Plasma Source IPG3 for Entry Simulations,” *Journal of Thermophysics and Heat Transfer*, Vol. 16, No. 3, 2002, pp. 440-449.
- [38] Bottin, B., Carbonaro, M., Van Der Haegen, V., Paris, S., and Charbonnier, J. M., “Reentry Simulation Capability of the VKI 1.2 MW Plasmatron,” First Joint French-German Symposium on Simulation of Atmospheric Entries by Means of Ground Test Facilities, Nov. 1999.
- [39] Ito, T., Ishida, K., Mizuno, M., Sumi, T., Fujita, K., Nagai, J., Murata, H., and Matsuzaki, T., “Heating Tests of TPS samples in 110kW ICP-heated wind tunnel,” ISTS 2004-e-20, 2004.
- [40] Yamada, T., and Inatani, Y., “Inductively-coupled High Enthalpy Flow Generator for Planetary Entry Probes,” ISTS 2004-e-21, 2004
- [41] Gerdeman, D. A., Hecht, N. L., “Arc Plasma Technology in Materials Science,” Springer-Verlag, New York, 1972
- [42] Inatani, Y., Hasegawa, S., and Komatsu, T., “Present Status of Arc Heated Facilities in the World and the Future Plan,” Proceedings of the 26th Symposium on Fluid Mechanics, 1994, pp. 101-104.
- [43] Nishida, M., “Arc-Heated High Enthalpy Gas Flow,” Proceedings of the 32th Symposium on Fluid Mechanics, 2000, pp. S1-S9
- [44] Nakamura, Y., and Ichiguro, M., “Ionization Characteristics of Arc-Heated Wind Tunnel Flow,” *Aeronautical and Space Sciences Japan*, Vol. 43, No. 499, 1995, pp. 467-472.
- [45] Felderman, E. J., Chapman, R., Jacoks, J. L., Horn, D. D., and Bruce W. E., “High-Pressure

- Arc Heater Development and Modeling: Status and Requirements,” *Journal of Propulsion and Power*, Vol. 12, No. 6, 1996, pp. 1044-1051.
- [46] Balboni, J. A., Adler, D., and Goekcen, T., “Measurement and Computation of Flow Properties in the NASA Ames 100 MW Direct Connect Arcjet Facility Scramjet Combustor,” AIAA Paper 95-0294, 1994.
- [47] Wilson, D. R., “Development and Calibration of a Continuous-Flow Arc-Heated Hypersonic Wind Tunnel,” AIAA Paper 90-1381, 1990.
- [48] Vecchio, A. D., Palumbo, G., Koch, U., and Guelhan, A., “Temperature Measurements by Laser-Induced Fluorescence Spectroscopy in Nonequilibrium High Enthalpy Flow,” *Journal of Thermophysics and Heat Transfer*, Vol. 14, No. 2, 2000, pp. 216-224.
- [49] Chazot, O., and Boschek, E., “Plasmatron Facility for Combined Particle-Impact and Aero-Heating Tests,” AIAA Paper 03-4040, 2003.
- [50] Auweter-Kurtz, M., Kurtz, H. L., and Laure, S., “Plasma Generators for Re-entry Simulation,” *Journal of Propulsion and Power*, Vol. 12, No. 6, 1996, pp. 1053-1061.
- [51] Park, C., “Nonequilibrium Hypersonic Aerothermodynamics,” John Wiley and Sons, 1990.
- [52] Sharma, S. P., “Research on Nonequilibrium Phenomena at Ames E.A.S.T. Facility,” 19th International Symposium on Shock Waves, 1993.
- [53] Sharma, S. P., Gellispie, W. D. and Meyer, S. A., “Shock Front Radiation Measurement in Air,” AIAA Paper 91-0573, 1991.
- [54] Babikian, D. S., Gopaul, D. S. and Park, C., “Measurement and Analysis of Nitric Oxide Radiation in an Arcjet Flow,” *Journal of Thermophysics and Heat Transfer*, Vol. 8, No. 4, pp. 737-743.
- [55] Storm, P. V. and Cappelli, M. A., “Laser-induced fluorescence measurements within an arcjet thruster nozzle,” AIAA Paper 95-2381, July 1995.
- [56] Winter, M. W. and Auweter-Kurtz, M., “Boundary layer investigation in front of a blunt body in a subsonic air plasma flow by emission spectroscopic means,” AIAA paper 98-2460, 1998.
- [57] Scott, C. D., “Effects of Nonequilibrium and Wall Catalysis on Shuttle Heat Transfer,” *Journal of Spacecraft*, Vol. 22, No. 5, 1985, pp.489-499.
- [58] Chen, Y. K. and Milos, F. S., “Ablation and Thermal Response Program for Spacecraft Heatshield Analysis,” *Journal of Spacecraft and Rockets*, Vol. 36, No. 3, 1999, pp. 475-483.
- [59] Curry, D. M., Pham, V. T., Norman, I. And Chao, D. C., “Oxidation of Hypervelocity Impacted Reinforced Carbon-Carbon,” *Journal of Spacecraft and Rockets*, Vol. 37, No. 3, 2000, pp. 310-317.
- [60] Armenise, I., Barbato, M., Capitelli, M. and Gorse, C., “Surface Recombination Coefficients and Boundary-Layer Hypersonic Flow Calculations on Different Surfaces,” *Journal of Spacecraft and Rockets*, Vol. 41, No. 2, 2004, pp. 310-313.

- [61] Stockle, S., Fasoulas, S., Auweter-Kurtz, M., "Heterogeneous Catalytic Recombination Reactions Including Energy Accommodation Considerations in High Enthalpy Flows," AIAA Paper 97-2561, 1997.
- [62] Laux, T., Feigl, M., Auweter-Kurtz, M., Stockle, T., "Estimation of Surface Catalyticity of PVD-Coatings by Simultaneous Heat Flux and LIF Measurements in High Enthalpy Air Flows," AIAA Paper 00-2364, 2000.
- [63] Auweter-Kurtz, M., "Diagnostic Tools for Plasma Wind Tunnels and Reentry Vehicles at the IRS," Measurement Techniques for High Enthalpy and Plasma Flows, NATO Research and Technology Organization Proceedings RTO-EN-8, Neuilly-Sur-Seine Cedex, France, 2000, pp. 2B-1-2B-78.
- [64] Sharma, S. P., Park, C., Scott, C. D., Arepalli, S., and Taunk, J., "Arcjet Flow Characterization," AIAA Paper 96-0612, 1996.
- [65] Winovich, W., "On the Equilibrium Sonic-Flow Method for Evaluating Electric-Arc Air-Heater Performance," NASA TN D-2132, 1964
- [66] Fletcher, D. G., "Measurement Requirements for Improved Modeling of Arcjet Facility Flows," Measurement Techniques for High Enthalpy and Plasma Flows, NATO Research and Technology Organization Proceedings RTO-EN-8, Neuilly-Sur-Seine Cedex, France, 2000, pp. 3A-1-3A-27.
- [67] Bennett, B. K., "Transient Enthalpy Probe Development," Paper No. 88-0770, Proceedings of the 34th ISA International Instrumentation Symposium, 1988.
- [68] Graves, C. M., Moody, H. L., and Mitchell, J. D., Horn, D. D., "Enthalpy Probe for Arc Heater Flow Diagnostics," AIAA Paper 93-2785, 1993.
- [69] Fay, J. A., and Ridell, F. R., "Theory of Stagnation Point Heat Transfer in Dissociated Air," *Journal of Aeronautical Science*, Vol. 25, No. 2, 1958, pp. 73-85.
- [70] Pope, R. B., "Measurements of Enthalpy in Low Density Arc-Heated Flow," *AIAA Journal* Vol. 4, 1966, pp. 717-716.
- [71] Schoenemann, A. and Auweter-Kurtz, M., "Mass Spectrometric Investigation of High Enthalpy Plasma Flows," *Journal of Thermophysics and Heat Transfer*, Vol. 9, No. 4, 1995, pp. 620-628.
- [72] Bloom, M. H., Lederman, S., and Widhopf, G. F., "Experiments on cylindrical electrostatic probes in a slightly ionized hypersonic flow," *AIAA Journal*, Vol.6, No. 11, 1968, pp. 2133-2139.
- [73] Demtroder, W., "Laser Spectroscopy," second ed., Berlin, Springer Verlag, 1996.
- [74] Griem, H. R., "Plasma Spectroscopy," McGraw-Hill, Inc., 1964.
- [75] Rob, M. A., Mack Jr., L. H., Arepalli, S., and Scott, C. D., "Spectral Measurements in the Plenum of an Arcjet Wind Tunnel," AIAA Paper 95-2126, 1995.
- [76] Herzberg, G., "The Spectra and Structure of Simple Free Radicals," Cornell University Press,

New York, 1971.

- [77] NIST Molecular Spectra Database, <http://physics.nist.gov/PhysRefData/MolSpec/>
- [78] Park, C., "Nonequilibrium Air Radiation (NEQAIR) Program: User's Manual," NASA TM 86707, 1985.
- [79] Fujita, K., and Abe, T., "SPRADIAN, Structured Package for Radiation Analysis: Theory and Application," ISAS Report 1-47, 1997.
- [80] Newton, "Optiks, Inflections and Colours of Light (1704)," reprinted by Dover Publication, New York, 1982.
- [81] Wollaston, W. H., "A Method of Examining Refractive and Dispersive Powers, by Prismatic Reflection," *Philosophical Transactions of the Royal Society of London* Vol. 92, 1802, pp. 365-380.
- [82] Fraunhofer, J., *Ann. Phys.* 56, 264, 1817.
- [83] Herschel, J. F. W., *Trans. Roy. Soc. Edinburgh*, 9, 445, 1823.
- [84] Kirchhoff, G., *Monatsber. Ber. Akad. Wiss.* 783, 1859.
- [85] Kirchhoff, G., and Bunsen, R., *Ann. Chim. Phys.* 62, 452, 1961
- [86] Walsh, A., *Spectrochim. Acta* 7, 108, 1955.
- [87] Schawlow A. L., and Townes C. H., "Infrared and Optical Masers," *Physical Review*, Vol. 112, 1958, pp. 1940.
- [88] Maiman T. H., *Nature*, Vol. 187, 1960, pp. 493.
- [89] Alferov, Z. I., 1970
- [90] Pirani, F., Bartolomei M., Aquilanti V., Scotoni M., Vescovi M., Ascenzi D., Bassi D., and Cappelletti D., "Collisional orientation of the benzene molecular plane in supersonic seeded expansions, probed by infrared polarized laser absorption spectroscopy and by molecular beam scattering," *Journal of Chemical Physics*, Vol. 119, 2003, pp. 265.
- [91] Paul J. B., Scherer J. J., Collier C. P., and Saykally R. J., "Cavity ringdown laser absorption spectroscopy and time-of-flight mass spectroscopy of jet cooled platinum silicides," *Journal of Chemical Physics*, Vol. 104, 1996, pp. 2782.
- [92] Stoffelles, W. W., Stofellels, E., and Tachibana K., *Review of Scientific Instruments*, Vol. 69, 1998, pp. 3635.
- [93] Teii, K., Hori, M., Goto, T., and Ishii, N., *Journal of Applied Physics*, Vol. 87, No. 10, 2000, pp. 7185.
- [94] Measures, R. M., "Laser Remote Sensing," *John Wiley and Sons*, New York, 1984.
- [95] Menzies, R. T., and Chahine, M. T., "Remote Atmospheric Sensing with an Aierborne Laser Absorption Spectrometer," *Applied Optics*, Vol. 13, No. 12, 1974, pp. 2840.
- [96] Paci, P., Zvinevich, Y., Tanimura, S., Wyslouzil, B. E., Zahniser, M., Shorter, J., Nelson, D., and McManus B., "Spatially resolved gas phase composition measurements in supersonic flows

- using tunable diode laser absorption spectroscopy," *Journal of Chemical Physics*, Vol. 121, 2004, pp. 9964.
- [97] Davidson, D. F., Chang, A. Y., Rosa, M. D., and Hanson, R. K., "Continuous Wave Laser Absorption Techniques for Gasdynamic Measurements in Supersonic Flows," *Applied Optics* Vol. 30, 1991, pp. 2598-2608.
- [98] Baer D. S., and Hanson, R. K., "Tunable Diode Laser Absorption Diagnostics for Atmospheric Pressure Plasmas," *Journal of Quantive Spectroscopy and Radiative Transfer* Vol. 47, 1992, pp. 455-475.
- [99] Chang, H. A., Baer, D. S., and Hanson, R. K., "Semiconductor Laser Diagnostics of Atomic Oxygen for Hypersonic Flow Field Measurements," AIAA Paper 93-0628, 1993. Baer, D. S., Chang, H. A., and Hanson, R. K., "Semiconductor Laser Absorption Diagnostics of Atomic Oxygen for Atmospheric-Pressure Plasmas," AIAA Paper 93-0822, 1993.
- [100] Li, H., Hanson, R. K. and Jeffries, J. B., "Diode Laser-Induced Infrared Fluorescence of Water Vapor," *Measurement Science and Technology*, Vol. 15, No. 7, 2004, pp. 1285-1290.
- [101] Zhang, F., Fujiwara, T., and Komurasaki, K., "Absorption Sensor System for Arcjet Multi-Parameter Measurements," *Measurement Science and Technology*, Vol. 11, 2000, pp. 95-99.
- [102] Kim., S., "Development of Tunable Diode Laser Absorption Sensors for A Large-Scale Arc-Heated-Plasma Wind Tunnel," Doctor thesis, Stanford University, 2004.
- [103] Linday, A. C., Nicol, J. L. and Stancey, D. N., "linear Absorption Measurements of Pressure Broadening in Neon," *Journal of Physics B: Atomic, Molecular and Optical Physics*, Vol. 24, 1991, pp. 4901-4908.
- [104] Kasai, S., Mizutani, R., Kondo, R., Hasuo, M. and Fujimoto, T., "Dynamics of Metastable Argon Atoms in a Thin Discharge Cell: Single Beam Absorption Spectroscopy and Monte Carlo Study of the Velocity Distribution," *Journal of Physical Society of Japan*, Vol. 72, No. 8, 2003, pp. 1936-1942.
- [105] Herzberg, G., "Atomic spectra and atomic structure, Dover Publications," New York, 1944.
- [106] Matsui, M., Takayanagi, H., Oda, Y., Komurasaki, K., Arakawa, Y., "Performance of arcjet-type atomic-oxygen generator by laser absorption spectroscopy and CFD analysis," *Vacuum*, Vol.73, 3-4, 2004, pp.341-346.
- [107] Matsui, M., Takayanagi, H., Oda, Y., Komurasaki, K., Arakawa, Y., "Performance of arcjet-type atomic-oxygen generator by laser absorption spectroscopy and CFD analysis," *Vacuum*, Vol.73, 3-4, 2004, pp.341-346.
- [108] Matsui, M., Komurasaki, K., Arakawa, Y., "Characterization of Arcjet Type Arc-Heater Plumes," "AIAA 02-2242, 2002.
- [109] M. Matsui, "Laser Absorption Spectroscopy in Arc-heater Plumes," Master thesis, The

University of Tokyo, 2002.

- [110] Zel'dovich, Y. B., Raizer, Y. P., Hayes, W. D. and Probstein, R. F., "Physics of shock waves and high-temperature hydrodynamic phenomena," Academic Press New York, 1966.
- [111] NIST Atomic Spectra Database, http://physics.nist.gov/cgi-bin/AtData/main_asd
- [112] McDonald, D., and Corbett, B., "Performance characteristics of quasi-single longitudinal mode Fabry Perot lasers," *IEEE Photonics Technology Letters*, Vol. 8. 1996, pp.1127-1129.
- [113] Sale, T. E., "Vertical Cavity Surface Emission Lasers," Somerset England, Research Study Press LTD, 1975.
- [114] <http://www.ulmphotronics.com/>
- [115] <http://www.koheras.com/>
- [116] Liu, K. and Littman, M. G., "Novel geometry for single-mode scanning of tunable lasers," *Optics Letters*, Vol. 6, No. 3., 1981, pp.117-118.
- [117] Deutch, M., "Abel inversion with a simple analytic representation for experimental data," *Applied Physics Letters*, Vol 42, 1983, pp 237-239.
- [118] <http://www.wolfram.com/index.ja.html>
- [119] Davis, C., "Lasers and Electro-Optics," Cambridge University Press, 1996.
- [120] Yariv, A., "Quantum Electronics," *John Wiley and Sons*, 1989.
- [121] Bear, D. S., and Hanson, R. K., "Semiconductor laser-based measurements of quench rates in an atmospheric pressure plasma using saturated-fluorescence spectroscopy," *Applied Optics*, Vol. 32, No. 6, 1993, pp. 948-955.
- [122] <http://www.jutem.co.jp/>
- [123] Koreto, H., Master thesis, The University of Tokyo, 2002.
- [124] Matsuzaki, R., "Quasi-One-Dimensional Aerodynamics with Chemical Vibrational and Translational Nonequilibrium," *Transaction of Japan Society for Aeronautical and Space Science*, Vol. 30, No. 90, 1987, pp. 243-258.
- [125] Gupta, J. M., Yos, R. N., Thompson, R. A. and Kam-pui, L., "A Review of Reaction Rates and Thermodynamic and Transport Properties for an 11-Species Air Model for Chemical and Thermal Nonequilibrium Calculations to 30000K," NASA RP 1232, 1990.
- [126] Wilcox, D. C.; DCW Industries, California, 1993.
- [127] Shima E, et.al.; NAL SP 34, 1997, p7-12.
- [128] Jameson, A., and Yoon, S., "Lower-Upper Implicit Schemes with Multiple Grids for the Euler Equations," *AIAA Journal*, Vol. 25, No. 7, 1987.
- [129] Herdrich, G, Auweter-Kurtz, M., and Kurtz, H., "New Inductively Heated Plasma Source for Reentry Simulations," *Journal of Thermophysics and Heat Transfer*, Vol. 14, No. 2, 2000, pp. 244-249.
- [130] Herdrich, G, Auweter-Kurtz M., Endlich, P. and Kurtz, H., "Mars Entry Simulation Using

an Inductively Heated Plasma Generator,” *Journal of Spacecraft and Rocket*, Vol. 40, No. 5, 2003, pp. 690-693.

- [131] Herdrich, G., Auweter-Kurtz, M. and Kurtz, H., “A new inductively heated plasma source for re-entry simulations,” AIAA Paper 98-3022, 1998.
- [132] Herdrich, G., Auweter-Kurtz, M., Kurtz, H., Laux, T. and Schreiber, E., “Investigation of the inductively heated plasmagenerator IPG3 using injection rings of different geometries,” AIAA Paper 2000-2445, 2000.
- [133] Auweter-Kurtz, M., Herdrich, G., Laux, T. and Komurasaki, K., “Probe measurements and laser absorption spectroscopy on the IRS IPG3 plasma plume,” AIAA Paper 2001-2732, 2001.
- [134] Herdrich, G. and Auweter-Kurtz, M., “Characterization of inductively heated plasma generators using measured data in combination with a simple analytical model,” AIAA Paper 2001-3012, 2001.
- [135] Herdrich, G., Auweter-Kurtz, M. and Endlich, P., “Mars entry simulation using the inductively heated plasma generator IPG4,” AIAA Paper 2001-3013, 2001.
- [136] Herdrich, G., Auweter-Kurtz, M., Laux, P., Deportes, A., Endlich, P. and Ootegem, B. V., “Experiments at the Inductively Heated Plasma Wind Tunnels of CORIA and IRS,” AIAA Paper 2002-2711, 2002.
- [137] Endlich, P., Auweter-Kurtz, M., Herdrich, G. and Laure, S., “Mars Entry Simulation with Dust Using an Inductively Heated Generator,” AIAA Paper 2002-3237, 2002.
- [138] Herdrich, G., Auweter-Kurtz, M., Endlich, P. and Laux, T., “Simulation of Planetary Entry Manoeuvres Using the Inductively Heated Plasma Wind Tunnel PWK3,” AIAA Paper 2003-3637, 2003.
- [139] Herdrich, G. and Auweter-Kurtz, M., “Development and Characterization of Inductively Heated Plasma Generators for Atmospheric Entry Simulations,” AIAA Paper 2004-2503, 2004.